

C.P. No. 544

LIBRARY
ROYAL AIR FORCE ESTABLISHMENT
BAMFORD.

C.P. No. 544



MINISTRY OF AVIATION

AERONAUTICAL RESEARCH COUNCIL

CURRENT PAPERS

Pressure Measurements on
Three Open Nose Air Intakes at
Transonic and Supersonic Speeds,
with an Analysis of their
Drag Characteristics

by

J. C. Gibbings

LONDON: HER MAJESTY'S STATIONERY OFFICE

1961

PRICE 9s. 6d. NET

U.D.C. No. 533.697.23 : 533.6.011.5 : 533.69.048.2

March, 1960

PRESSURE MEASUREMENTS ON THREE OPEN NOSE AIR INTAKES AT
TRANSONIC AND SUPERSONIC SPEEDS, WITH AN ANALYSIS OF
THEIR DRAG CHARACTERISTICS

by

J. C. Gibbings

SUMMARY

Tests on three open nose air intakes at zero incidence over a Mach number range of 0.80 to 1.82 are described. Two of the cowls had sharp lips and the third a rounded lip. External pressure distributions, diffuser pressure recoveries and drags were obtained for a range of mass flow ratios. At supersonic speeds measurement of the nose shock wave shape made possible the division of the external drag into wave and separation drags. Comparisons with theoretical values are made for the pressure distributions, pressure recovery, nose shock wave shape, wave drag and external drag.

Previously issued as R.A.E. Rept. Aero.2637 - A.R.C. 22,134

NOTE: Tables 1 to 3 referred to on p.5 are not reproduced in this published version, but copies may be obtained on request from the Royal Aircraft Establishment.

LIST OF CONTENTS

	<u>Page</u>
1 INTRODUCTION	4
2 DESIGN AND DETAILS OF TUNNEL MODELS	4
3 RANGE OF TEST CONDITIONS	5
4 PRESSURE DISTRIBUTIONS	5
4.1 Results for the sharp lipped cowls	5
4.2 Results for the blunt cowl	6
5 PRESSURE RECOVERY	7
6 DRAG	7
6.1 General	7
6.2 Experimental results	8
6.3 Discussion of drag results	10
7 CONCLUSIONS	12
8 ACKNOWLEDGEMENT	12
LIST OF SYMBOLS	12
LIST OF REFERENCES	14
APPENDICES 1 AND 2	17-26
ILLUSTRATIONS - Figs.1-29	-
DETACHABLE ABSTRACT CARDS	-

LIST OF APPENDICES

<u>Appendix</u>		
1	- Comparison of diffuser pressure recovery weighted on a mass flow and on an area basis	17
2	- Analysis of the nose shock wave shape and the determination of wave drag	20

LIST OF TABLES

<u>Table</u>		
1	- Measured pressure coefficients on the 7.6° cowl	27
2	- Measured pressure coefficients on the 12° cowl	37
3	- Measured pressure coefficients on the blunt lip cowl	45

LIST OF ILLUSTRATIONS

	<u>Fig.</u>
Details of cowls and test rig	1
Cowl external pressure distribution, 7.6° cowl	2
Cowl external pressure distribution, 12° cowl	3
Cowl external pressure distribution, blunt lip cowl	4
Internal pressure recovery, 7.6° cowl	5
Internal pressure recovery, 12° cowl	6
Internal pressure recovery, blunt lip cowl	7
Variation of internal pressure recovery with Mach number	8
Flow past an open nose intake	9
Variation of $C_{D_{cowl}}$ with mass flow ratio, 7.6° cowl	10
Variation of $C_{D_{cowl}}$ with mass flow ratio, 12° cowl	11
Variation of $C_{D_{cowl}}$ with mass flow ratio, blunt lip cowl	12
Variation of $C_{D_{cowl}}$ with Mach number at constant mass flow ratio	13
Variation of $C_{D_{cowl_0}}$ with Mach number for the three cowls	14
Variation of $C_{D_{pre}}$ with mass flow ratio	15
Variation of external drag of intakes with mass flow	16
Variation of external drag with mass flow, 7.6° cowl	17
Variation of external drag with mass flow, 12° cowl	18
Variation of external drag with mass flow, blunt lip cowl	19
Variation of $C_{D_{ext}}$ with Mach number at constant mass flow ratio	20
Variation of form drag with mass flow ratio	21
Assumed velocity profile in the diffuser	22
Pressure recovery factors used in Appendix 1	23
Typical wave drag integrations	24
Errors in wave angle due to schlieren distortion and uneven Mach number distribution across the tunnel	25
Schlieren photograph of the flow past the 12° cowl, $M_0 = 1.82$	26
Intersection of main and secondary shock waves	27
Extrapolation of nose shock wave shape to infinity	28
Wave drag integrations	29

1 INTRODUCTION

This report describes an investigation into the aerodynamic properties of open nose, axially symmetric air-intakes at zero incidence.

The efficiency with which this type of intake decelerates the internal flow has been the subject of much research, and so in this report less emphasis is placed on this aspect of their performance than on the external drag of the intakes. This drag can vary considerably with changes of both Mach number and mass flow into the intake. If there is no external deceleration of the intake flow the external drag is dependent upon the external cowl shape. Large drags will arise at the lower subsonic speeds only if this shape is such that boundary layer separation occurs, but at higher speeds the external drag at full mass flow can depend greatly upon the cowl shape, for this dictates the wave drag. To investigate this dependence of drag upon shape, three differently shaped cowls have been tested.

When the air flowing into the intake is decelerated externally then some of the engine thrust should be carried on the cowl. However, under these conditions separation can, and often does, occur on the cowl lip, resulting in a loss of this thrust suction force and hence, in effect, an increase in drag. In addition, the external air can be regarded as flowing past a body whose bluntness increases as this external deceleration increases, and so the wave drag might be expected to increase also.

To obtain values of the various drag components occurring at reduced internal mass flow, each of the three cowls was tested over a range of values of intake mass flow at several fixed Mach numbers. All the tests were made in the R.A.E. (Bodford) 3' x 3' tunnel, which, together with its flow properties, is described in Refs. 1 and 2.

2 DESIGN AND DETAILS OF TUNNEL MODELS

A general arrangement diagram of the tunnel model intake rig is given in Fig. 1. Also shown are sketches of the three different cowls that were tested. The one marked, and hereafter referred to, as the 7.6° lip cowl, had a sharp lip whose thickness was of the order of 0.006" and whose external lip angle was $7^\circ 35'$. The 12° lip cowl was similar to the 7.6° cowl, but had a lip angle of $12^\circ 3'$ and a nose thickness of approximately 0.004". The blunt cowl had a rounded lip with a nose radius of curvature of 0.22". All three cowls had nominally the same maximum cross sectional area and the same minimum entry area.

The 7.6° cowl was a copy of one previously tested^{3,4} at a lower Reynolds number. The blunt cowl was chosen as an example of an extremely blunt nose shape, and the 12° cowl as one likely to have a wave drag intermediate in value between the other two.

On each cowl static pressure measuring holes were provided along four generators of the external surface, the range of axial position of these holes being shown in Fig. 1. The holes were arranged in cyclic order around the cowls.

Grooves were machined in the metal cowls along each of the four generators and copper tubes inlaid. The grooves were then filled with cold setting Araldite which was afterwards turned down to the cowl shape. Holes were then drilled through the Araldite into the buried copper tubes.

On the two sharp nosed cowls the regions near the lips were too thin to permit the embedding of copper tubes, and so in these cases passages were formed in the Araldite by casting the front portion around thin wedge slivers

which were later withdrawn, the passages so left being connected to copper tubes in a thicker part of the cowl. In this way it was possible to get the first hole on each sharp nosed cowl to within about 0.1" of the lip.

A pitot-static comb was fixed at the rear of the diffuser, as illustrated in Fig.1, to enable the mass flow and pressure recovery to be calculated.

Behind the comb was an exit plug whose axial position could be adjusted by an electric actuator contained in the sting. Two sizes of plug were used.

3 RANGE OF TEST CONDITIONS

All three cowls were tested over a Mach number range of 0.8 to 1.82 at zero incidence. The internal mass flow ratio was varied at all Mach numbers, minimum values of this ratio ranging from 0.45 to 0.85 and maximum values from 0.95 to 1.16.

The majority of tests were conducted at Reynolds numbers between 1.6×10^6 and 1.8×10^6 , based on the inlet nose diameter, but some further tests covered a range from 0.38×10^6 to 2.8×10^6 .

4 PRESSURE DISTRIBUTIONS

The computed pressure coefficients for all the measured pressure distributions are tabulated in Tables 1 to 3, but only a few are reproduced in graphical form. These examples were selected to illustrate the various flow features that were observed. This selection is given in Figs.2(a) to (f) for the 7.6° cowl, in Figs.3(a) to (e) for the 12° cowl, and in Figs.4(a) to (e) for the blunt cowl. For the sharp lipped cowls the pressure coefficient C_p is plotted against the axial distance from the cowl lip, x , expressed in terms of the inlet radius r_i . In the case of the blunt cowl, C_p is plotted against s/r_i for the portion around the blunt nose, where s is the distance along the surface generator from the throat, but downstream of the nose C_p is plotted against x/r_i as for the other two cowls. Each figure gives curves for one particular Mach number and a range of mass flow ratios μ .

4.1 Results for the sharp lipped cowls

On the 7.6° cowl the flattened suction peaks provide evidence of flow separation off the sharp lip when the mass flow ratio is low. This was confirmed by schlieren observation at supersonic speeds, when a corresponding shock was seen to emanate from the rear of the separated region. At Mach numbers of 0.8 and 0.9 the dead air region is quite extensive, but it becomes much smaller at and above $M_0 = 1.0$. This reduction at supersonic speeds is presumably associated with the ability of the air to turn sharp corners more easily. It is interesting to note that on this cowl at $M = 0.9$, Fig.2(b), the lip dead air region appears, disappears and then reappears as μ decreases. Applying the corresponding scale of local Mach numbers to the pressure coefficients suggests an explanation. It seems likely that when the mass flow ratio has dropped to 0.57 the local Mach number has increased sufficiently to permit the turning of the flow over the lip by a supersonic expansion. Further reduction in μ to 0.45 has increased the angle through which the flow must turn at the lip to an extent which supersonic expansion cannot achieve, and separation has reappeared.

On the 12° cowl the flow also separates from the lip, but in this case the dead air region is still comparatively large at $M_0 = 1.0$, (Fig.3b) although it becomes smaller at higher Mach numbers.

On the 7.6° cowl at $M_0 = 0.8$ and 0.9 , a typically subsonic, fairly symmetrical velocity peak occurs at the sharp corner on the cowl surface, even though the peak velocities are supersonic in the latter case. At $M_0 = 0.9$, Fig.2(b), and $\mu = 0.45$, the results indicate that the large dead air region is followed by a boundary layer so thick that it smooths out the velocity peak at the following corner. At Mach numbers of 1.0 and above an ordinary supersonic expansion occurs at this corner, Figs.2(c) to 2(f). The effect of the sharper corner on the 12° cowl is to increase the degree of expansion around it. The form of the pressure distribution at $M_0 = 0.8$, Fig.3(a), suggests that the subsonic velocity peak is followed by a small region of separation.

Though the lip thicknesses of the 7.6° and 12° cowls were only of the order of $0.006''$ and $0.004''$ respectively, there was evidence that even under full mass flow conditions the nose shock was detached. Theoretical values of the pressure coefficient at the nose of the two cowls are given in Figs.2(e), 2(f) and 3(e). These were obtained first by assuming the nose shock was attached to the lip, and so are appropriate to $\mu = 1.0$. Values were taken from the graphs of Ref. 5. Pressure coefficients were also computed from measurements of the corresponding shock wave angle at the nose and are shown in Figs.2(e) and 3(e). These measurements are described in detail in Appendix 2. In some cases they gave values of the wave angle corresponding to a detached shock.

Comparison of the experimental pressure coefficients near to the nose with the computed nose values also confirms that the nose shock was detached. The measured pressure coefficient at the first pressure hole is seen in each of these cases to lie between the attached shock value and the measured wave angle value.

The theoretical pressure distribution for the 7.6° cowl is given in Ref. 4. These values are compared with the present experimental results in Figs.2(d), 2(e) and 2(f). Except at $M_0 = 1.14$ the agreement is seen to be poor, this presumably being due to the fact that the nose shock is slightly detached. There is also a dip in the experimental curves at a value of x/r_1 of about 0.6 which is not predicted theoretically. No error in the manufacture of the model could be detected which might have been responsible for this, nor can it be attributed to disturbances from the tunnel walls since it occurred both with the solid nozzles and with the slotted transonic test section.

4.2 Results for the blunt cowl

On the blunt cowl there is a large velocity peak on the nose at the lower Mach numbers, Figs.4(a) to 4(c), which dies away at the higher supersonic speeds, Figs.4(d) and 4(e). This peak, and the associated large adverse pressure gradient downstream of it, occurs even at full mass flow.

Fig.4(a) shows that, as with the 7.6° cowl, at the lowest value of μ there existed a separation followed by a boundary layer apparently thick enough to smooth out the velocity peak at the succeeding corner.

It can be seen, for example in Fig.4(a), that quite high velocity peaks occurred at the internal throat when running at full mass flow.

5 PRESSURE RECOVERY

There are several possible ways of expressing the efficiency of the diffusion process in an intake. Of these, the most commonly used is stagnation pressure, weighted on either a mass flow or an area basis. These two methods of weighting are compared in Appendix 1, where they are seen, in the present conditions, to give almost identical efficiencies, and efficiencies which, for the subsonic diffusion process, can be effectively 100%.

The present results are weighted on a mass flow basis, and values of \bar{H}/H_0 , the ratio of the mean stagnation pressure at the end of the diffuser to the free stream stagnation pressure, are shown in Figs. 5, 6 and 7 plotted against the mass flow ratio μ . Within the limits of experimental error (which are of the order of $\pm 2\%$), the value of \bar{H}/H_0 for each Mach number is constant over most of the mass flow range, but for values of μ near unity there is a slight fall-off in pressure recovery, which is most marked at subsonic and transonic speeds. This is presumably due to the disappearance of pre-entry diffusion, but there are insufficient experimental points in this region to assess the effect accurately. The mean pressure recoveries are plotted against free stream Mach number in Fig. 8. For comparison, curves are also included of the loss due to a normal shock. These agree excellently with the experimental results and, as predicted in Appendix 1, show that the decrease in efficiency at supersonic speeds is effectively equal to the normal shock loss, and is little dependent upon the subsonic diffusion.

6 DRAG

6.1 General

Since several terms are used in the discussion of the drag of intakes, a brief résumé is given here. Consider the flow past the open-nose intake shown in Fig. 9. AB is the pre-entry stream tube, which extends to infinity upstream of the intake and which separates the internal and external flows. In accordance with the recommendations of Ref. 6, and neglecting skin friction, the external drag of the intake, D_{ext} , is considered as the sum of two components, the pre-entry drag, D_{pre} , and the cowl intrinsic normal pressure drag, D_{cowl} . In coefficient form we have

$$C_{D_{\text{pre}}} = \frac{1}{q A_{\text{ref}}} \int_{A_0}^{A_i} (p - p_0) dA$$

$$C_{D_{\text{cowl}}} = \frac{1}{q A_{\text{ref}}} \int_{A_i}^{A_c} (p - p_0) dA$$

$$C_{D_{\text{cowl}}} + C_{D_{\text{pre}}} = C_{D_{\text{ext}}}$$

where p is the pressure along, and A the cross-sectional area of, the stream tube or stream surface forming the boundary of the external flow, p_0 is the

free stream static pressure and q is the dynamic pressure. These definitions are quite explicit with a sharp lipped cowl, but with a round nosed cowl a difficulty arises in that as the mass flow is altered, the position of the stagnation point on the lip changes so that the inlet area is not constant. If, however, we modify the definitions, putting

$$C_{D_{pre}} = \frac{1}{q A_{ref}} \int_{A_o}^{A_t} (p-p_o) dA = \frac{1}{q A_{ref}} \int_{A_o}^{A_i} (p-p_o) dA + \frac{1}{q A_{ref}} \int_{A_i}^{A_t} (p-p_o) dA$$

$$C_{D_{cowl}} = \frac{1}{q A_{ref}} \int_{A_t}^{A_c} (p-p_o) dA = \frac{1}{q A_{ref}} \int_{A_i}^{A_c} (p-p_o) dA - \frac{1}{q A_{ref}} \int_{A_i}^{A_t} (p-p_o) dA$$

where A_t is the cross-sectional area of the internal throat, then the total external drag is correct, although its components are slightly in error by equal and opposite amounts. This is the procedure that has been adopted here. The reference area has been taken as the inlet area in the case of the sharp lipped cowls and the area of the internal throat in the case of the blunt lip cowl.

When the intake is operating at unit mass flow ratio the pre-entry drag is zero: the drag coefficient in this condition will be denoted by $C_{D_{cowl_0}}$. If the mass flow ratio is then reduced so that the intake is "spilling", the external drag can be expressed in the form

$$C_{D_{ext}} = C_{D_{cowl_0}} + C_{D_{spill}}$$

where $C_{D_{spill}}$ is the "spillage drag" coefficient

6.2 Experimental results

6.2.1 Cowl normal pressure drag

The cowl normal pressure drag was obtained by graphical integration of the external pressure distributions and the results for the three cowls, for the various Mach numbers and mass flow ratios tested, are displayed in Figs. 10, 11 and 12. Most of these results are for a Reynolds number, based on the inlet diameter, of between 1.5 and 1.7 million. Some spot results obtained for Reynolds numbers of 2.5 and 2.8 million are shown for the 7.6° cowl in Fig. 10 and for the blunt lip cowl in Fig. 12. Some further results for Reynolds numbers of 0.8 and 0.4 million are shown in Fig. 10 to give a comparison with those of Refs. 3 and 4; it is seen that the present values of $C_{D_{cowl}}$ are considerably higher. This point is discussed later when the total external drag is considered, but it can be noted here that there is only a very small scale effect upon the pressure distribution for Reynolds numbers greater than 0.8 million.

Measurements were made at close Mach number intervals over the transonic range for two fixed plug positions. The corresponding results for $C_{D_{cowl}}$ are shown in Fig. 13, the mass flow ratios quoted being means over the range of Mach number. Also included are the values appropriate to $\mu = 1$, which were

obtained by cross-plotting from Figs. 10, 11 and 12. The comparable results for the 7.6° cowl from Ref. 4 are also reproduced, and again some discrepancies between the two sets of results are to be noted.

Finally, $C_{D_{cowl_0}}$, the cowl normal pressure drag coefficient when $\mu = 1$, is plotted for the three cowls against Mach number in Fig. 14. It is noticeable that the drag of the blunt lip cowl is lower than that of the 12° cowl up to a Mach number of about 1.2, despite the extreme bluntness of the lip. At the higher supersonic speeds $C_{D_{cowl_0}}$ for the blunt nosed cowl increases with free stream Mach number, but for the other two it decreases.

6.2.2 The pre-entry drag

The pre-entry drag coefficient has been defined above as

$$C_{D_{pre}} = \frac{1}{q A_i} \int_{A_0}^{A_i} (p - p_0) dA .$$

From momentum considerations, and assuming one-dimensional flow in the pre-entry stream tube, this can be expressed in the form

$$\begin{aligned} C_{D_{pre}} &= \frac{1}{q A_i} \left[(p_i - p_0) A_i + \rho_i V_i^2 A_i - \rho_0 V_0^2 A_0 \right] \\ &= \frac{2}{\gamma M_0^2} \left[\left(\frac{p_i}{p_0} - 1 \right) + \mu \gamma M_0^2 \left(\frac{V_i}{V_0} - 1 \right) \right] . \end{aligned}$$

At supersonic speeds a shock wave normally occurs ahead of the intake. If the suffix *w* denotes conditions immediately behind the shock, then a more convenient form for computation using existing tables is:

$$C_{D_{pre}} = \frac{2}{\gamma M_0^2} \left[\left(\frac{p_i}{p_w} \cdot \frac{p_w}{p_0} - 1 \right) + \mu \gamma M_0^2 \left(\frac{V_i}{a_0^*} \cdot \frac{a_0^*}{V_w} \cdot \frac{M_w}{M_0} \cdot \frac{a_w}{a_0} - 1 \right) \right] .$$

Values of $C_{D_{pre}}$ for the various test Mach numbers have been calculated and are shown plotted against mass flow ratio in Fig. 15. At the higher supersonic speeds $C_{D_{pre}}$ increases in an almost linear manner as μ decreases from unity, but with reduction of speed it becomes progressively more non-linear in the mass flow ratio range 0.6 to 1.0.

6.2.3 Total external drag

The external drag is the sum of the cowl normal pressure drag and the pre-entry drag. The external drag coefficients thus obtained are plotted against mass flow ratio in Figs. 16 to 19. The corresponding theoretical values of Refs. 11 and 12 for supersonic speeds are also included and are discussed later in section 6.3. In addition, the comparable results recorded in Ref. 3 are reproduced in Fig. 17. At a Mach number of 1.42 the present

results lie roughly in a mean position between the two previous sets of results obtained from pressure and force measurements, but at $M_0 = 1.82$ there is better agreement with the results of Ref. 3 derived from pressure measurements than with those obtained from force measurements. However, the agreement is not very good in either case.

The variation of external drag with Mach number for constant values of the mass flow ratio μ is shown in Fig.20. Fig.20(a) gives the results for the 7.6° cowl and the results (for $\mu = 1$) of the previous tests on this cowl shape for comparison⁴. There is agreement only over a portion of the Mach number range. The discrepancy could be due to inaccuracies in computing the drags from the results of Ref. 4 because of the limited number of pressure holes in the much smaller model.

Also plotted in Fig.20(a) is the theoretical curve for $\mu = 1$ from Ref.4. The theoretical values are lower than the experimental results, but show the same variation of drag with Mach number.

Comparison of Figs.20(a), (b) and (c) shows that at $\mu = 1$ the drags for the two sharp nosed cowls decrease with increasing Mach number in the supersonic part of the speed range. However, the drags for these two cowls at the lowest mass flow ratio and for the blunt lip cowl at all mass flow ratios increase with Mach number.

6.2.4 Wave drag

A matter of considerable interest is the division of the external drag at supersonic speeds into that attributable to the entropy rise through the nose shock system and that due to lip separation. In particular, a comparison in this respect is made between the sharp and blunt lip cowls.

The wave drag was computed by a method that made use of measurements of the nose wave shape obtained from schlieren photographs. This method, which is described in detail in Appendix 2, makes use of Whitham's analysis of the wave shape^{7,8}. Several sources of inaccuracy in computing the wave drag are discussed in this Appendix, leading to a suggested final maximum error in $C_{D_{wave}}$ of ± 0.05 .

Values of the wave drag thus obtained are shown in Fig.17,18 and 19 and are discussed in section 6.3.

6.2.5 Form drag

The present measurements only include drag due to normal pressure loads and neglect skin friction, so the external drag is the sum of the form drag and wave drag. The form drag coefficient is thus given by

$$C_{D_{form}} = C_{D_{ext}} - C_{D_{wave}} \cdot$$

Values of the form drag coefficient for Mach numbers of 1.42 and 1.82 are plotted against mass flow ratio in Figs.21(a) and (b) and are discussed in detail below.

6.3 Discussion of drag results

Form drag is to be expected at supersonic speeds when there is a lip separation on the sharp nosed cowls at reduced mass flow, but is not to be expected on either the blunt nose cowl or on the sharp nosed cowls when $\mu = 1$ and there is no nose separation. This is confirmed by the results

shown in Fig.21, within the previously quoted accuracy for the values of $C_{D_{wave}}$, that is ± 0.05 . On the sharp lip cowls a form drag appears as the mass flow ratio decreases from unity, but on the blunt nose cowl the form drag is zero for all values of μ .

The existence of form drag on sharp lipped cowls for mass flow ratios less than unity was indicated also by results obtained by Brajnikoff and Rogers⁹ and by Clark and Lewis¹⁰ which showed wave drag values much lower than the total drag when $\mu < 1$.

The analyses of Graham¹¹ and of Moeckel^{12,13} can be used to give estimates of the wave drag. Such estimates are compared with the present experimental values in Figs.16,17,18 and 19. Graham's theory gives only the spillage wave drag and does not predict the drag at full mass flow, so in comparing his theoretical values with experiment the theoretical curves have been vertically displaced so as to pass through the experimental value at $\mu = 1$. Moeckel's theory gives an estimate for both the drag at full mass flow for a blunt nosed cowl and its variation with mass flow for all cowl shapes.

On the round nose cowl where experiment has shown there to be little or no form drag a direct comparison can be made with the external drag and the theories of Graham and Moeckel. This is done in Figs.16(c) and 19. At all Mach numbers Graham's theory underestimates the drag rise, the discrepancy being greatest at transonic speeds. Moeckel's theory does not predict the drag at full mass flow very reliably, but gives better agreement than Graham's theory for the slope $\partial C_{D_{ext}}/\partial \mu$. This is best illustrated where the Moeckel curves have been vertically displaced so as to pass through the experimental values at $\mu = 1$ (Fig.19).

In the case of the sharp lipped cowls, as soon as the mass flow ratio falls below unity the flow separates off the lip and a separation bubble is formed. This separation bubble, although initially small in extent, gives rise to an appreciable form drag but so modifies the effective external cowl shape that the wave drag is actually reduced for small amounts of spillage. As a consequence, it would not be expected that the spillage drag would be in agreement with a theory which considered only the wave drag. However, on the 7.6° lip cowl good agreement is obtained between experiment and Graham's theory for mass flow ratios above 0.7 at Mach numbers of 1.42, 1.61 and 1.82, and on the 12° lip cowl at Mach numbers of 1.14 and 1.82, although at $M = 1.42$ and 1.61 the agreement is not so good, the experimental spillage drag tending to be less than the theoretical value. It would thus appear that with a sharp lipped intake the fact that the flow separates from the lip is not necessarily detrimental from the spillage drag point of view at supersonic speeds for moderate amounts of spillage, because the flow separation may reduce the wave drag so that the sum of the actual form and wave drags is no greater than the wave drag that would occur in the absence of any separation.

Summarising the drag characteristics of the three cowls, at $M = 0.8$ the 7.6° lip cowl has less than one third of the drag of the other two cowls at full mass flow, a lower drag than the 12° cowl down to $\mu = 0.51$ and a lower drag than the blunt lip cowl over the whole range of mass flow ratios covered by the tests, that is down to 0.45. Under full mass flow conditions all three cowls exhibit a steep drag rise at transonic speeds. In the case of the sharp lipped cowls, the drag reaches a maximum at a Mach number of about 1.15 and thereafter decreases, but with the round nose cowl the drag continues to increase at supersonic speeds. By a Mach number of 1.82 the drags at full mass flow of the 7.6° , the 12° and the blunt lip cowl are respectively in the ratio 1.0: 2.6: 5.5. The marked superiority of the 7.6° cowl is now maintained at reduced mass flow, however, because at this speed the spillage drags are not greatly dissimilar for the three cowl shapes.

7 CONCLUSIONS

Tests on three cowls with different lip shapes at zero incidence have shown a wide variation of external drag with both Mach number and mass flow into the intake. At full mass flow the cowl with a 7.6° sharp lip had a very much lower drag throughout the speed range than either the 12° sharp lip cowl or the cowl with a rounded lip. At transonic speeds the spillage drag of all the cowls varied in a non-linear manner with spillage, and the spillage drag of the 12° lip cowl was considerably less than that of the other two cowls for mass flow ratios less than about 0.8. At supersonic speeds the spillage drag did not follow a completely consistent pattern, but at the highest Mach number tested it was still slightly less on the 12° cowl.

The shape of the nose shock wave at supersonic speeds was found to be in reasonable agreement with that predicted by Whitham^{7,8}, and an improved method of determining the wave drag from measurements of the wave shape is described. The round lip cowl was found to have zero form drag at supersonic speeds, the external drag being purely wave drag for all mass flow ratios investigated. Comparison of the spillage drag of this cowl with the theoretical values of Graham¹¹ and of Moeckel^{12,13} showed better agreement with the latter theory for Mach numbers above 1.4, Graham's theory tending to underestimate slightly the rate of drag rise with spillage. In the case of the sharp lip cowls, as soon as the mass flow ratio fell below unity the flow separated off the lip and gave rise to a large form drag. However, the separation so modified the effective cowl shape that the wave drag was reduced for small amounts of spillage and it is suggested that the sum of the actual form and wave drags may be no greater than the wave drag that would occur in the absence of any separation.

The internal pressure recovery was virtually identical for the three cowls, being effectively 100% at subsonic speeds and reduced only by an amount equal to the normal shock loss at supersonic speeds. It is also shown that for normal amounts of subsonic diffusion, weighting the pressure recovery on a mass flow or on an area basis leads to essentially the same result.

8 ACKNOWLEDGEMENT

Acknowledgement is made of the assistance of Dr. I. McGregor in the final preparation of this report.

LIST OF SYMBOLS

(Some symbols used only once are not included here)

a_1, a_2	coefficients defined in equation 12, Appendix 2
A	cross-sectional area
A_0	area of pre-entry stream tube at infinity upstream
C_D	drag coefficient = $D/q_0 A_i$
C_p	pressure coefficient = $(p - p_0)/q_0$

LIST OF SYMBOLS (Contd)

D	drag
D_{cowl}	drag due to normal pressures acting on the external surface of the cowl
D_{cowl_0}	value of D_{cowl} when $\mu = 1$
H	stagnation pressure
H_p	stagnation pressure in central potential core at end of diffuser
\bar{H}	mean stagnation pressure at end of diffuser
\bar{H}_A	value of \bar{H} weighted on an area basis
\bar{H}_m	value of \bar{H} weighted on a mass flow basis
K_1, K_2	coefficients of diffuser performance defined in Appendix 1
M	Mach number
M_p	Mach number of central potential core at end of diffuser
M_s	$M_0 \sin \sigma$
m	mass flow
p	pressure
(p_{s_0}/p_{s_2})	stagnation pressure ratio across a shock wave
P	function defined by equation 6, Appendix 2
q	dynamic pressure
r	radial co-ordinate at end of diffuser (Appendix 1), radial co-ordinate to shock wave (Appendix 2)
r_p	radius of central potential core at end of diffuser, arbitrarily chosen radius at limit of schlieren picture
r_i	radius of inlet to intake
s	distance along surface generator of blunt cowl
u	local velocity at end of diffuser
u_p	velocity of central potential core at end of diffuser
V	velocity
x	axial distance along cowls
dx/dr	slope of nose shock wave

LIST OF SYMBOLS (Contd)

α	$\cot \mu_0$
μ	mass flow ratio
μ_0	Mach angle of free stream
ν	function defined in equation 7, Appendix 2
ρ	density
σ	wave angle

Suffixes

o	conditions in free stream
i	at inlet
ext	external
pre	pre-entry

LIST OF REFERENCES

<u>No.</u>	<u>Author(s)</u>	<u>Title, etc</u>
1	Morris, D.E.	Calibration of the flow in the working section of the 3' x 3' tunnel, National Aeronautical Establishment. A.R.C. C.P.261. Sept. 1954.
2	Sutton, E.P.	The development of slotted working section liners for transonic operation of the N.A.E. 3 ft wind tunnel. A.R.C. R. & M. 3085. March 1955.
3	Fraenkel, L.E.	The external drag of some pitot-type intakes at supersonic speeds, Part II. A.R.C. 14,289. June 1951.
4	Griggs, C.F., Goldsmith, E.L.	Measurements of spillage drag on a pitot-type intake at supersonic speeds. A.R.C. 16,687. Aug. 1953.
5	Rosenhead, L. (Chairman)	A selection of graphs for use in calculations of compressible airflow. Oxford, 1954.

LIST OF REFERENCES (Contd)

<u>No.</u>	<u>Author(s)</u>	<u>Title, etc</u>
6	Mair, W.A. (Chairman)	Report of the definitions panel on definitions to be used in the description and analysis of drag. A.R.C. C.P. 369, May, 1957.
7	Whitham, G.B.	The behaviour of supersonic flow past a body of revolution far from the axis. Proc. Roy. Soc. A, Vol 201, p.89, 1950.
8	Whitham, G.B.	The flow pattern of a supersonic projectile. Comm. Pure and Applied Maths., Vol. 5, pp 301-348, 1952.
9	Brajnikoff, G.B., Rogers, A.W.	Characteristics of four nose inlets as measured at Mach numbers between 1.4 and 2.0. N.A.C.A. T.N. 3724, August 1956.
10	Clark, D.B., Lewis, R.B.	Development of wide range supersonic inlets. N.A.C.A./T.I.L. P31487.
11	Graham, E.W.	Notes on the drag of scoops and blunt bodies. Douglas Aircraft Corp. Report SM - 13747. April 1950.
12	Moeckel, W.E.	Approximate method for predicting the form and location of detached shock waves ahead of plane or axially symmetric bodies. N.A.C.A. T.N. 1921, July 1949.
13	Moeckel, W.E.	Estimation of inlet lip forces at subsonic and supersonic speeds. N.A.C.A. T.N. 3457, June 1955.
14	Fraenkel, L.E., Goldsmith, E.L.	A preliminary investigation of the performance of conical supersonic diffusers. A.R.C. 12,582. June 1949.
15	Wyatt, De M.D.	Analysis of errors introduced by several methods of weighting non-uniform duct flows. N.A.C.A. T.N. 3400.
16	Ohman, L.	An experimental method of determining the drag of a shock wave, with application to a ducted body. Sweden, F.F.A. Rept. 51, 1954.
17	Ferri, A.	Method for evaluating from shadow or schlieren photographs the pressure drag in two-dimensional or axially symmetrical flow phenomena with detached shock. N.A.C.A. T.N. 1808.
18	Munk, M.M., Crown, J.C.	The head shock wave. Proc. 7th Int. Congress Appl. Maths.
19	Liepmann, H.W.	On the relation between wave drag and entropy increase. Douglas Aircraft Co. Rept. SM 13726.

LIST OF REFERENCES (Contd)

<u>No.</u>	<u>Author(s)</u>	<u>Title, etc</u>
20.	Nucci, L.M.	The external shock drag of supersonic inlets having subsonic entrance flow. N.A.C.A./T.I.B. 2586, December, 1950.
21	Liepmann, H.W., Puckett, A.E.	Introduction to the aerodynamics of a compressible fluid. Wiley, New York, 1947, p.58.
22	Ibid	p.41
23	Ogwcki, H.	On the attached curved shock in front of an open nosed axially symmetrical body. Journal Phys. Soc. Japan, Vol 9, Part 5, Sept.-Oct. 1954.
24	Thomas, T.Y.	Calculation of the curvature of attached shock waves. Journal Maths Phys., Vol 27, pp. 279 - 297, 1948.

1

2

3

4

5

6

APPENDIX 1

A COMPARISON OF DIFFUSER PRESSURE RECOVERY WEIGHTED ON A MASS FLOW AND ON AN AREA BASIS

Of the several forms in which diffuser performance has been correlated the most commonly used is that in which the stagnation pressure distribution at exit is weighted on either an area or a mass flow basis. A brief comparison of these methods of weighting has been given by Fraenkel and Goldsmith¹⁴ and by Wyatt¹⁵. A more general comparison is given here covering cases where the exit flow is axi-symmetric and has a central potential core.

The assumed velocity profile at the exit from the diffuser is sketched in Fig.22, where for the outer viscous annulus we write

$$\frac{u}{u_p} = \left(\frac{R_d - r}{R_d - r_p} \right)^{1/n} \quad (1)$$

The mean stagnation pressure \bar{H} , weighted on an area basis, is given by

$$\frac{\bar{H}_A}{H_o} = \frac{\int \frac{H}{H_o} dA}{A}$$

For the low Mach numbers obtaining at the end of the diffuser, incompressible flow may be assumed, so that

$$H = p + \frac{1}{2} \rho u^2 \quad (2)$$

and then

$$\begin{aligned} \int H dA &= \int_c^{R_d} 2\pi r (p + \frac{1}{2} \rho u^2) dr \\ &= pA + \rho u_p^2 A \int_0^{1.0} \left(\frac{u}{u_p} \right)^2 \left(\frac{r}{R_d} \right) \cdot d\left(\frac{r}{R_d} \right) \end{aligned}$$

and substituting from equation (1) gives

$$\begin{aligned} \int H dA &= pA + \rho u_p^2 \left[\frac{1}{2} \left(\frac{r_p}{R_d} \right)^2 + \frac{n}{n+1} \left(1 - \frac{r_p}{R_d} \right) \left\{ \frac{r_p}{R_d} + \frac{n}{n+2} \right\} \right] A \\ &= pA + \frac{1}{2} \rho u_p^2 A (K_1 + 1) \quad (3) \end{aligned}$$

the term in square brackets being written $(K_1 + 1)$. Hence

$$\frac{\bar{H}_A}{H_p} = \frac{p + \frac{1}{2} \rho u_p^2 (K_1 + 1)}{p + \frac{1}{2} \rho u_p^2}$$

so that

$$\left(\frac{\bar{H}_A}{H_p} - 1 \right) \left(1 + \frac{2}{\gamma M_p^2} \right) = K_1 \quad (4)$$

Similarly, the mean stagnation pressure weighted on a mass flow basis is given by

$$\frac{\bar{H}_m}{H_o} = \frac{\int \frac{H}{H_o} \cdot dm}{m} \quad (5)$$

where m is the mass flow

$$m = \int \rho u \, dA \quad (6)$$

and substituting from equation (1) gives

$$\begin{aligned} \frac{m}{\rho u_p A} &= \left(\frac{r_p}{R_d} \right)^2 + 2 \int_{r_p/R_d}^1 \left(\frac{1 - r/R_d}{1 - r_p/R_d} \right)^{1/n} \frac{r}{R_d} \cdot d \left(\frac{r}{R_d} \right) \\ &= \left(\frac{r_p}{R_d} \right)^2 + \frac{2n}{2n+1} \left(\frac{r_p}{R_d} + \frac{n}{n+1} \right) \left(1 - \frac{r_p}{R_d} \right) = c_1 \text{ (say)} \quad (7) \end{aligned}$$

Also

$$\begin{aligned} \int H \, dm &= \int_0^{R_d} \rho u \, 2\pi r \left(p + \frac{1}{2} \rho u^2 \right) dr \\ &= p \cdot m + \frac{1}{2} \rho^2 u_p^3 A \left[\left(\frac{r_p}{R_d} \right)^2 + \frac{2n}{2n+3} \left(\frac{r_p}{R_d} + \frac{n}{n+3} \right) \left(1 - \frac{r_p}{R_d} \right) \right] \\ &= p \cdot m + \frac{1}{2} \rho^2 u_p^3 A \cdot c_2 \quad (8) \end{aligned}$$

where c_2 denotes the bracketed term. Hence

$$\frac{\bar{H}_m}{H_p} = \frac{p + \frac{1}{2} \rho u_p^2 \cdot \frac{c_2}{c_1}}{p + \frac{1}{2} \rho u_p^2}$$

and

$$\left(\frac{\bar{H}_m}{H_p} - 1 \right) \left(1 + \frac{2}{\gamma M_p^2} \right) = \frac{c_2}{c_1} - 1$$

$$= K_2 \quad (\text{say}) . \quad (9)$$

Values of K_1 and K_2 are plotted in Fig.23 for a value of $n = 7$. It is apparent that there is little difference between the values of \bar{H}_m/H_p and \bar{H}_A/H_p and, for the low values of M_p normally encountered, that \bar{H}/H_p is very near to unity. Thus up to the stage where H_p is equal to the stagnation pressure at entry to the intake, the pressure recovery on these bases is almost unity during subsonic flight and is effectively decreased from unity only by the nose shock loss at supersonic speeds. The results of the present experiments were consistent with these findings.

APPENDIX 2

ANALYSIS OF THE NOSE SHOCK WAVE SHAPE AND THE DETERMINATION OF WAVE DRAG

1 INTRODUCTION

Several attempts to obtain the wave drag from measurements of the nose shock wave shape have been made previously, but the one most closely followed here is that due to Ohman¹⁶. This would appear to require less computation than the method suggested by Ferri¹⁷.

Ohman found considerable scatter in the estimated wave drag values which appear to arise mainly from inaccuracies in the method of extrapolating the measured shock wave shape to infinity. Brajnikoff and Rogers⁹, in applying a similar method due to Munk and Crown¹⁸, tried approximating the outer wave shape by an hyperbola, but without great success. This lack of success may be connected with the objection raised by Liepmann¹⁹ to the use of an hyperbola as an approximation to the wave shape.

Brajnikoff and Rogers attempted to avoid the difficulty arising from the use of a momentum circuit infinite in extent by also trying Nucci's method²⁰, but checks that they made of the accuracy again indicated rather large errors.

With the method now given for extending the necessary integration to infinity it is believed that errors from this source are reduced and results of an improved accuracy are obtained. Estimates of the likely error are discussed later.

2 THEORY OF THE METHOD

(a) General

In the notation of Fig.9, the wave drag is given by (Ref.19)

$$C_{D_{\text{wave}}} = \frac{4}{r_i^2} \int_{r_0}^{\infty} \left(1 - \frac{V_3}{V_0}\right) r \, dr \quad (1)$$

Using Ohman's notation,

$$\frac{V_3}{V_0} = (1 - \nu)^{\frac{1}{2}}$$

where

$$\nu = \frac{2P}{(\gamma-1) M_0^2}$$

and

$$P = \left(\frac{p_{s0}}{p_{s2}}\right)^{(\gamma-1)/\gamma} - 1 \quad (2)$$

where p_{s0}/p_{s2} is the stagnation pressure ratio across the nose shock wave.

(b) Visible part of the wave

The stagnation pressure ratio across a shock wave is given by (Ref.21)

$$\left(\frac{p_{s0}}{p_{s2}}\right)^{(\gamma-1)/\gamma} = \frac{2}{\gamma+1} \left(\frac{2\gamma}{\gamma+1}\right)^{1/\gamma} \left(\frac{\gamma-1}{2} + \frac{1}{M_s^2}\right) \left(M_s^2 - \frac{\gamma-1}{2\gamma}\right)^{1/\gamma} \quad (3)$$

where $M_s = M_0 \sin \sigma$ (4)

σ being the wave angle.

Values of σ for the part of the wave included in the schlieren picture were obtained from a photographically enlarged drawing. The slopes were derived by differentiating numerically using a three point formula and so the ratio V_3/V_0 could be computed. The integrand of equation (1) was then plotted and the integration from r_0 to the edge of the schlieren picture at $r = r_p$ (say) carried out graphically.

(c) Extension of the shock wave shape to infinity

An expression for the shape of an axi-symmetrical shock wave far from a body has been given by Whitham^{7,8} as

$$x = \alpha r - br^{3/4} - h(0) - \frac{1}{2} b h'(0) r^{-1/4} + O(r^{-1/2} \log r) \quad (5)$$

where x is the axial co-ordinate

r is the radial co-ordinate

$$\alpha = \cot \mu_0$$

$\mu_0 =$ Mach angle of the undisturbed flow.

Differentiating, we have

$$\frac{dx}{dr} = \alpha - \frac{3}{4} b r^{-1/4} + \frac{1}{8} b h'(0) r^{-5/4} + \dots$$

which for convenience is written as

$$\frac{dx}{dr} = \alpha + a_1 r^{-3/4} + a_2 r^{-5/4} + \dots \quad (6)$$

Now
$$\sin^2 \sigma = \frac{1}{1 + \left(\frac{dx}{dr}\right)^2} \quad (7)$$

and
$$M_c^2 = 1 + \alpha^2$$

so that
$$M_s^2 = \frac{1 + \alpha^2}{1 + \left(\frac{dx}{dr}\right)^2} \quad (8)$$

Substituting for (dx/dr) and expanding by the Binomial theorem then leads to

$$M_s^2 = 1 - \frac{1}{1+\alpha^2} \left[2 a_1 \alpha r^{-3/4} + 2 a_2 \alpha r^{-5/4} + \dots \right]$$

so that

$$M_s^2 - 1 = - \frac{2\alpha}{M_o^2} \left[a_1 r^{-3/4} + a_2 r^{-5/4} + \dots \right] \quad (9)$$

Combining equations (2) and (3) and expanding into series form gives

$$P = - \frac{2}{3} \cdot \frac{1-\gamma}{(1+\gamma)^2} (M_s^2 - 1)^3 + 2\gamma \cdot \frac{1-\gamma}{(1+\gamma)^3} (M_s^2 - 1)^4 + \dots$$

so that

$$\nu = \frac{4}{M_o^2} \cdot \frac{1}{(1+\gamma)^3} \left[\frac{1}{3} (\gamma+1) (M_s^2 - 1)^3 - \gamma (M_s^2 - 1)^4 + \dots \right]$$

Hence

$$\begin{aligned} 1 - (1-\nu)^{\frac{1}{2}} &\approx \frac{2}{M_o^2 (1+\gamma)^3} \left[\frac{1}{3} (\gamma+1) (M_s^2 - 1)^3 \right] \\ &\approx \frac{2}{3 M_o^2 (1+\gamma)^2} \left[- \frac{2\alpha}{M_o^2} \cdot r^{-3/4} (a_1 + a_2 r^{-1/2}) \right]^3 \end{aligned}$$

and so

$$\left[1 - (1-\nu)^{1/2}\right] r \simeq - \frac{16 \alpha^3}{3 M_o^8 (1+\gamma)^2} \cdot r^{-5/4} \left[a_1 + a_2 r^{-1/2} \right]^3.$$

For the typical values of M_s at $r = r_p$ that were encountered, this expression gave errors for the integrand at $r = r_p$ of up to about 10%, resulting in errors in the integration to infinity of not more than about 4% or 5%.

Integrating, and making use of equation (6) gives

$$\int_{r_p}^{\infty} \left(1 - \frac{\nu}{V}\right) r \, dr \simeq$$

$$\frac{64 \alpha^3}{3 M_o^8 (1+\gamma)^2} \cdot r_p^{-1/4} \left[\left(a_1^2 + \frac{1}{7} a_2^2 \cdot r_p^{-1} \right) \left\{ r^{3/4} \left(a - \frac{dx}{dr} \right) \right\}_{r=r_p} - \frac{16}{35} a_1 a_2^2 r_p^{-1} \right]$$

.... (10)

thus enabling the integration to infinity to be completed.

3 INTEGRATION TO r_p

Two examples of plots of the integrand of equation (1) are given in Figs. 24(a) and (b), the former for the 12° lip cowl and the latter for the blunt lip cowl. The values of r_o were computed from the mass flow ratio and the value of r_p was arbitrarily chosen as 16 on the scale shown. Points obtained from measurements of both the upper and lower waves on the schlieren picture are included.

A minor point of interest shown by these graphs is that although a normal shock wave would result in a straight line through the origin, this linearity is not maintained up to the point $r = r_o$, so that the outer portion of the stream tube that enters the intake has passed through an oblique shock. Thus the entering air has a slight variation of stagnation pressure across it, increasing outwards from the centre.

4 SOURCES OF ERROR

Apart from errors arising in measurement of wave angle, there are three further possible sources of error in obtaining the curves of Fig. 24, and these were all investigated.

The first arises from optical distortion in the tunnel schlieren system. This was found by photographing the shadow of a taut wire placed vertically across the tunnel window and just outside it. The slope of the wire was then measured in the same way as described for the measurement of shock wave slopes. The resulting distortion from a straight line is shown

plotted in Fig.25. The maximum distortion at the edge of the picture is of the order of one half to one degree. As can be seen from the scatter, it is only slightly greater than the accuracy with which the slopes can be measured.

The second source of error is that the Mach number distribution along the upstream side of the wave front is not necessarily uniform as assumed for the computations. To obtain an idea of the amount of this variation, a schlieren picture of the flow past a comb of static tubes was used. Measurements were made as before of the angles of the nose shock waves off each tube and their variation is also plotted in Fig.25 for both upper and lower waves. The trend of the variation is similar to that of the schlieren distortion and so within the experimental error there is no significant variation of Mach number across the tunnel.

The wave drag was computed as being that attributable to the entropy change through the main nose shock and ignored any other shocks. In some cases with the sharp nosed cowls a secondary shock emanated from the rear of the nose separation bubble. Neglect of this formed the third possible source of error.

To estimate the order of the strength of these secondary shock waves, use was made of a schlieren picture in which the nose shock and the secondary shock were seen to merge into one. A print of this picture is given in Fig.26. Measurements of the slopes of these two waves are plotted in Fig.27, with, for comparison, the Mach angle corresponding to the upstream Mach number. The intersection of the waves appears to occur at about $r = 8.0''$. Though very accurate readings cannot be taken from this graph, if for the inner main wave at the point of intersection a value of $dx/dr = 1.27$ is accepted, then the corresponding stream deflection through the wave is 5.0° and the Mach number between this wave and the secondary wave is 1.64. Then if a value of $dx/dr = 1.27$ is accepted at this point for the secondary wave, its stream deflection is 0.6° . Thus the deflection through the outer wave is $5.0^\circ + 0.6^\circ = 5.6^\circ$, leading to a value of $dx/dr = 1.26$, which fits the experimental data.

Small values of the entropy rise, ΔS , through a shock wave are proportional to $(M_s^2 - 1)^3$ (Ref.22), which, using the above figures, gives values of ΔS through the outer shock, the inner main shock and the inner secondary shock that are in the proportions

$$1.0 : 0.84 : 0.002$$

so that the entropy change through the secondary shock may be neglected.

5 INTEGRATION TO INFINITY

If only the first three terms of equation (6) are significant, then a plot of $\left(\alpha - \frac{dx}{dr}\right) \cdot r^{3/4}$ against $r^{-1/2}$ would yield a straight line. Two examples of such plots are shown in Fig.28. The scatter of the experimental points is considerable towards the origin, where values correspond to the outer portion of the shock wave and where $\left(\alpha - \frac{dx}{dr}\right)$ is becoming small. This experimental scatter is probably the main cause of inaccuracy in the final value of $C_{D_{wave}}$.

Despite the scatter there is a reasonable confirmation of the linear variation, and hence of the validity of Whitham's theory for the wave shape.

Fitting of the straight line enabled values of a_1 and a_2 to be obtained, and use of equation (10) then gave the integral to infinity.

The overall error in the wave drag obtained was mainly due to the error in fitting straight lines, of $\left(\alpha - \frac{dx}{dr}\right) r^{3/4}$ against $r^{-1/2}$, to the experimental points. Experience in doing this suggests a final error of about ± 0.05 in the wave drag coefficient.

6 ATTACHED SHOCK CASES

Previous evidence from the cowl pressure distributions was quoted to show that at full mass flow the apparently "attached" shock was in fact detached to a noticeable degree. Further evidence for this was obtained during the wave drag calculations. In Fig. 29 two examples of the experimental values of the integrand of equation (1) are plotted: both are for the sharp nosed cowls at nominally full mass flow. The theoretical values of $\left(1 - \frac{V_3}{V_0}\right) r$ at the nose assuming an attached shock are also shown for comparison. They are seen to be much lower than the corresponding experimental values, indicating that the shock wave at the nose is much steeper than in the "attached" shock case.

Two curves have been drawn through these theoretical points. The first was obtained by assuming that the shock wave shape is given by the first three terms of equation (5). In both cases this curve is seen to lie well below the experimental values.

The second curve was obtained by computing the curvature K_w of the nose shock at the lip. Now

$$\begin{aligned} K_w &= \frac{d^2x}{dr^2} / \left[1 + \left(\frac{dx}{dr} \right)^2 \right]^{3/2} \\ &= \frac{d^2x}{dr^2} \left(\frac{M_s}{M_0} \right)^3 \end{aligned}$$

from equations (4) and (7).

Expanding dx/dr as a Taylor series, we have,

$$\begin{aligned} \frac{dx}{dr} &= \left(\frac{dx}{dr} \right)_{r=r_0} + (r - r_0) \left(\frac{d^2x}{dr^2} \right)_{r=r_0} + \dots \\ &= \left(\frac{dx}{dr} \right)_{r=r_0} + (r - r_0) K_w \left(\frac{M_0}{M_s} \right)^3 + \dots \end{aligned}$$

Values of K_w were computed using an expression given by Ogwoki²³ for the ratio of the curvature of an axi-symmetric shock to that of a two-dimensional

shock, values for the curvature of the latter being obtained from existing tables (Ref.27). Substitution in the above series was then used to compute values of $\left(1 - \frac{v^3}{v_0^3}\right) r$ for small values of $(r - r_0)$. The curves obtained are

shown in Fig.29 and are seen to give much lower values than the previous ones, but apparently better agreement with the slope of the experimental curves at $r = r_0$. This may not necessarily be of great significance, because this slope depends upon the value of d^2x/dr^2 as well as dx/dr . In fact,

$$\frac{d}{dr} \left[\left(1 - \frac{v^3}{v_0^3}\right) r \right] = (1 - \sqrt{1-v}) - \frac{v}{\sqrt{1-v}} \cdot \frac{r}{2P} \cdot \frac{dP}{dM_s} \cdot \frac{M_s^3}{M_0^3} \cdot \frac{dx}{dr} \cdot \frac{d^2x}{dr^2} .$$



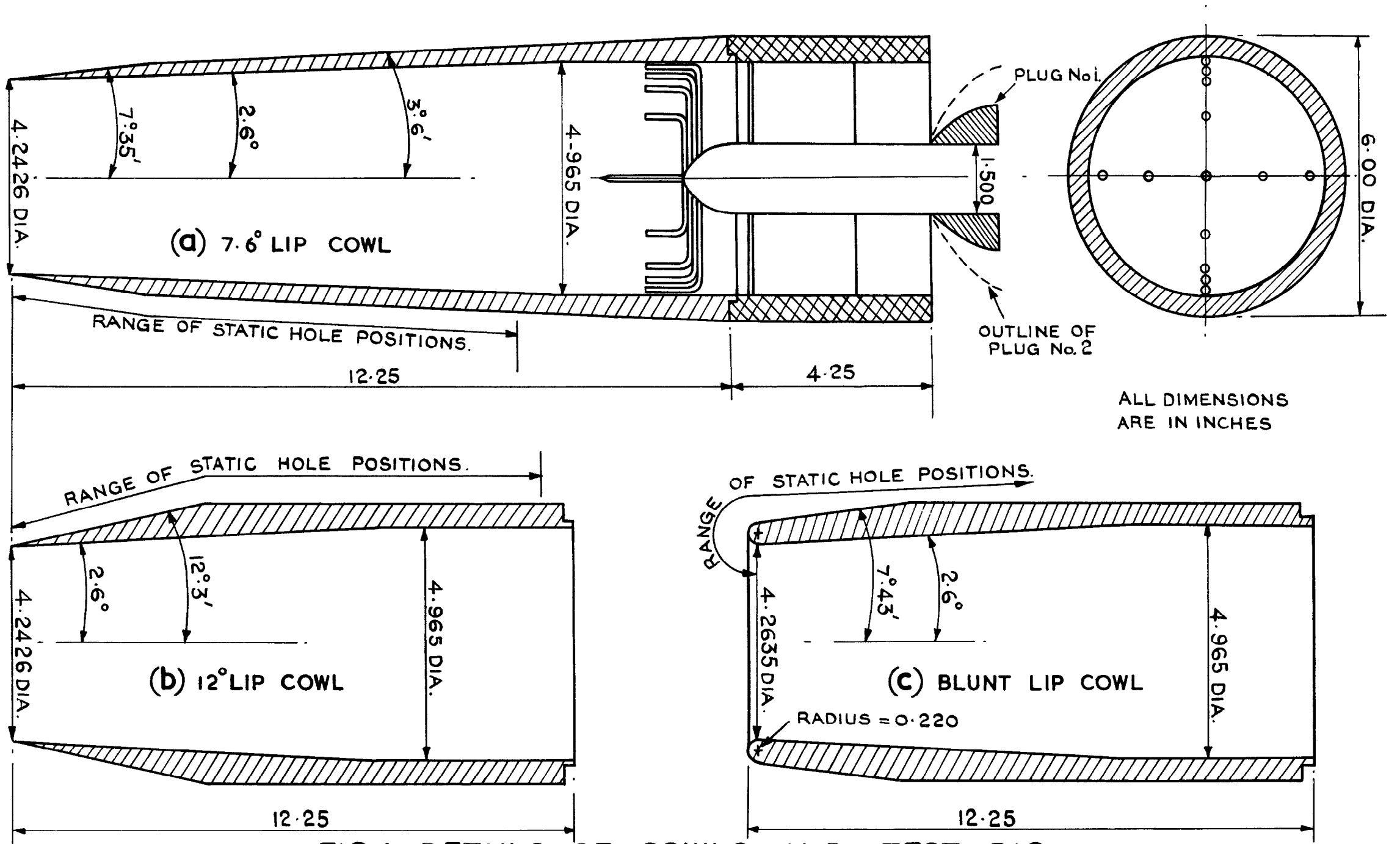


FIG. I. DETAILS OF COWLS AND TEST RIG.

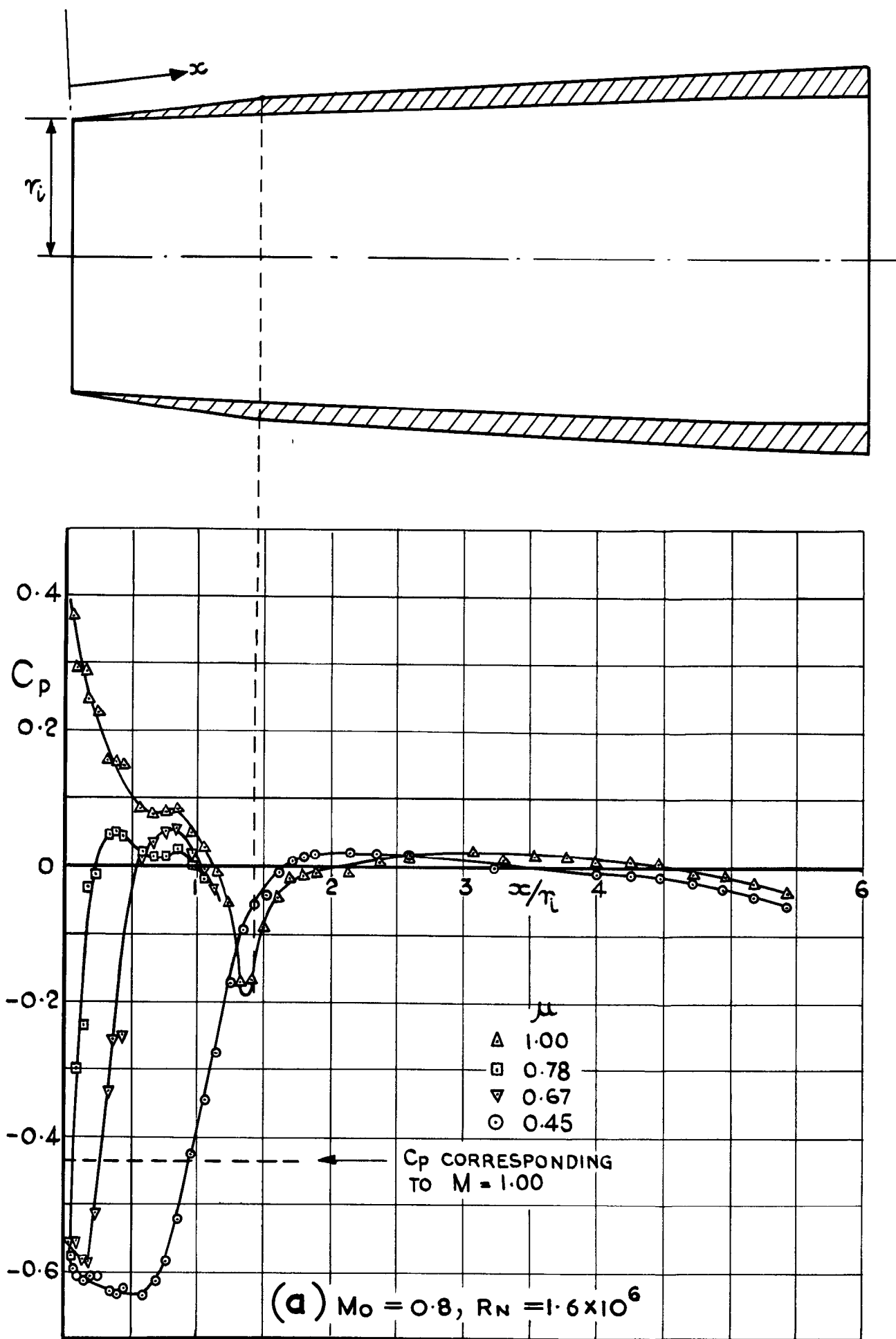
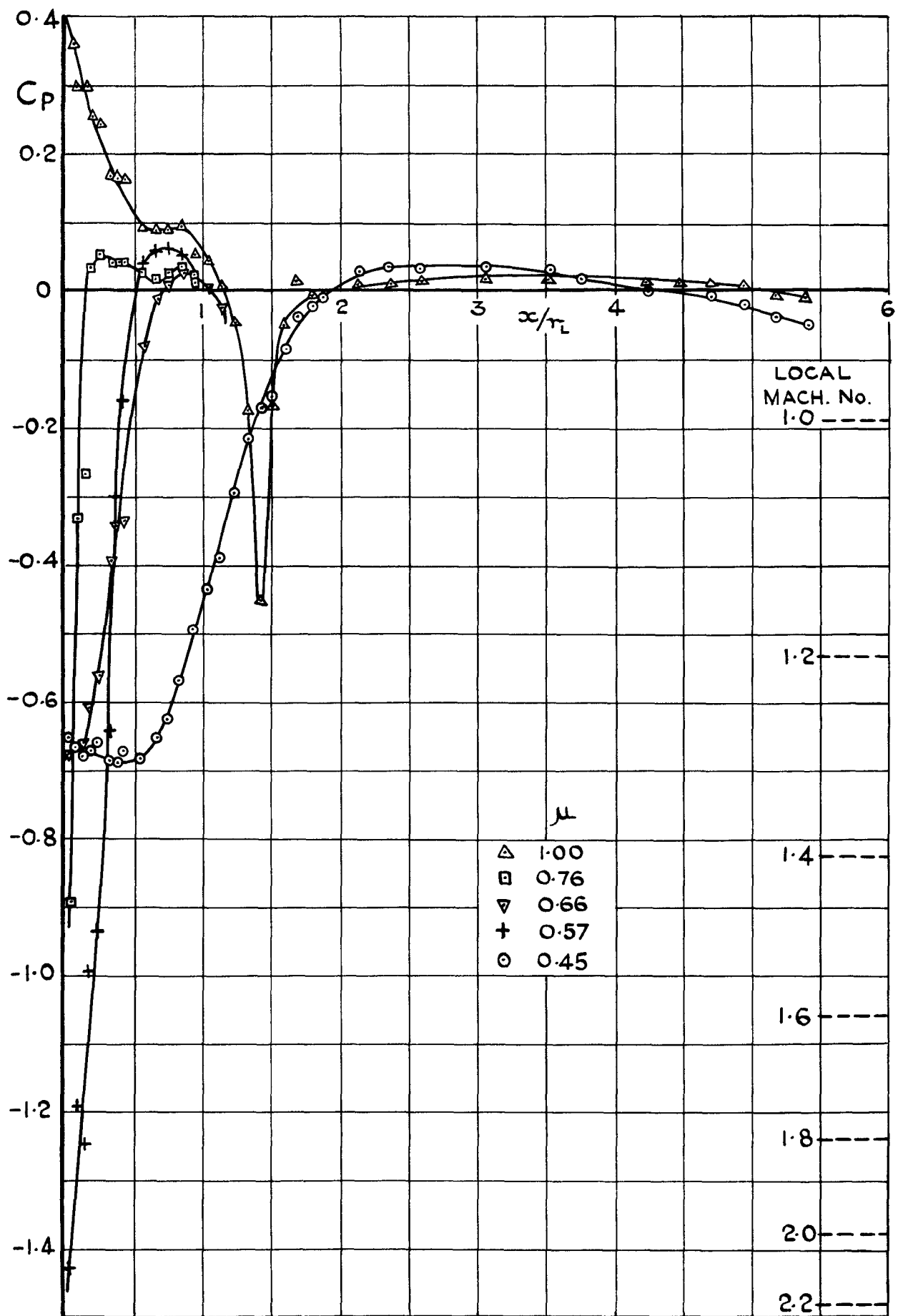
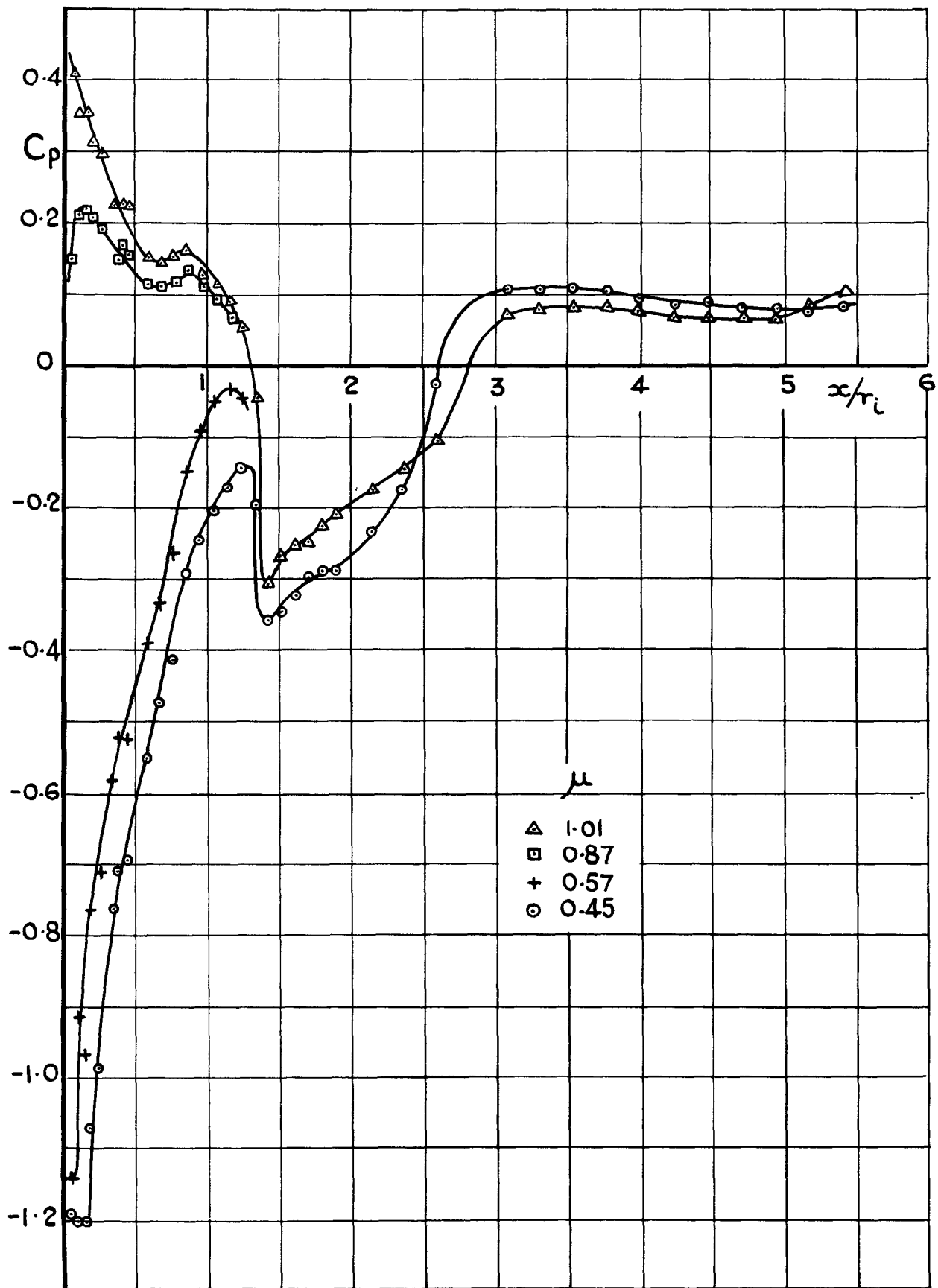


FIG. 2. COWL EXTERNAL PRESSURE DISTRIBUTION, 7.6° LIP COWL.

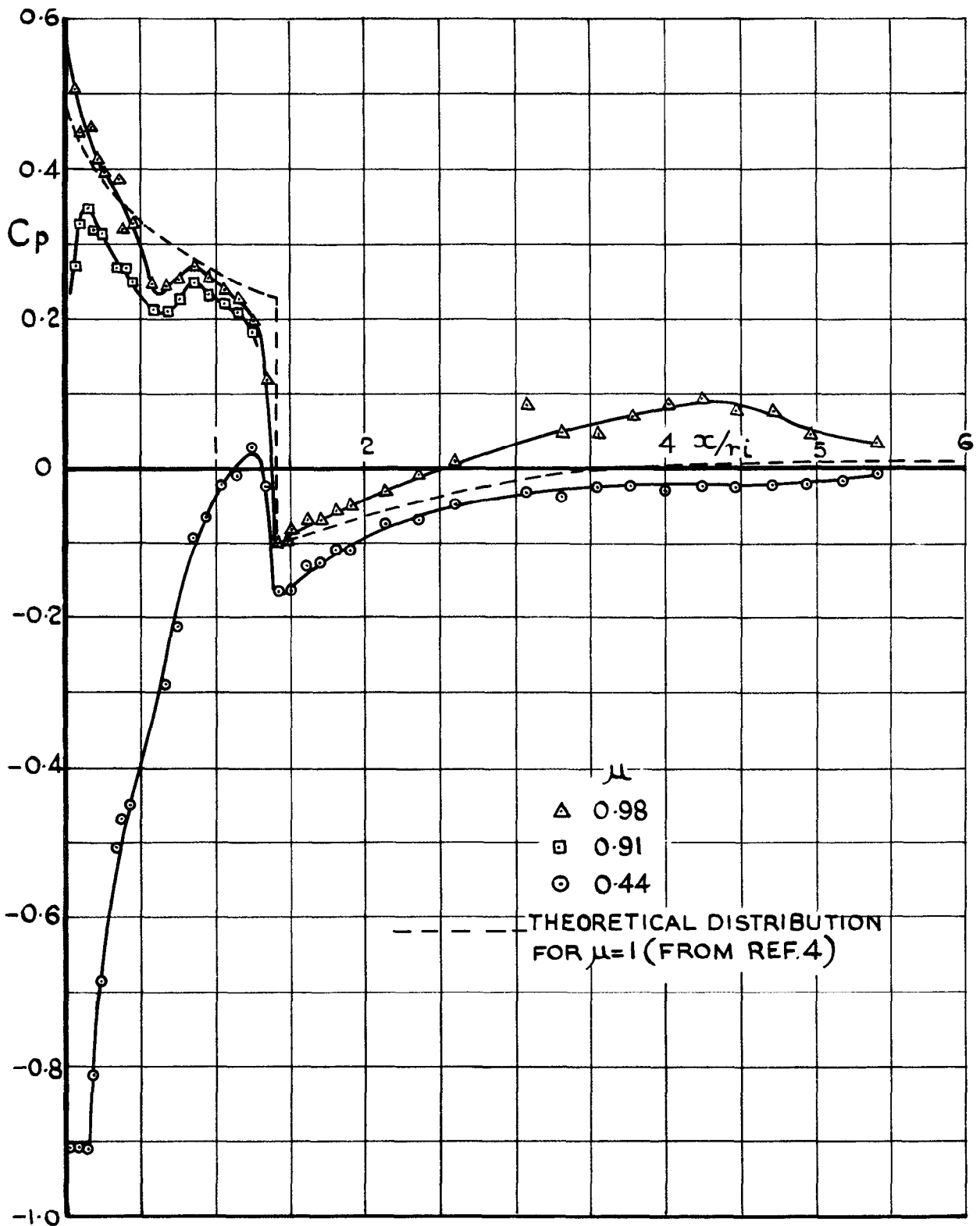


(b) $M_0 = 0.90$, $R_N = 1.7 \times 10^6$
FIG. 2. (CONT.) - COWL EXTERNAL PRESSURE DISTRIBUTION, 7.6° LIP COWL.



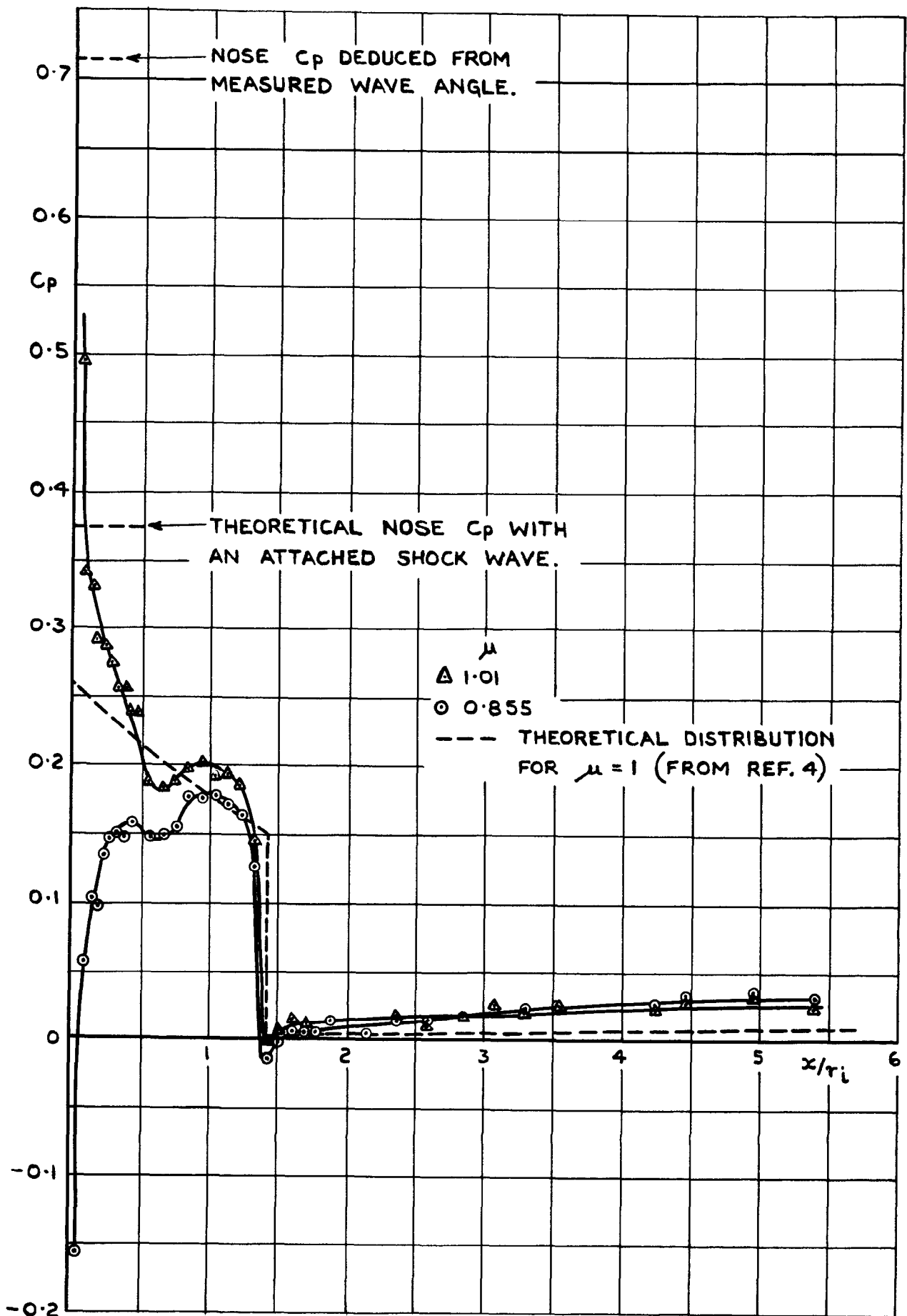
(C) $M_0 = 1.00$, $R_N = 1.75 \times 10^6$

FIG. 2. (CONT.) COWL EXTERNAL PRESSURE DISTRIBUTION, 7.6° LIP COWL.



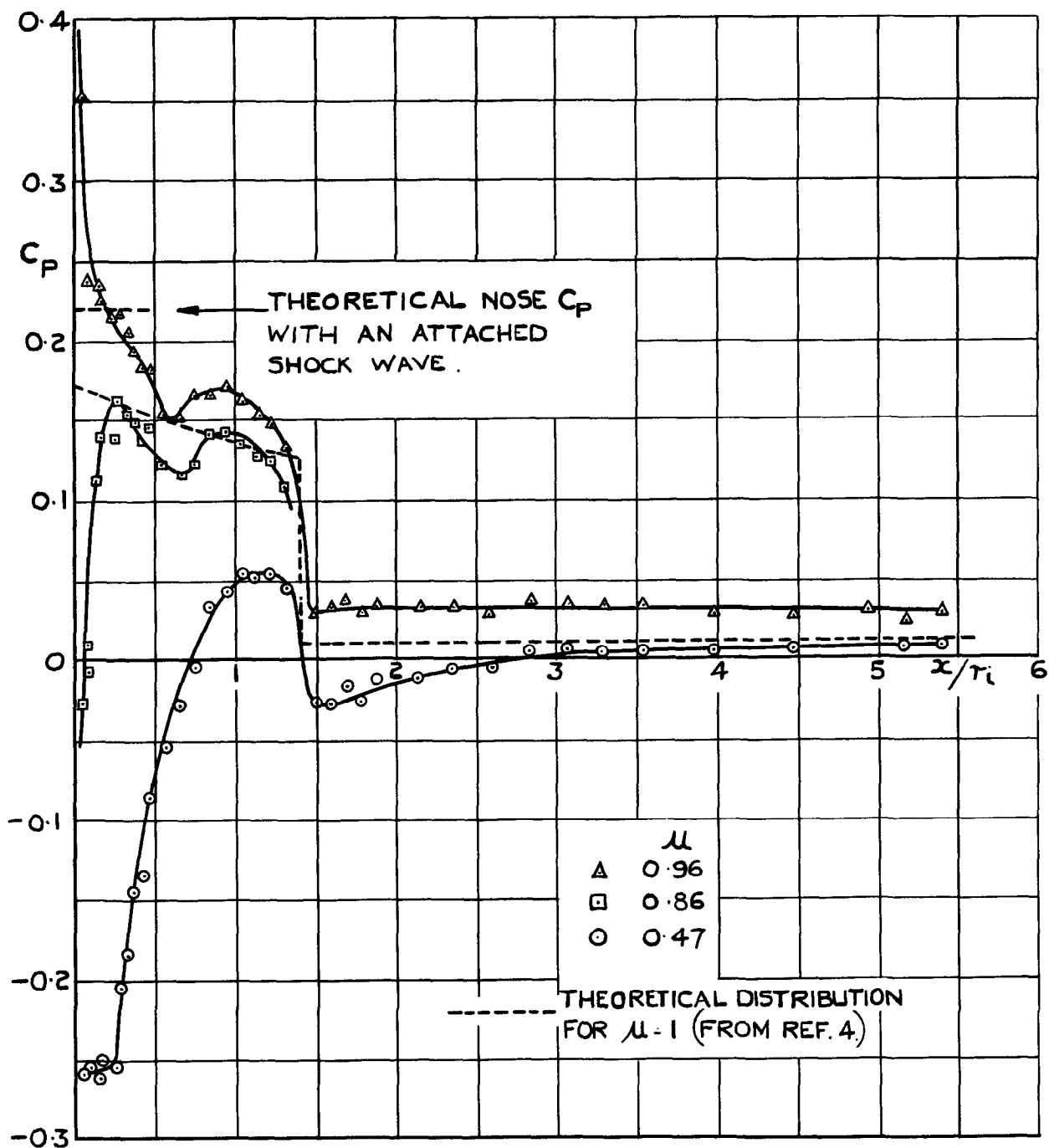
(d) $M_o=1.14$, $R_N=1.8 \times 10^6$

FIG.2.(CONT.) COWL EXTERNAL PRESSURE DISTRIBUTION, 7.6° LIP COWL.



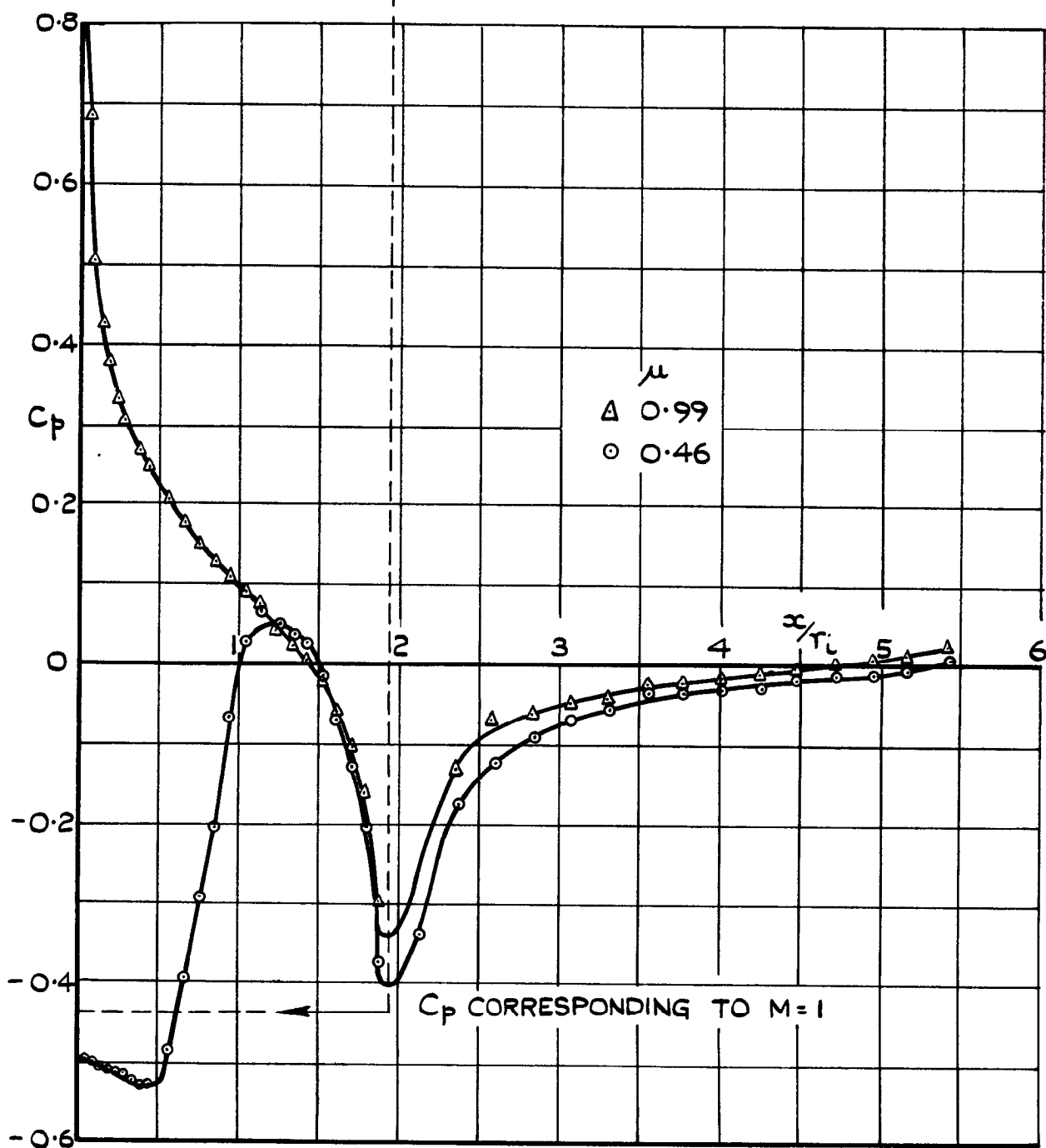
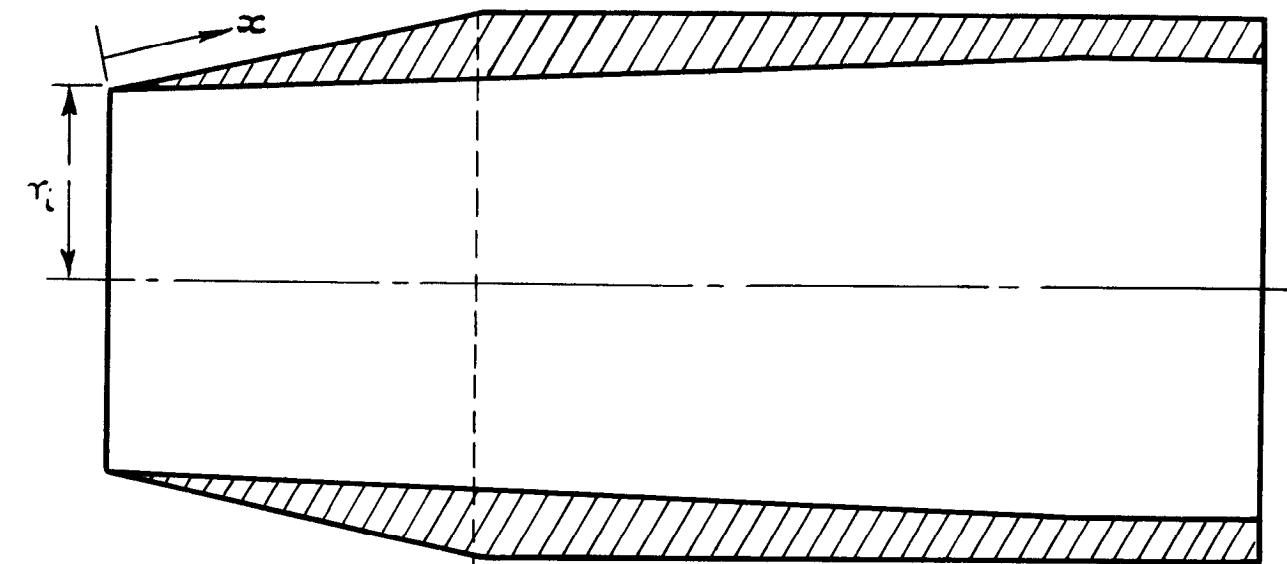
(e) $M_0 = 1.42$, $R_N = 1.6 \times 10^6$

FIG. 2 (CONT.) COWL EXTERNAL PRESSURE DISTRIBUTION, 7.6° LIP COWL.



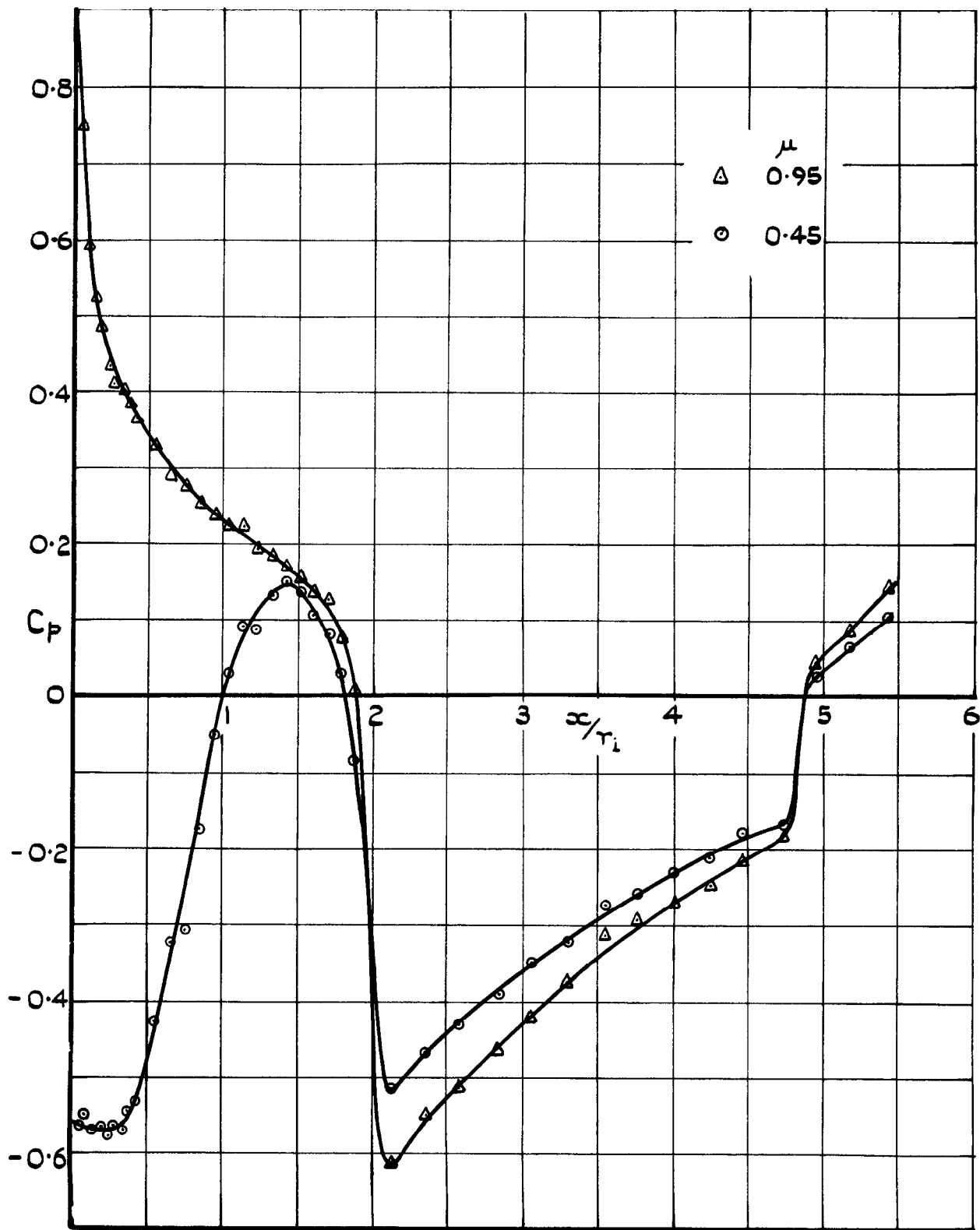
(f) $M_0 = 1.82$, $R_N = 0.78 \times 10^6$

FIG. 2. COWL EXTERNAL PRESSURE DISTRIBUTION, 7.6° LIP COWL.



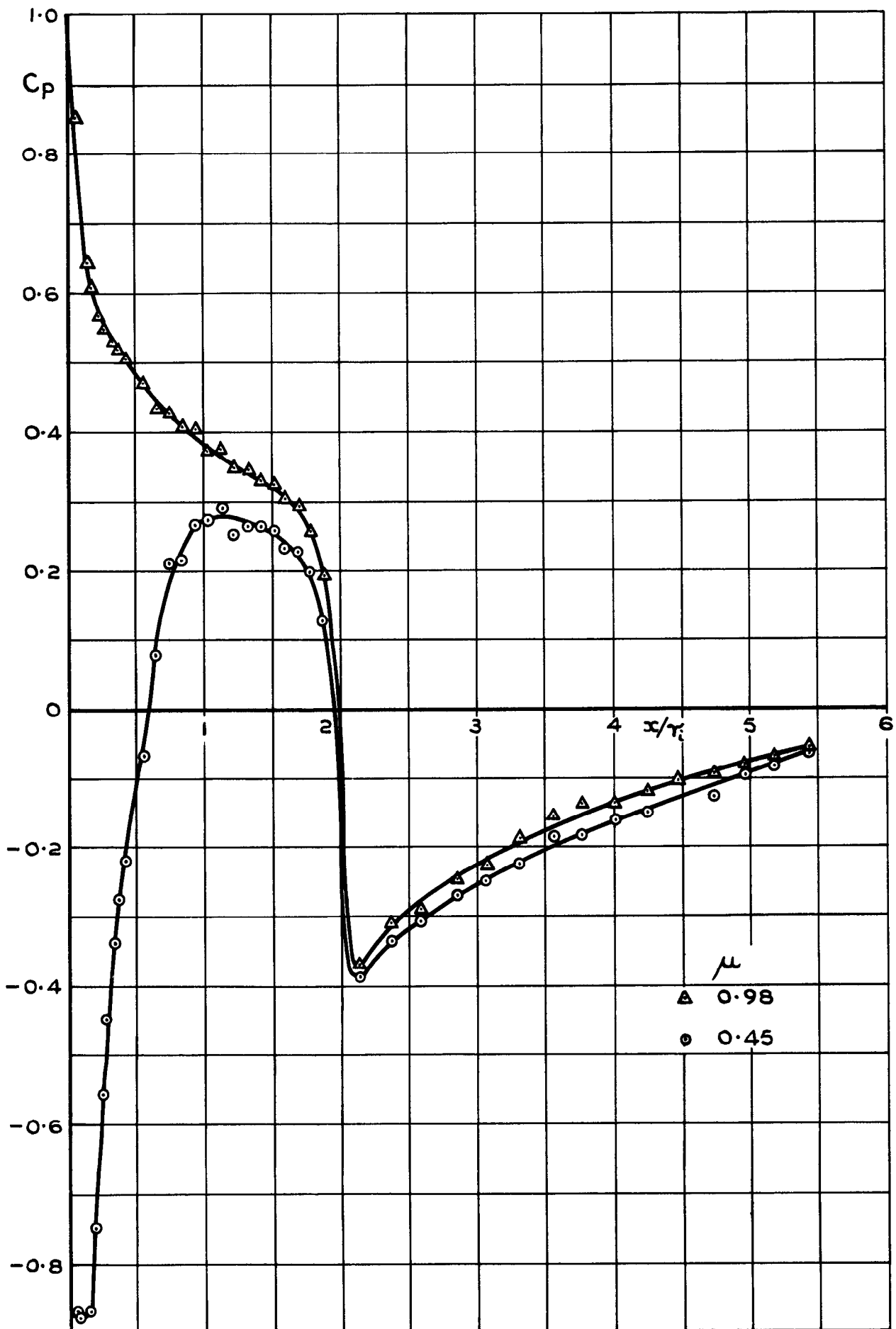
(a) $M_0 = 0.80, R_M = 1.6 \times 10^6$

FIG.3. COWL EXTERNAL PRESSURE DISTRIBUTION, 12° LIP COWL.



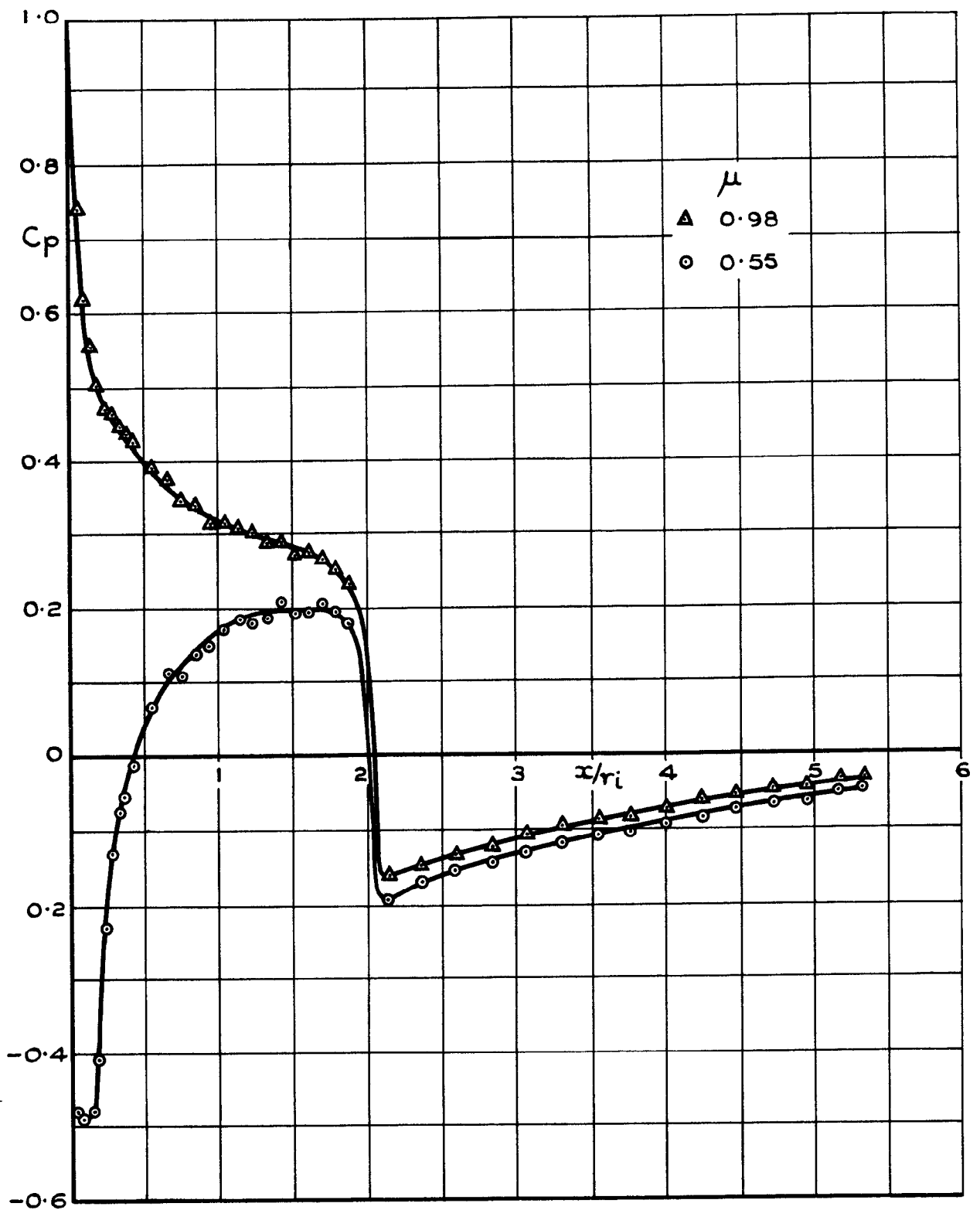
(b) $M_0 = 1.00$, $R_N = 1.75 \times 10^6$

FIG.3.(CONT.) COWL EXTERNAL PRESSURE DISTRIBUTION, 12° LIP COWL.



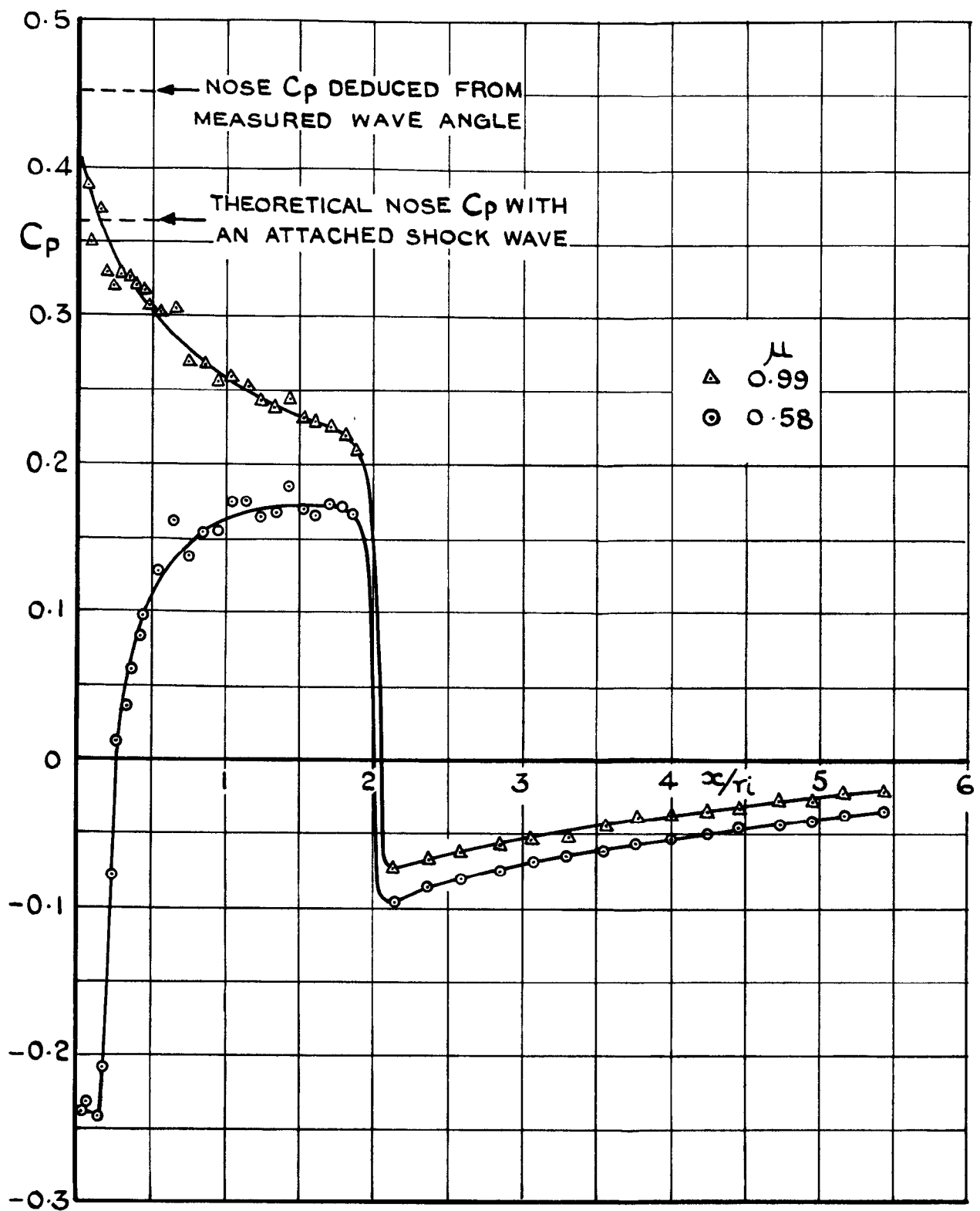
(C) $M_0 = 1.14$, $R_N = 1.8 \times 10^6$.

FIG. 3 (CONT.) - COWL EXTERNAL PRESSURE DISTRIBUTION, 12° LIP COWL.



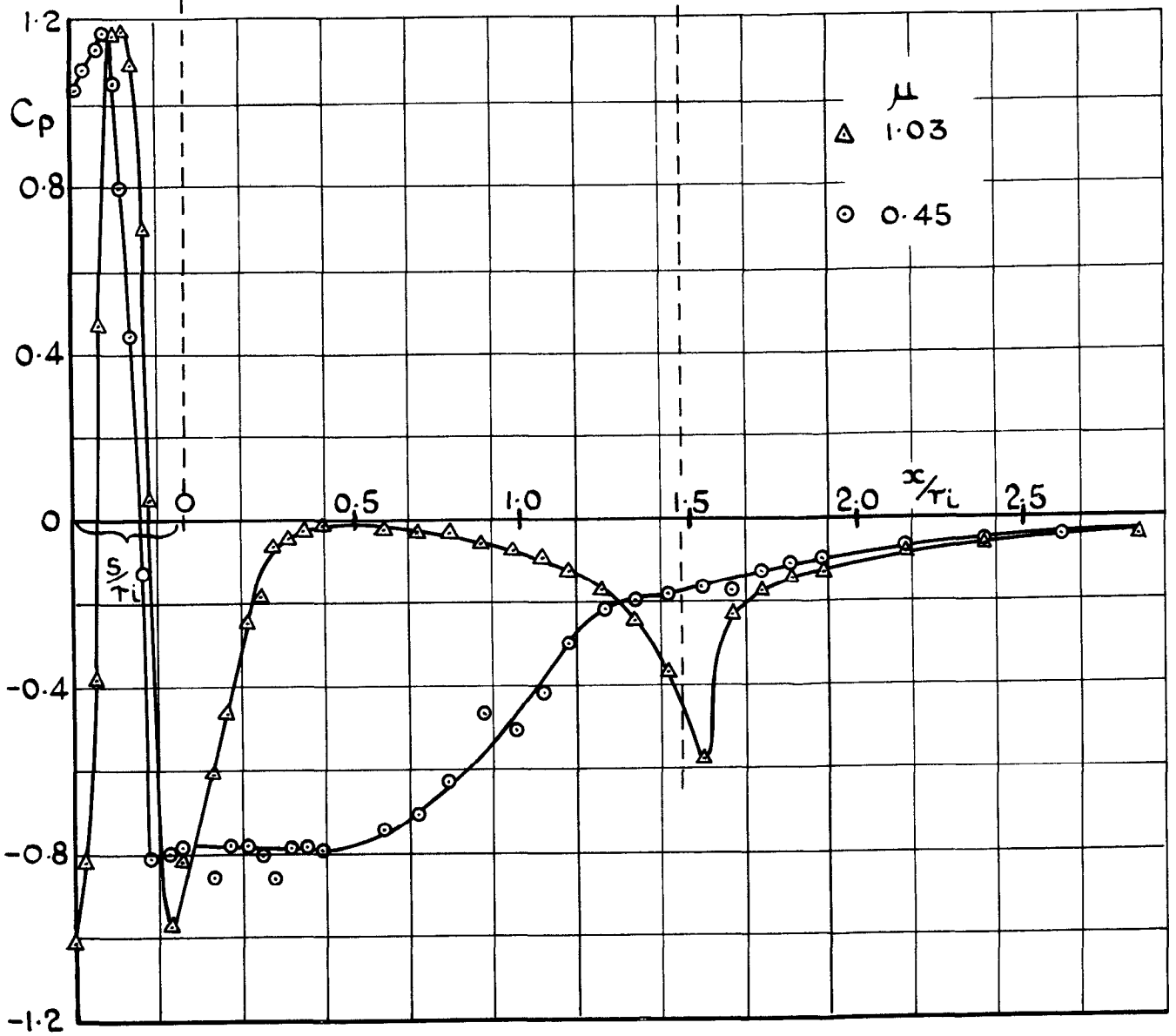
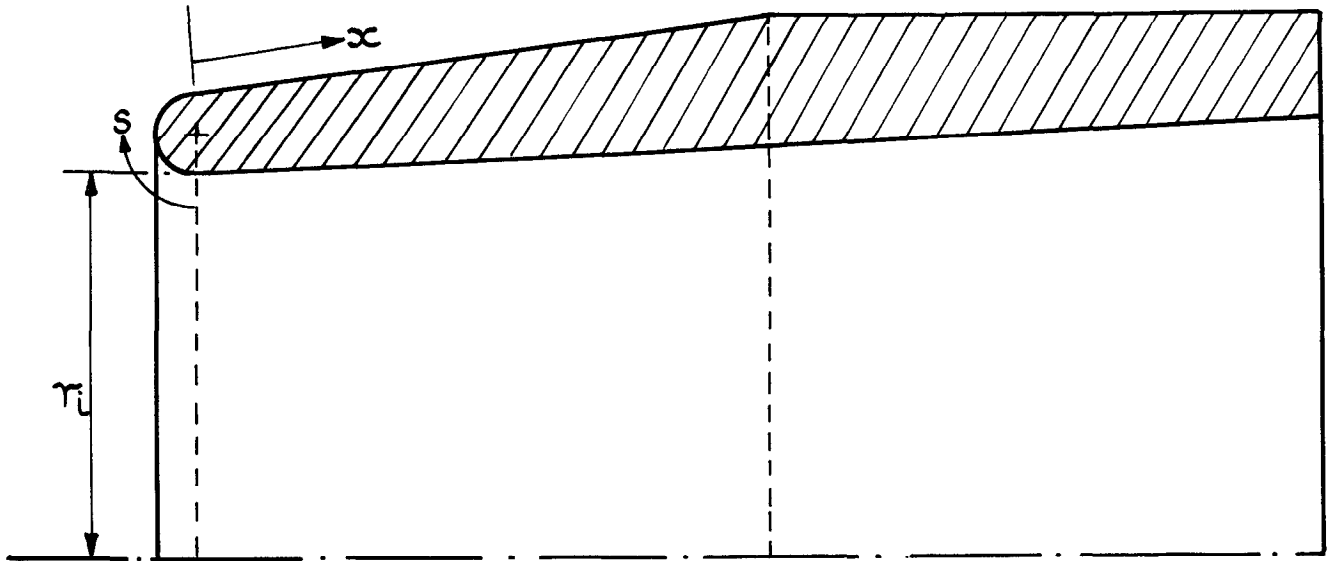
(d) $M_0 = 1.42$, $R_N = 1.6 \times 10^6$

FIG. 3 (CONT.) - COWL EXTERNAL PRESSURE DISTRIBUTION, 12° LIP COWL.



(e) $M_o = 1.82$, $R_N = 1.6 \times 10^6$

FIG. 3. (CONCLUDED) COWL EXTERNAL PRESSURE DISTRIBUTION, 12° LIP COWL.



(a) $M_0 = 0.80$, $R_N = 1.6 \times 10^6$

FIG. 4. COWL EXTERNAL PRESSURE DISTRIBUTION, BLUNT LIP COWL.

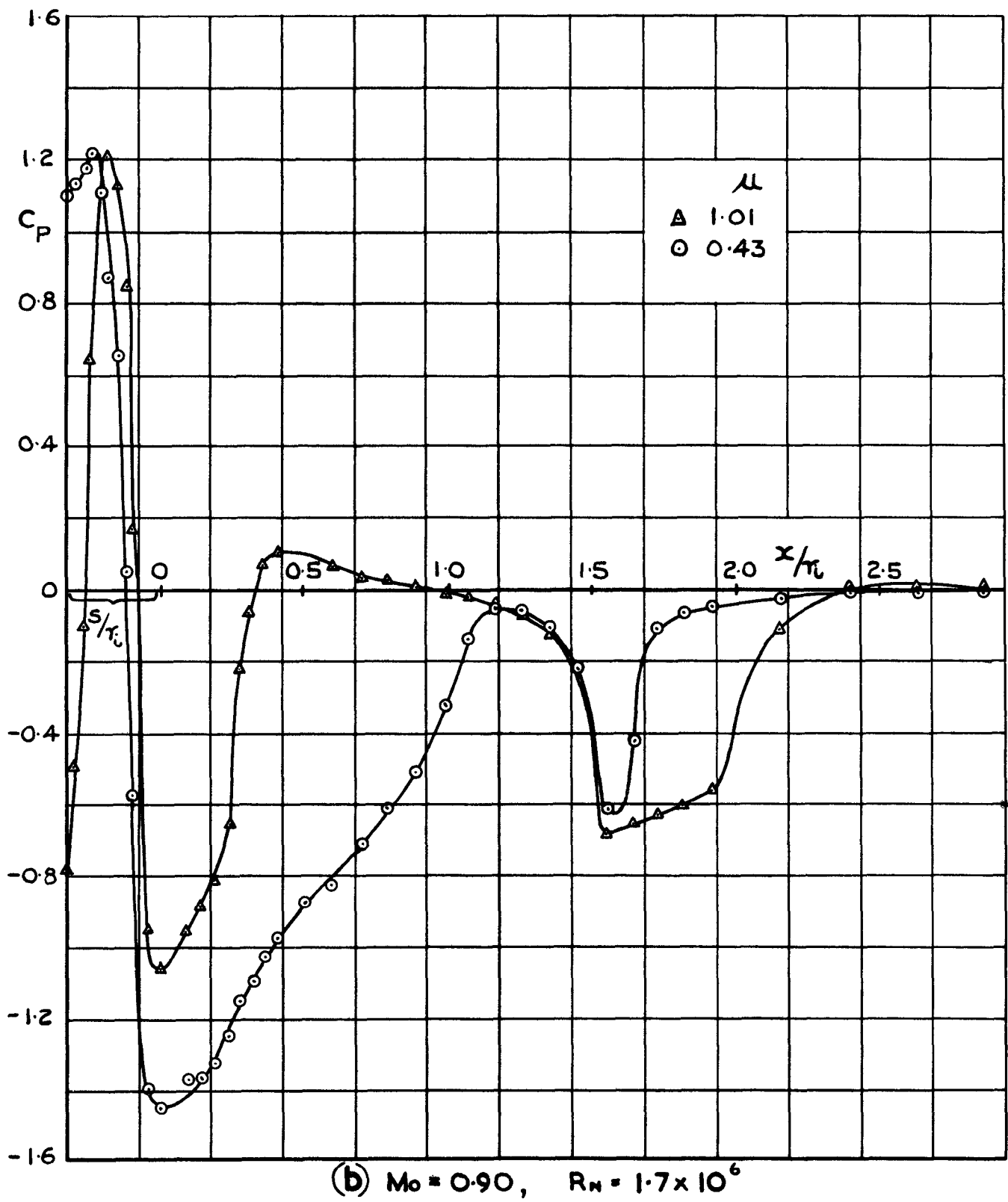


FIG.4.(CONT) COWL EXTERNAL PRESSURE DISTRIBUTION, BLUNT LIP COWL.

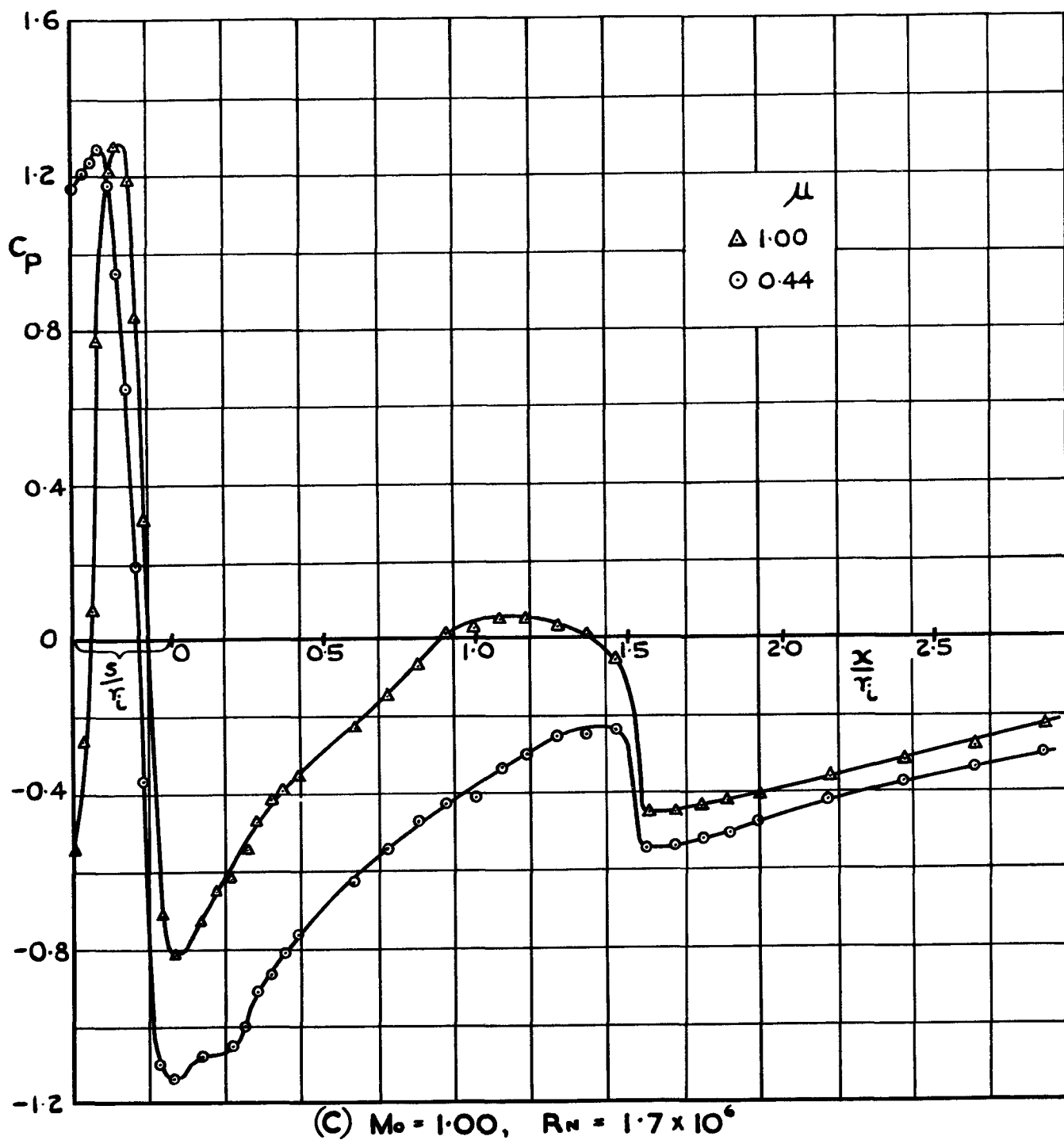
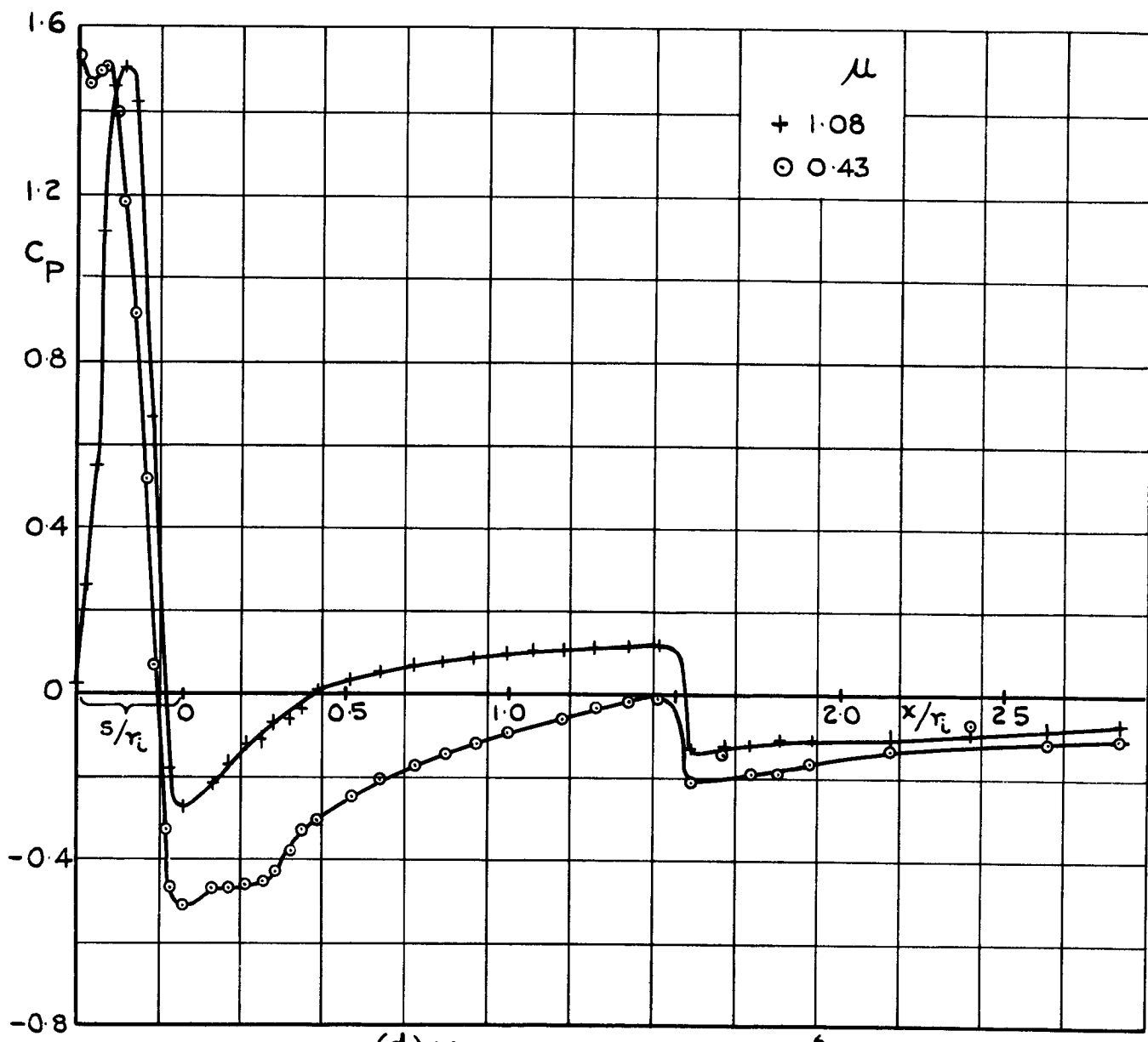
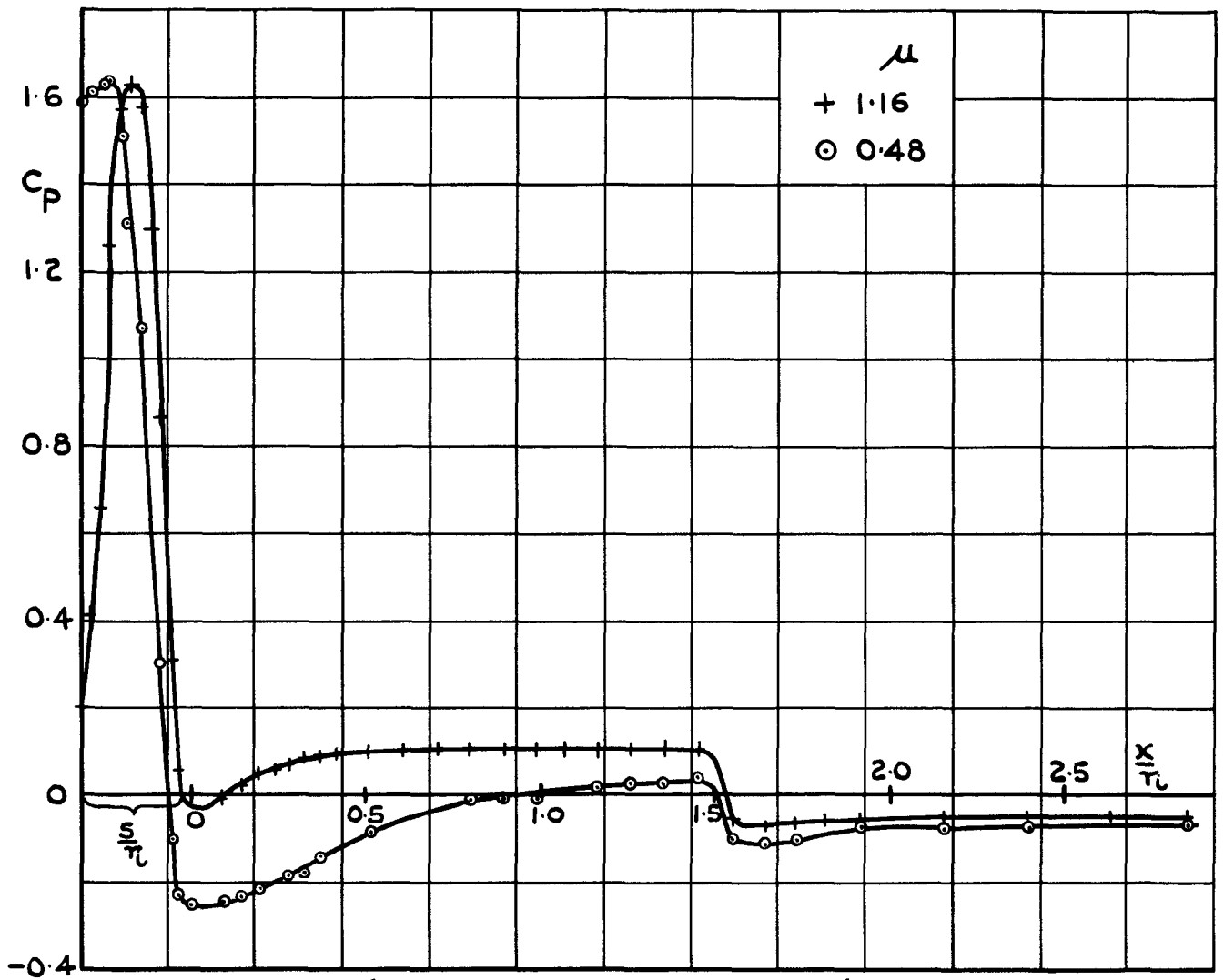


FIG.4. (CONT) COWL EXTERNAL PRESSURE DISTRIBUTION, BLUNT LIP COWL.



(d) $M_0 = 1.42, R_N = 1.5 \times 10^6$

FIG. 4. (CONT.) COWL EXTERNAL PRESSURE DISTRIBUTION, BLUNT LIP COWL.



(e) $M_0 = 1.82$, $R_N = 1.6 \times 10^6$

FIG.4.(CONCLUDED) COWL EXTERNAL PRESSURE DISTRIBUTION, BLUNT LIP COWL.

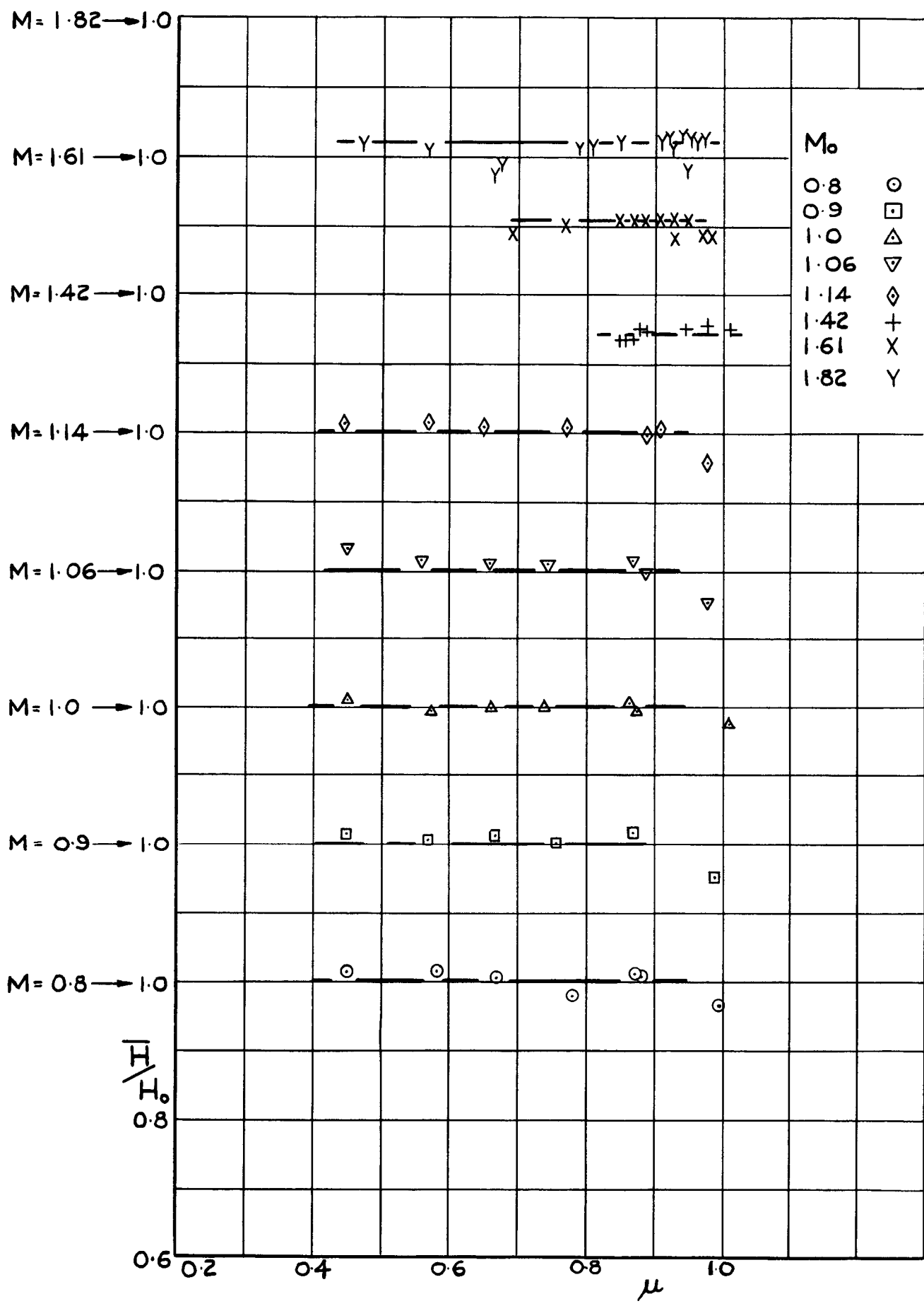


FIG.5. INTERNAL PRESSURE RECOVERY, 7.6° COWL.

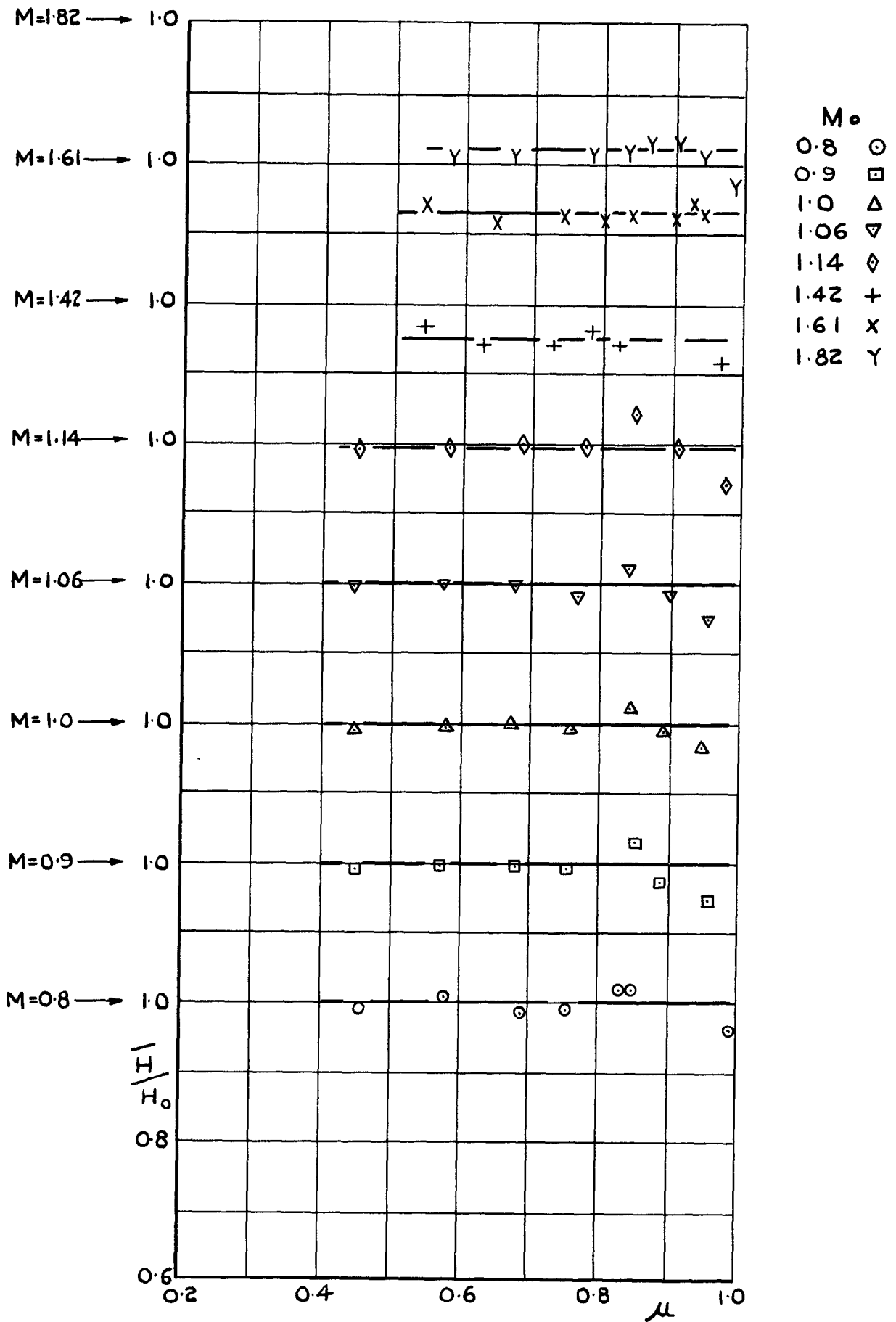


FIG. 6. INTERNAL PRESSURE RECOVERY, 12° COWL.

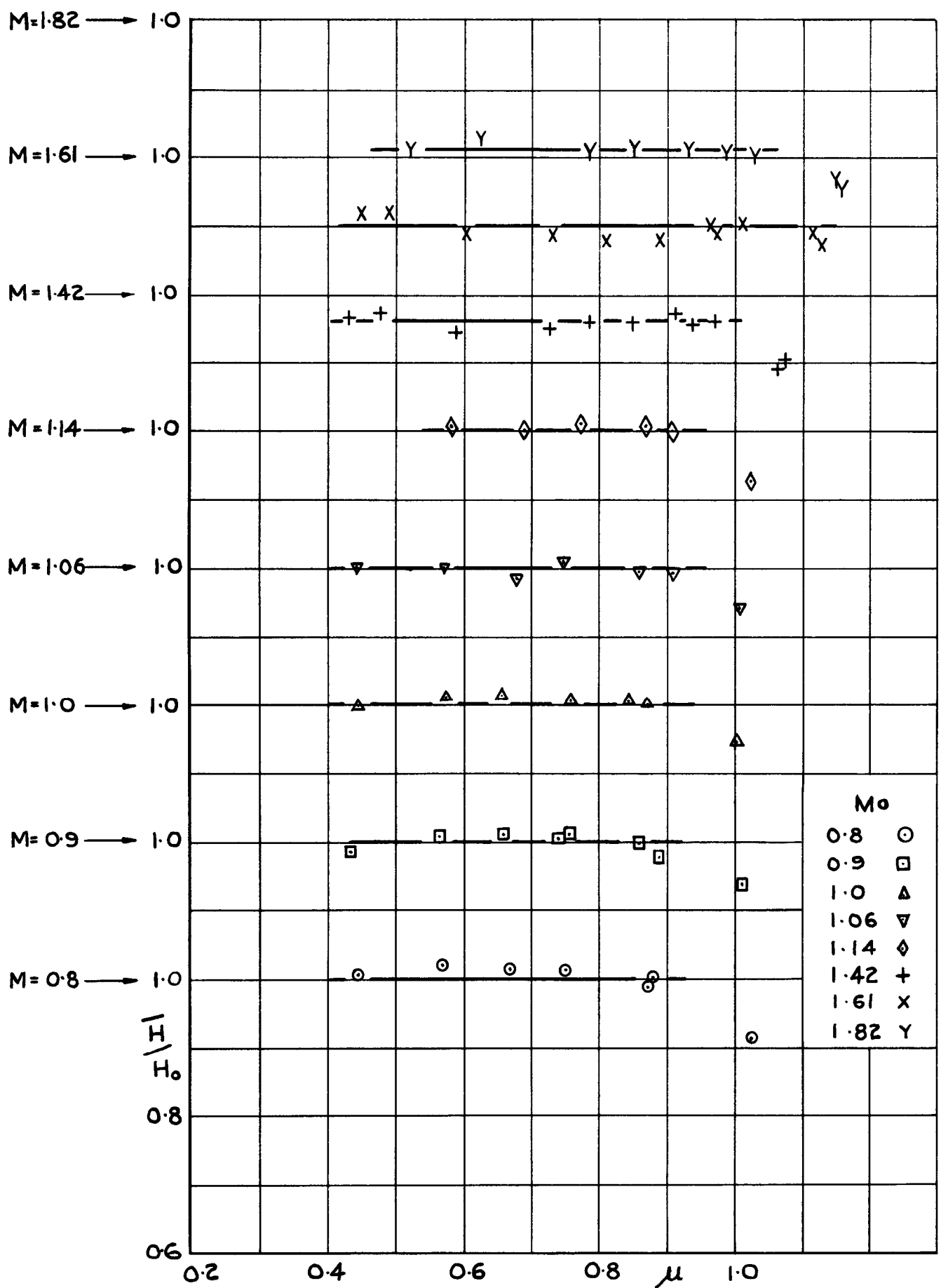


FIG. 7. INTERNAL PRESSURE RECOVERY, BLUNT LIP COWL.

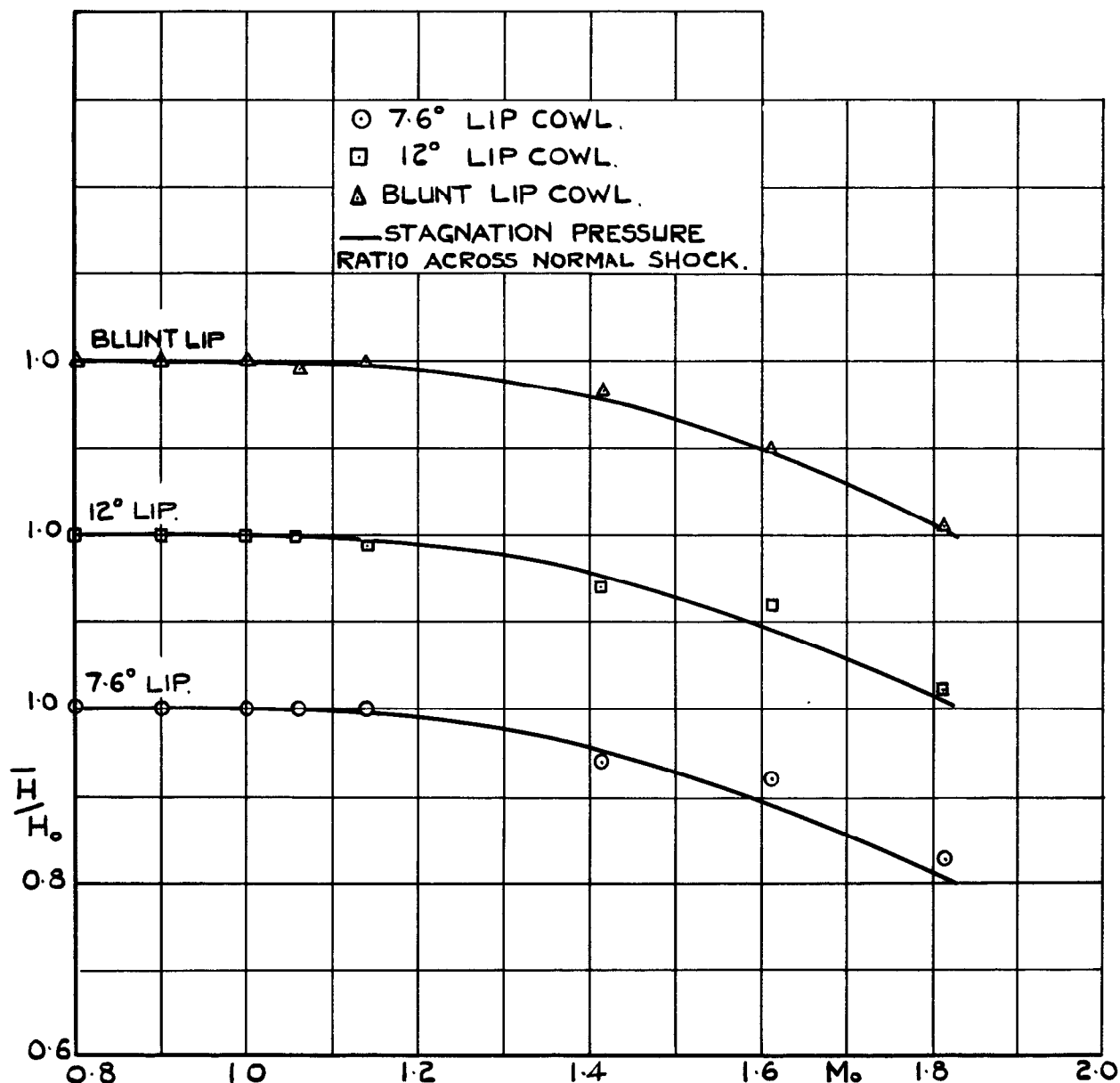


FIG.8. VARIATION OF INTERNAL PRESSURE RECOVERY WITH MACH No.

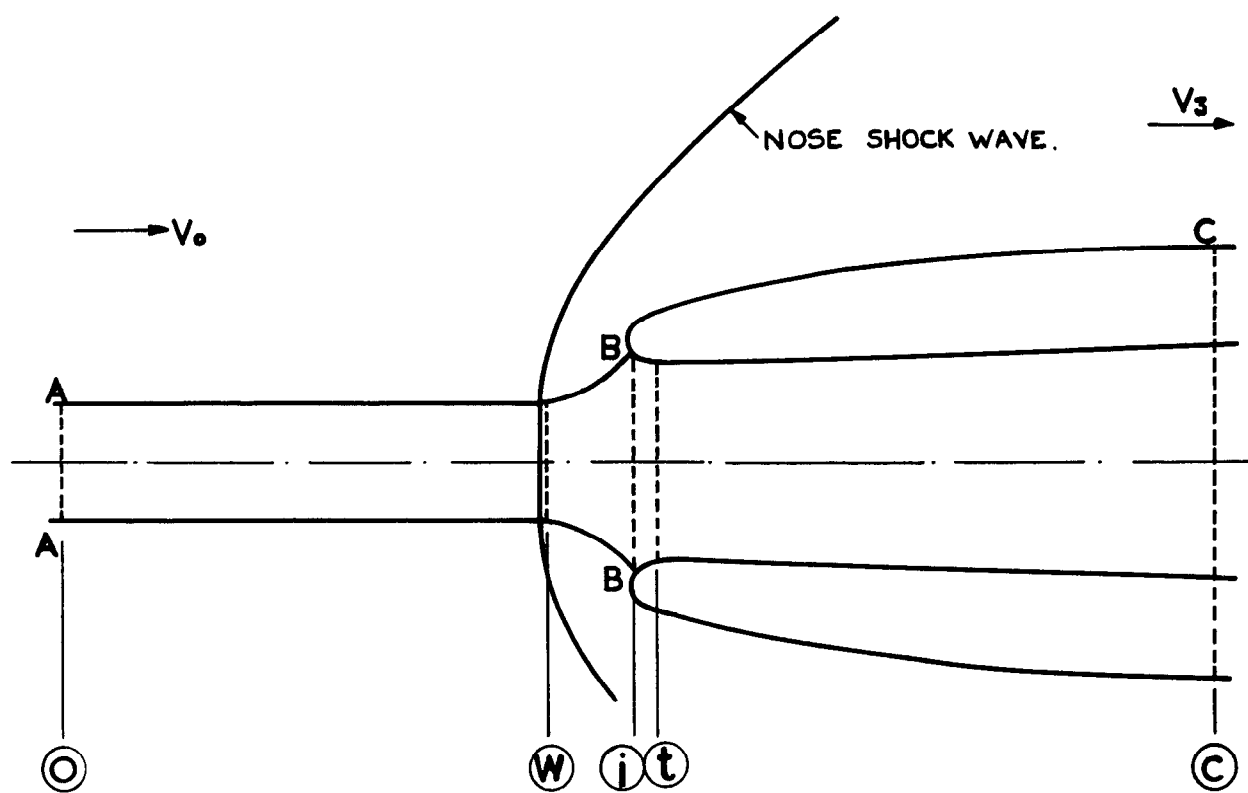


FIG.9. SKETCH OF THE FLOW PAST AN OPEN NOSE INTAKE.

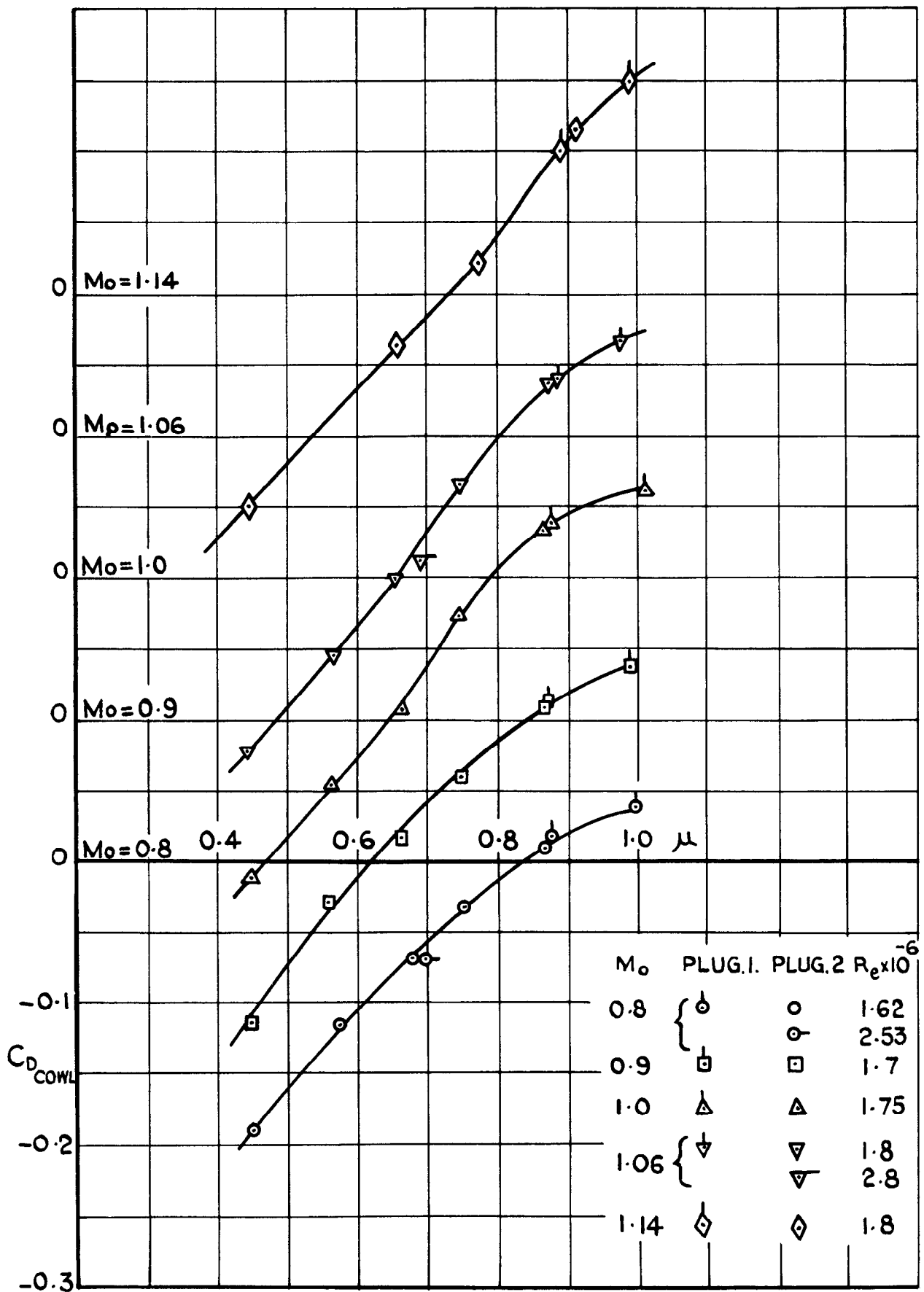


FIG 10. VARIATION OF $C_{D_{COWL}}$ WITH MASS FLOW RATIO, 7.6° LIP COWL.

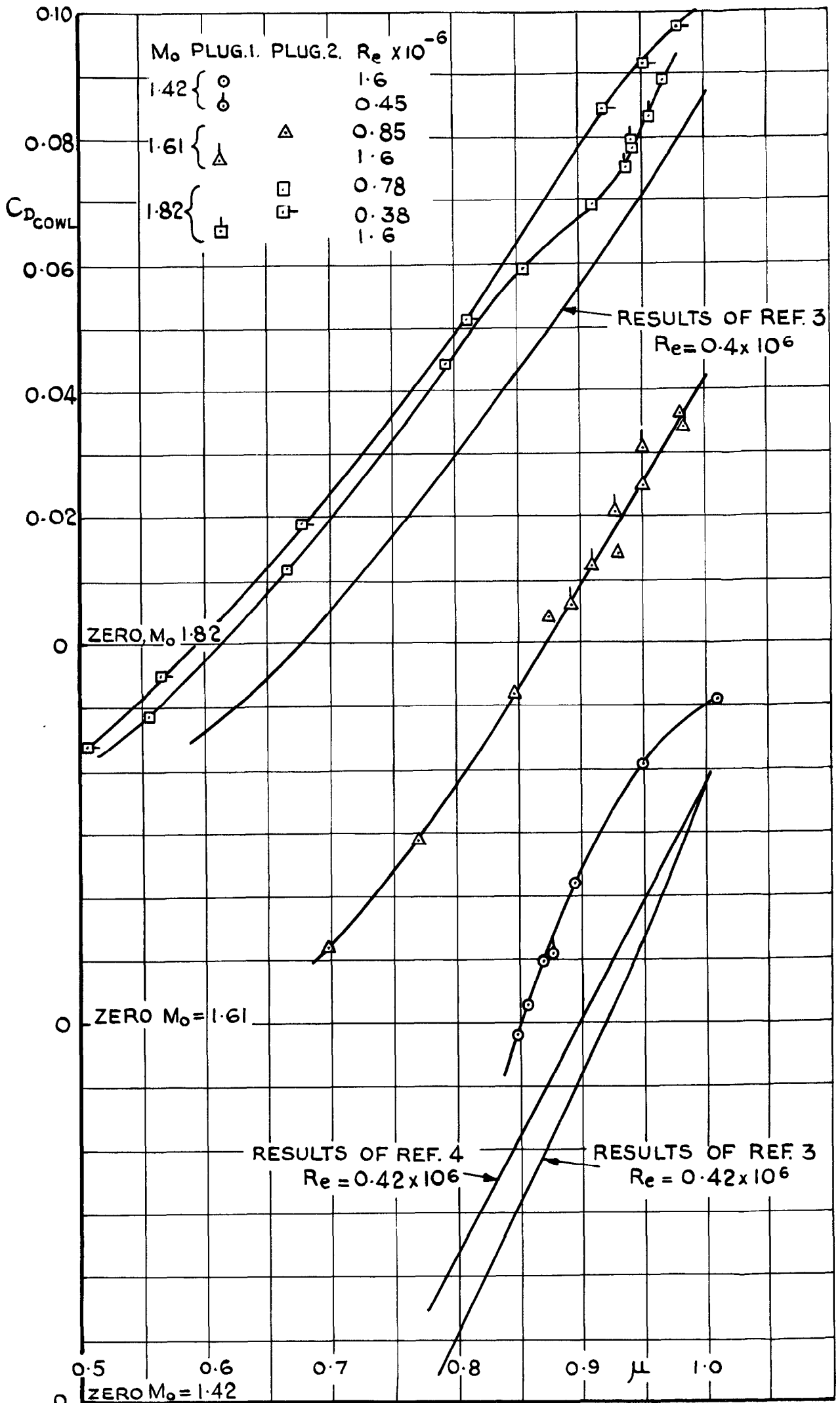


FIG.10. (CONCLUDED) VARIATION OF $C_{D\ COWL}$ WITH MASS FLOW RATIO, 7.6° LIP COWL.

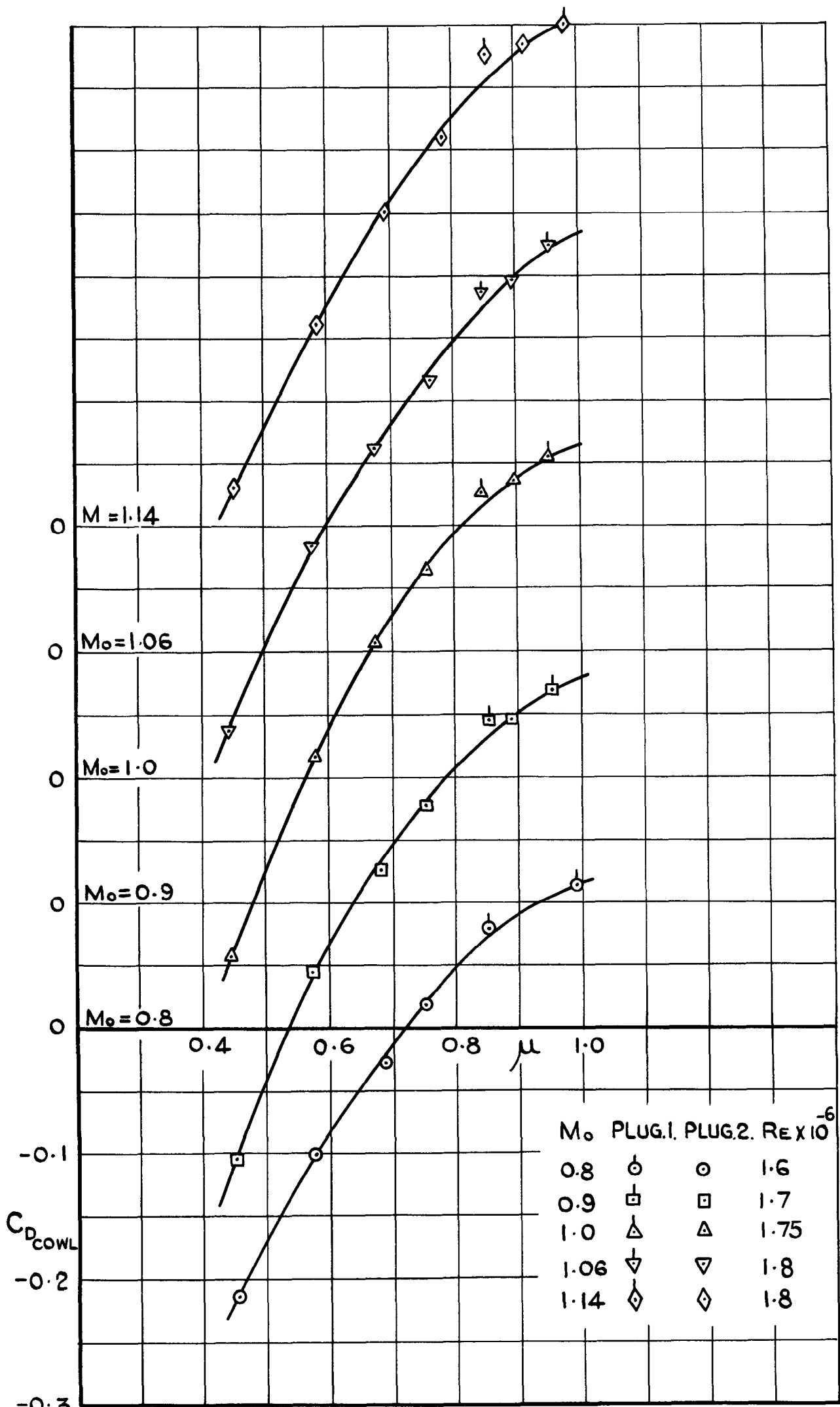


FIG. II. VARIATION OF $C_{D_{cowl}}$ WITH MASS FLOW RATIO, 12° LIP COWL.

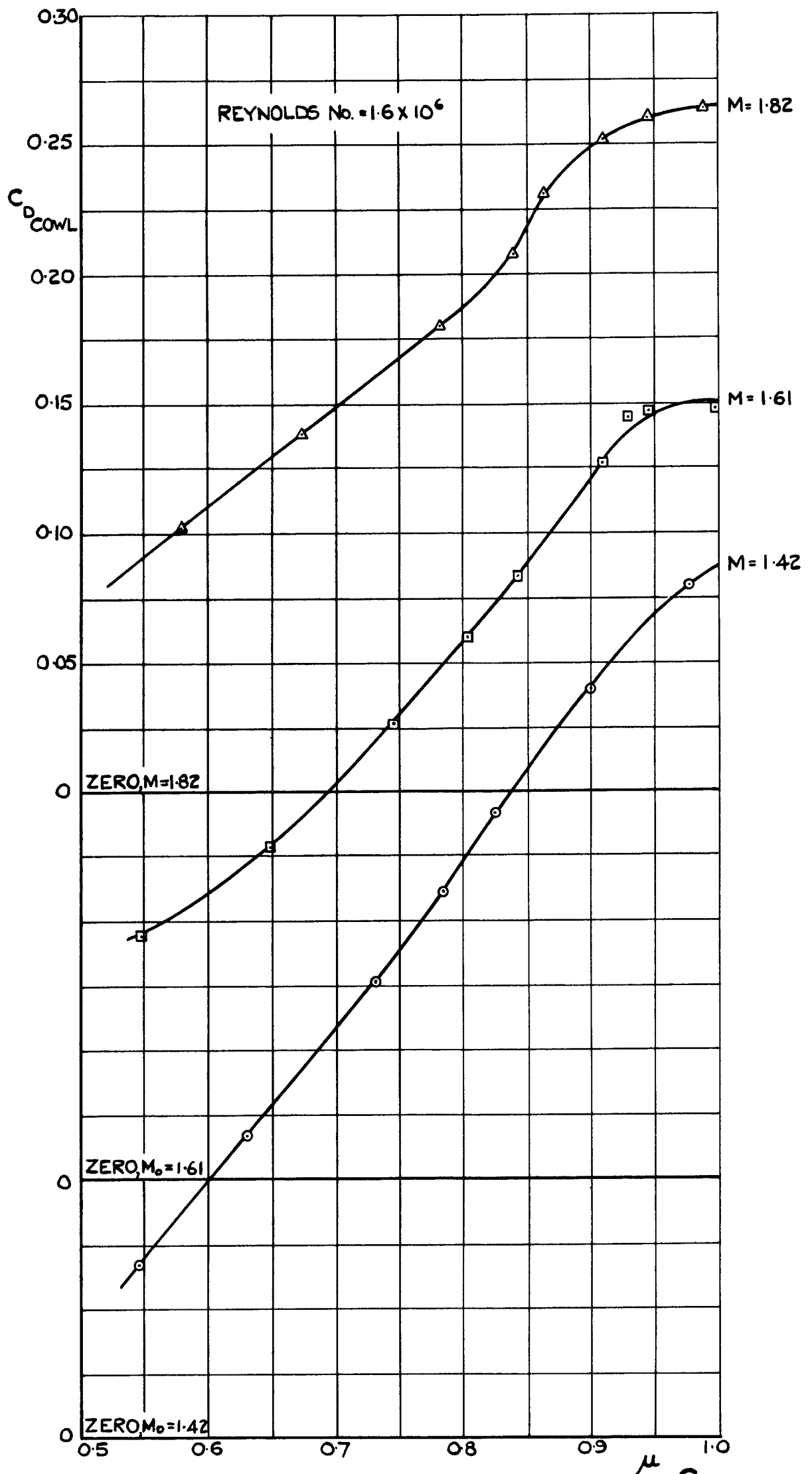


FIG. II. (CONCLUDED) VARIATION OF $C_{D_{COWL}}$ WITH MASS FLOW RATIO, 12° LIP COWL.

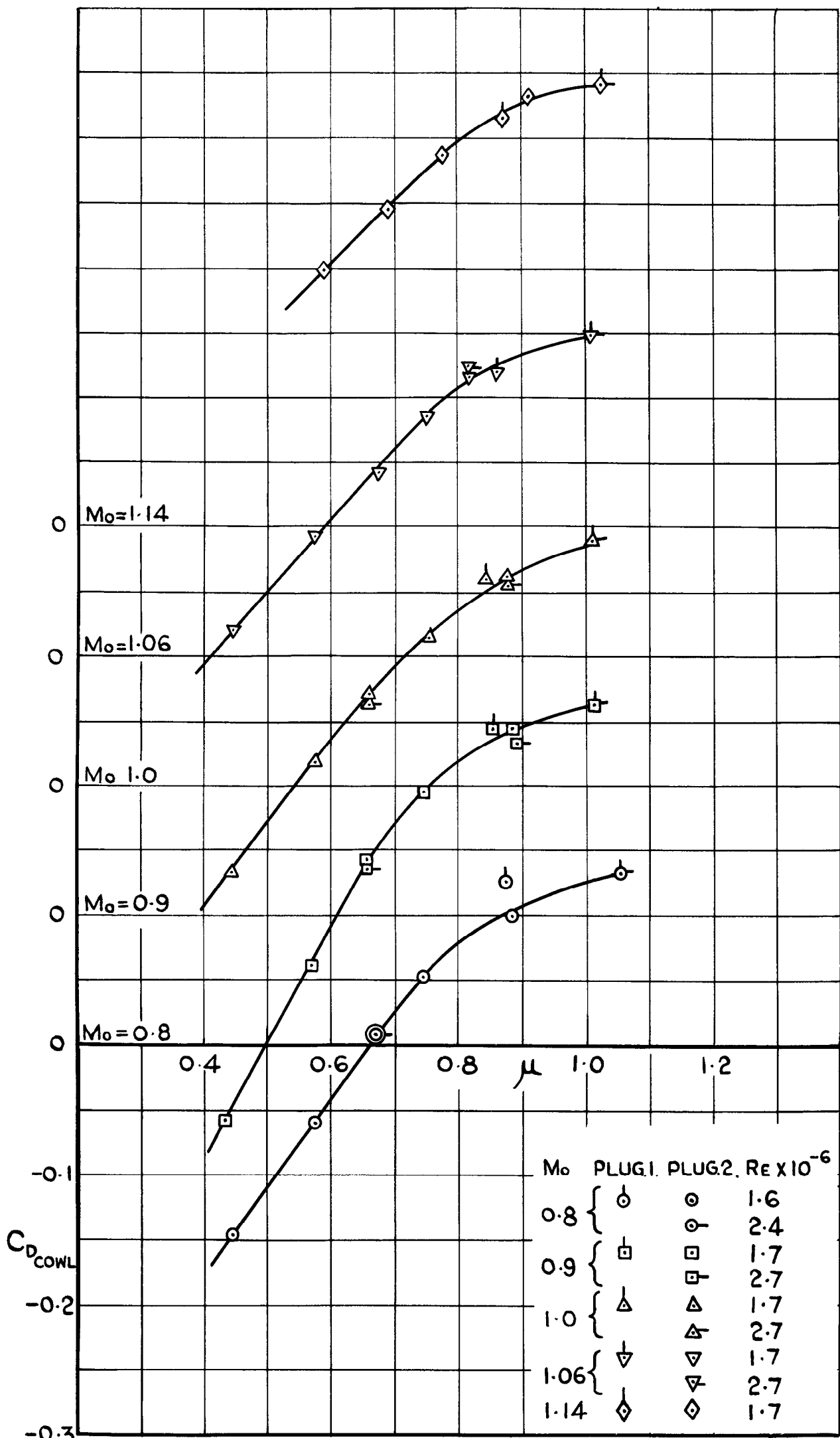


FIG.12. VARIATION OF $C_{D_{COWL}}$ WITH MASS FLOW RATIO, BLUNT LIP COWL.

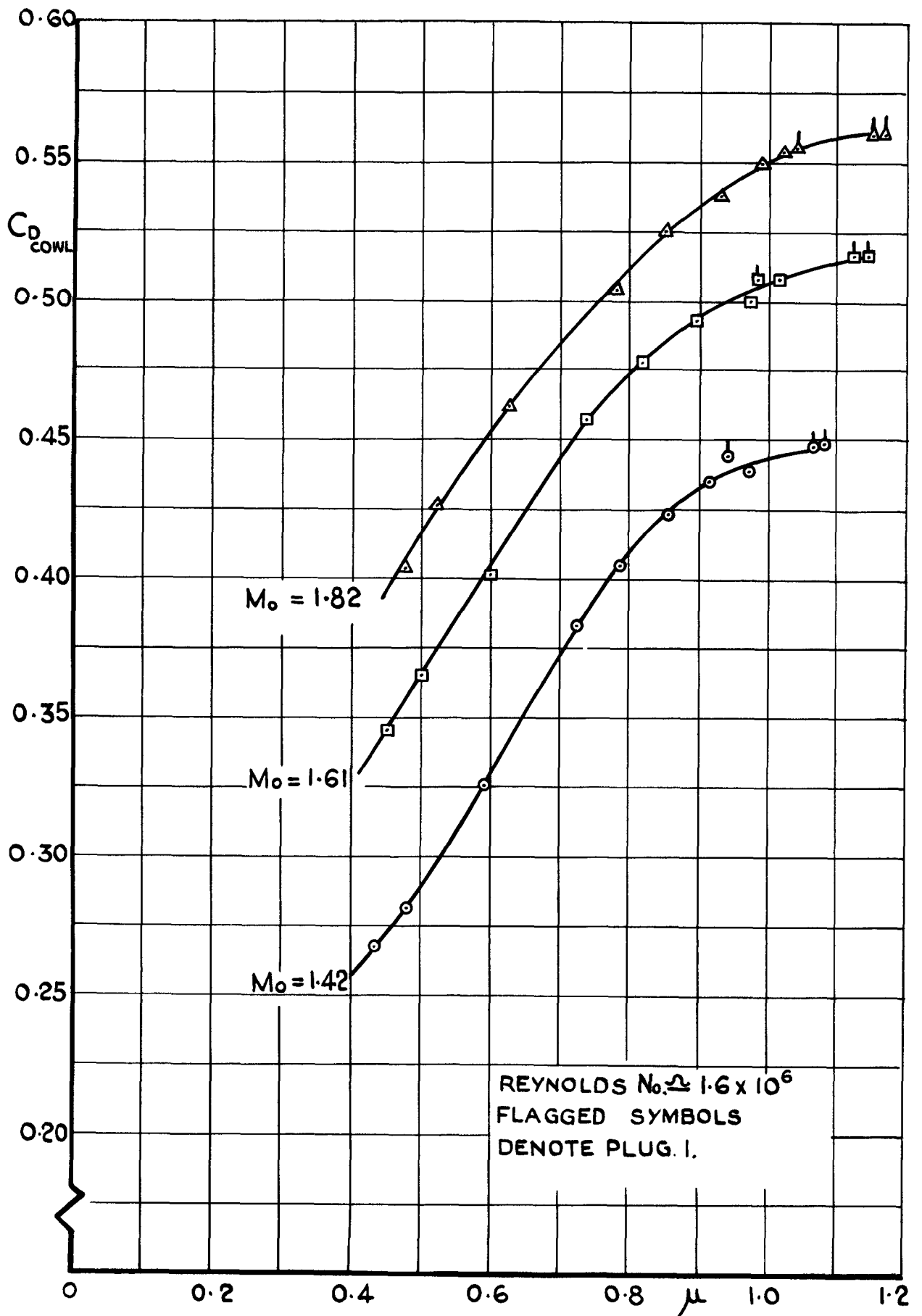
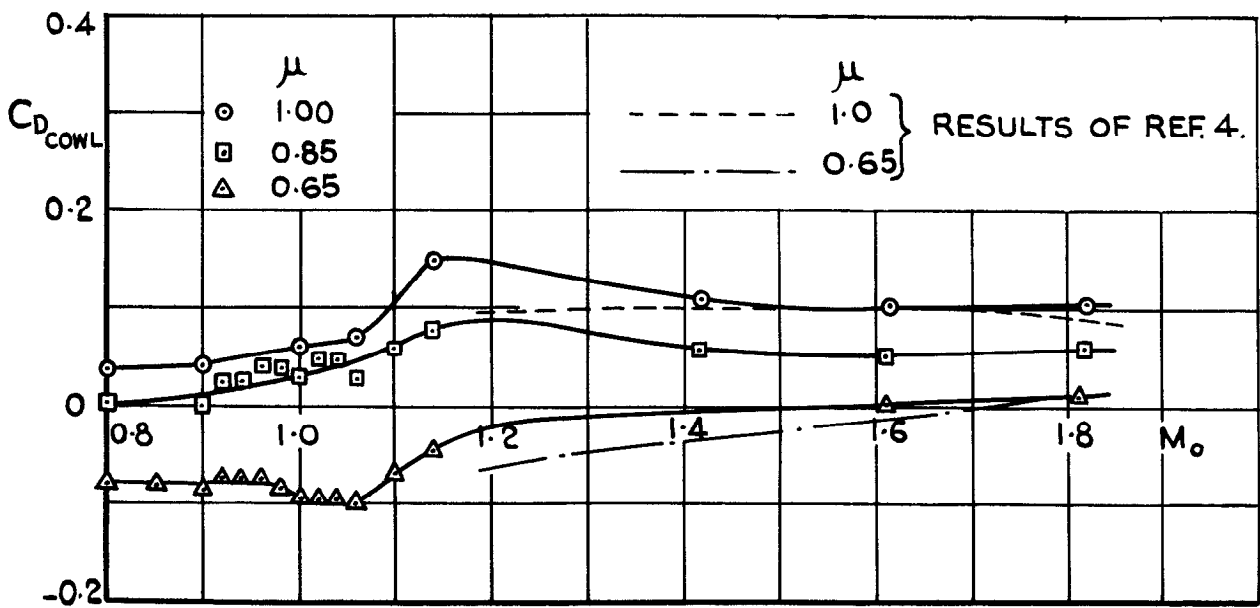
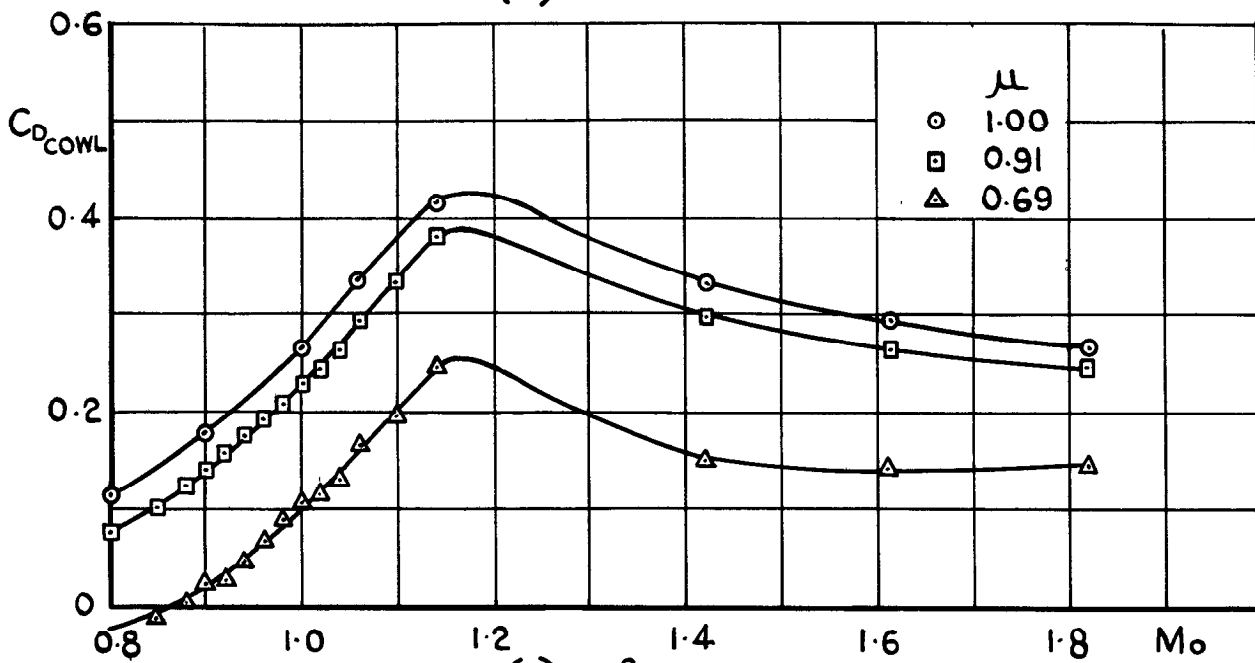


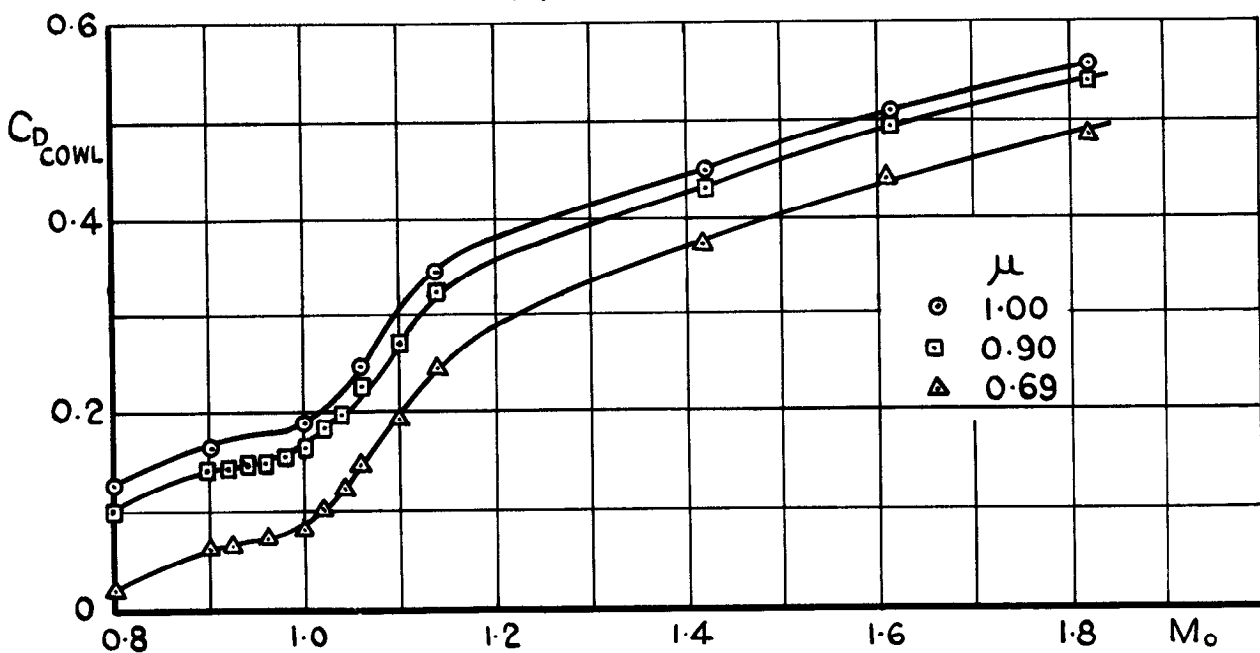
FIG.12. (CONCLUDED) VARIATION OF $C_{D_{cowl}}$ WITH MASS FLOW RATIO, BLUNT LIP COWL.



(a) 7.6 LIP COWL.



(b) 12° LIP COWL.



(c) BLUNT LIP COWL.

FIG. 13. VARIATION OF $C_{D_{cowl}}$ WITH MACH No. AT CONSTANT MASS FLOW RATIO.

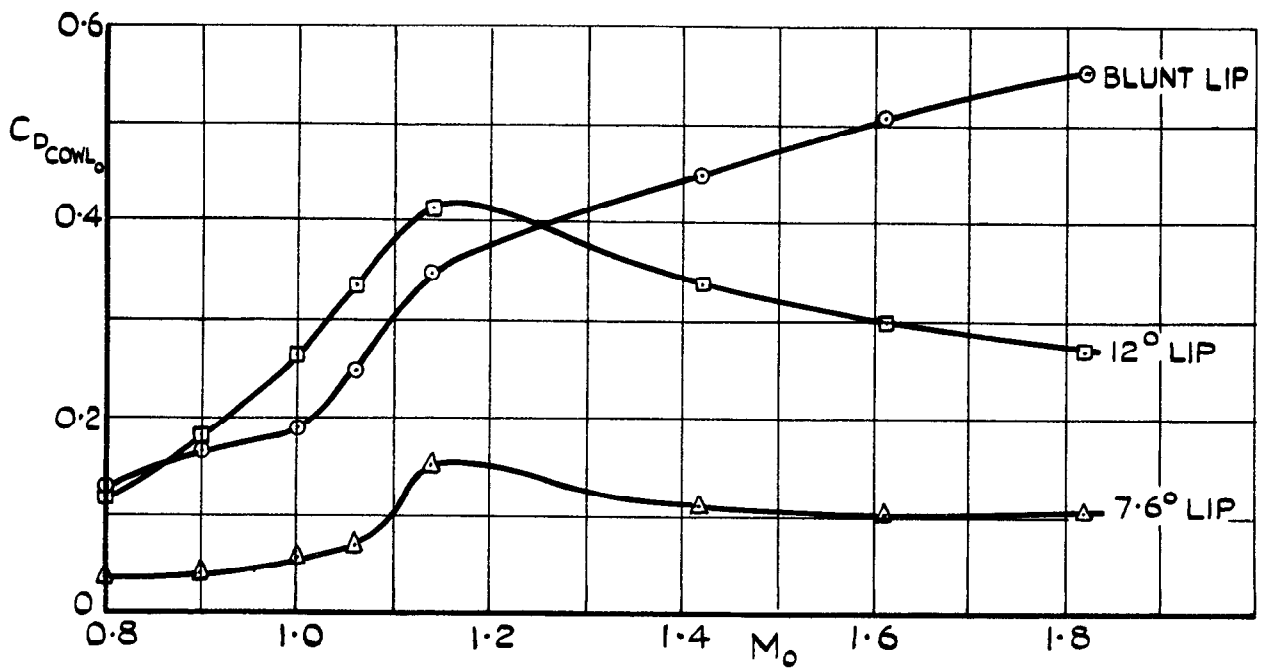


FIG. 14. VARIATION OF $C_{D_{COWL_0}}$ WITH MACH No. FOR THE THREE COWLS ($\mu = 1$)

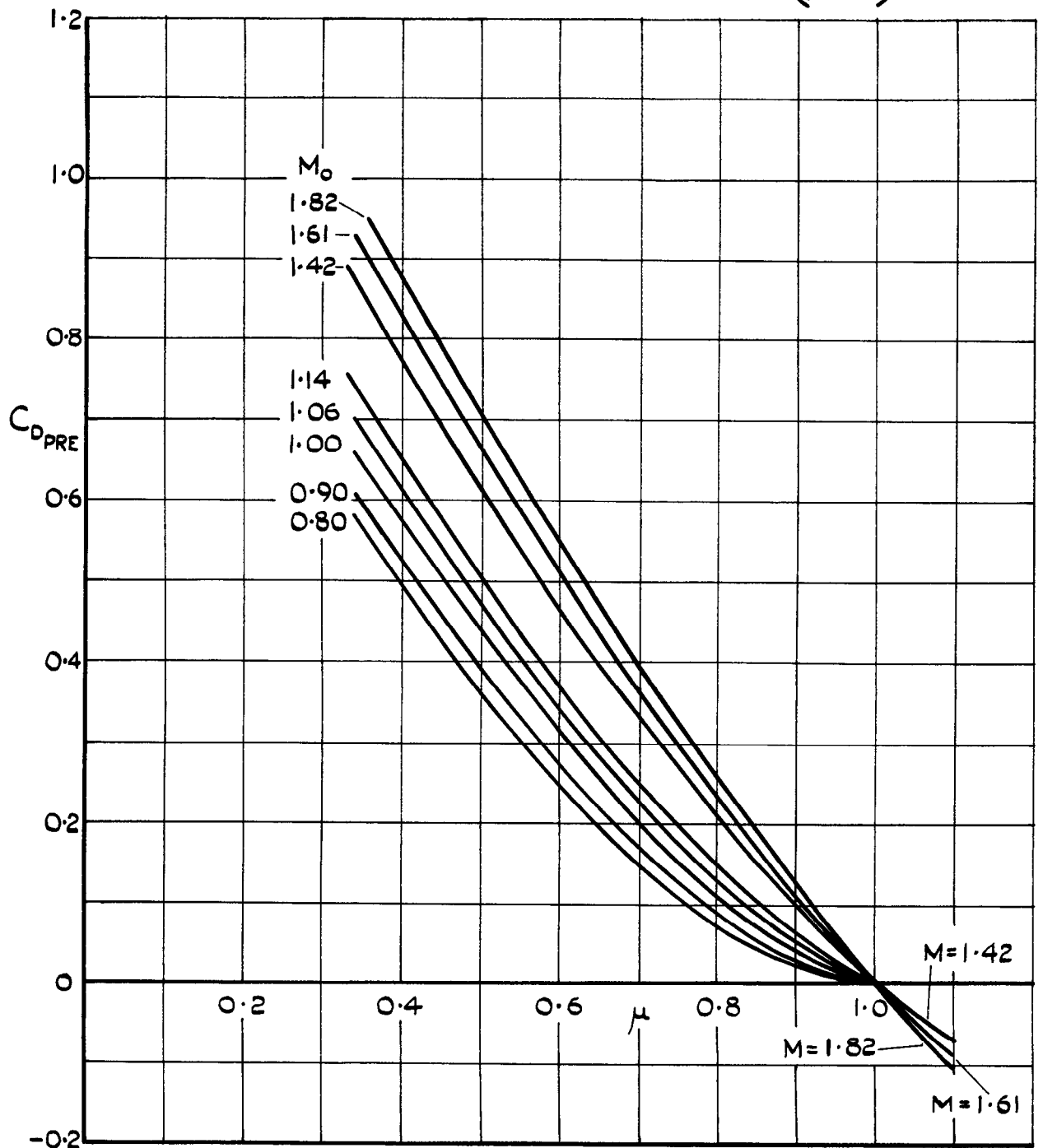
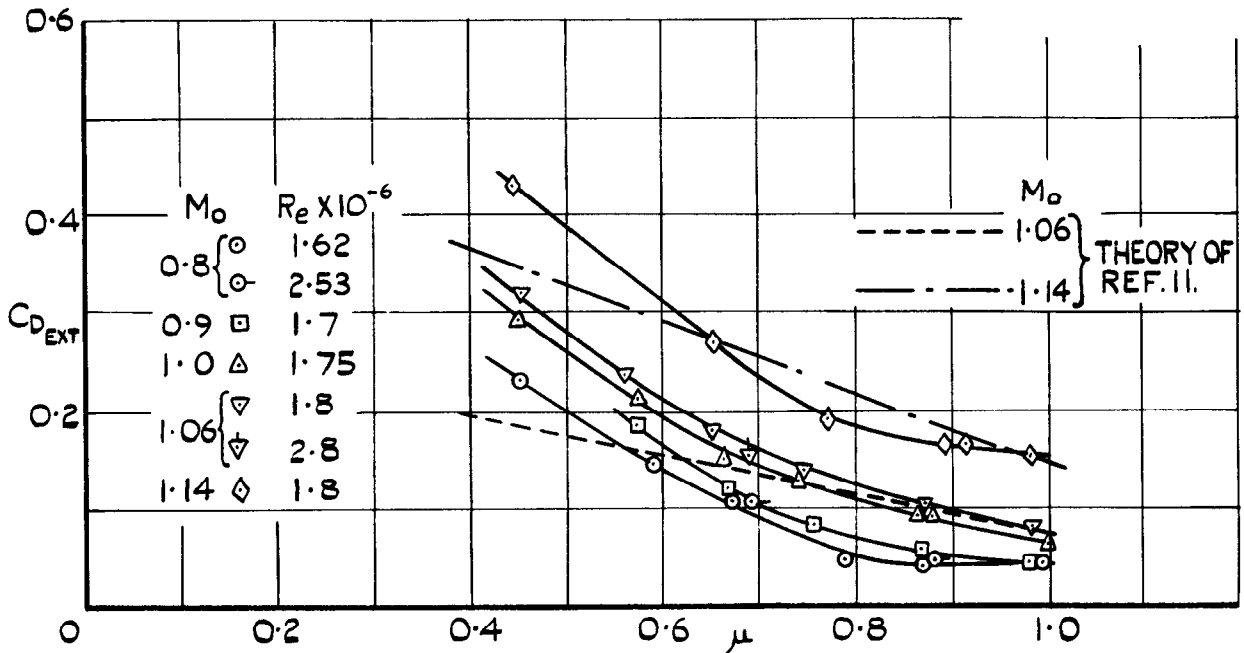
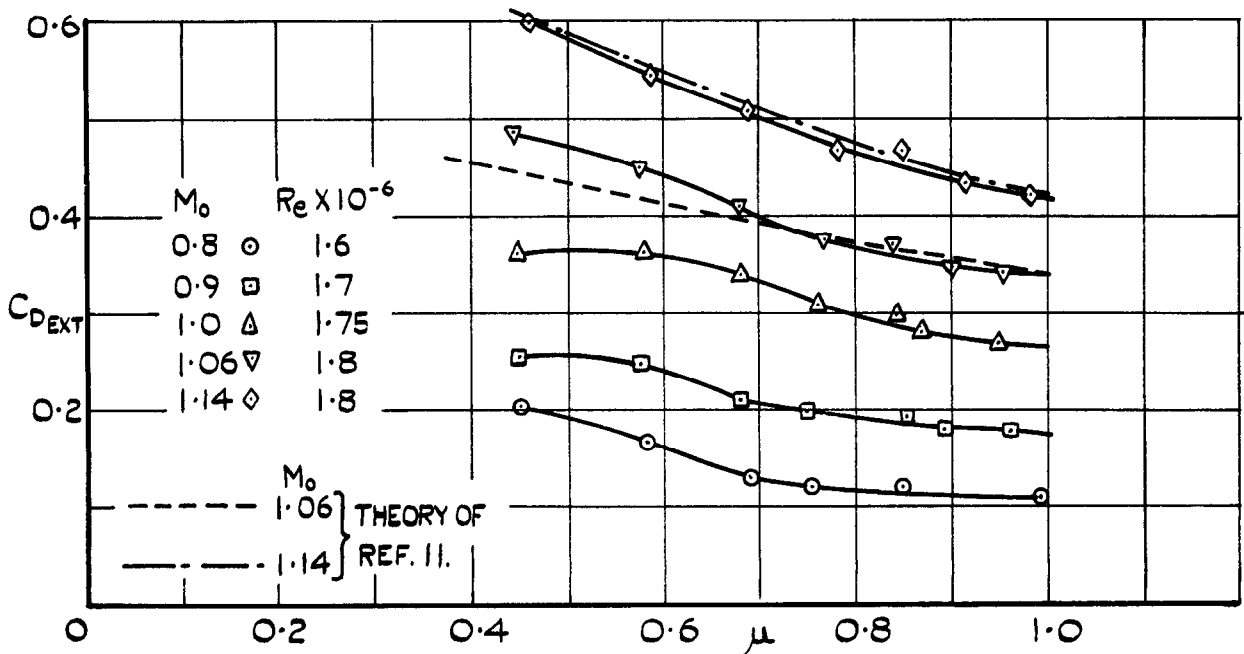


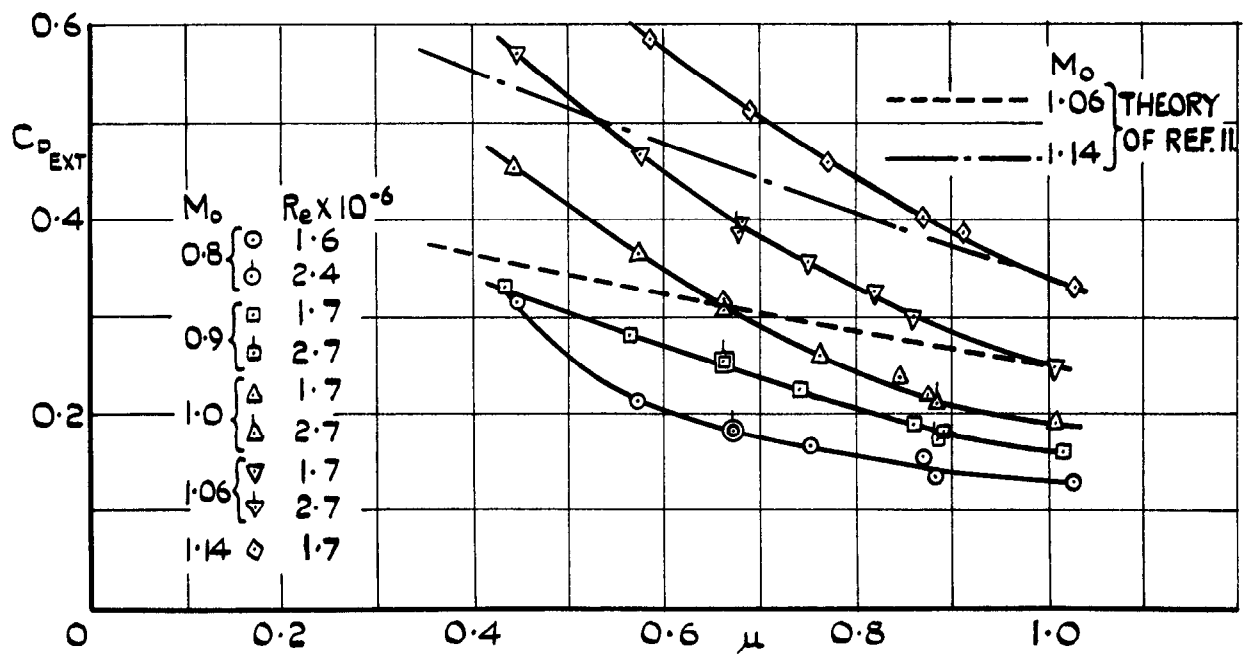
FIG. 15. VARIATION OF $C_{D_{PRE}}$ WITH MASS FLOW RATIO (CALCULATED)



(a) 7.6° LIP COWL.



(b) 12° LIP COWL.



(c) BLUNT LIP COWL.

FIG. 16. VARIATION OF EXTERNAL DRAG OF INTAKES WITH MASS FLOW.

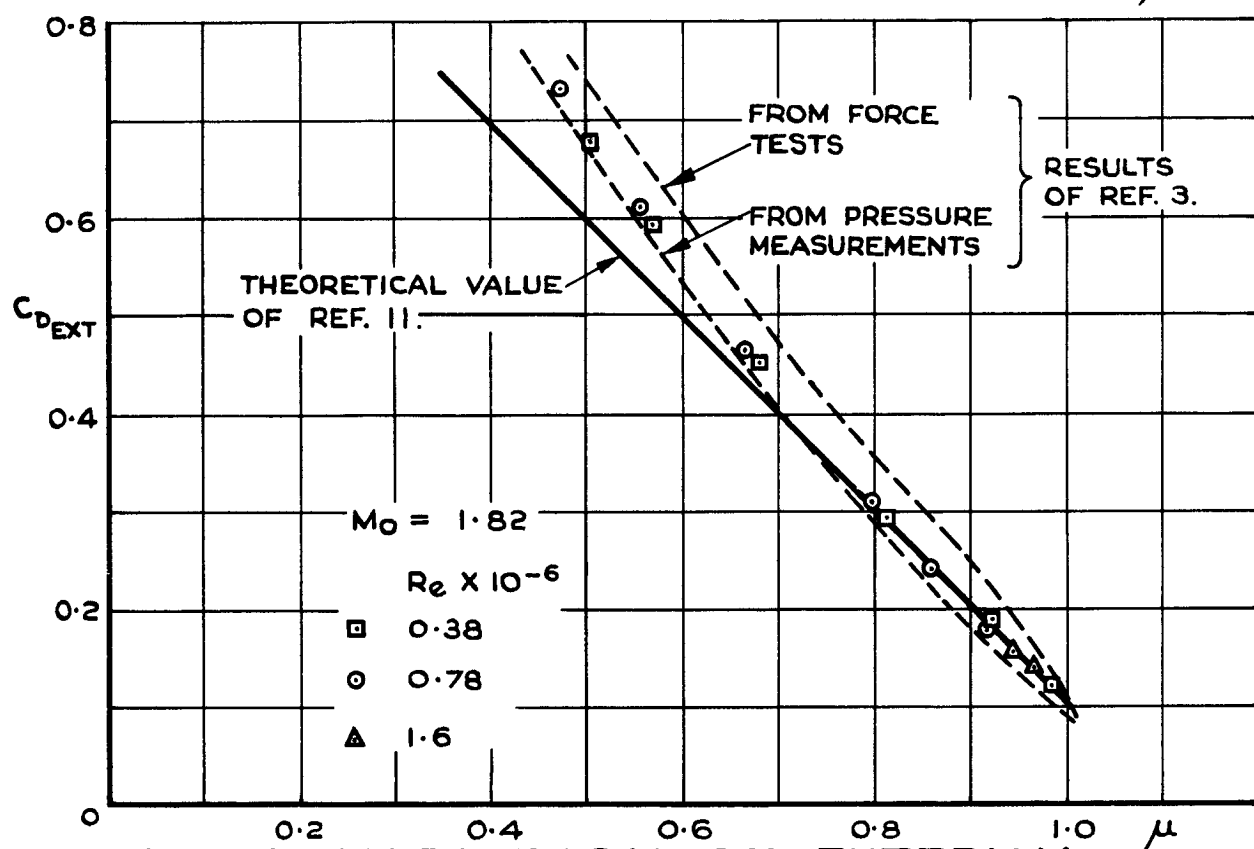
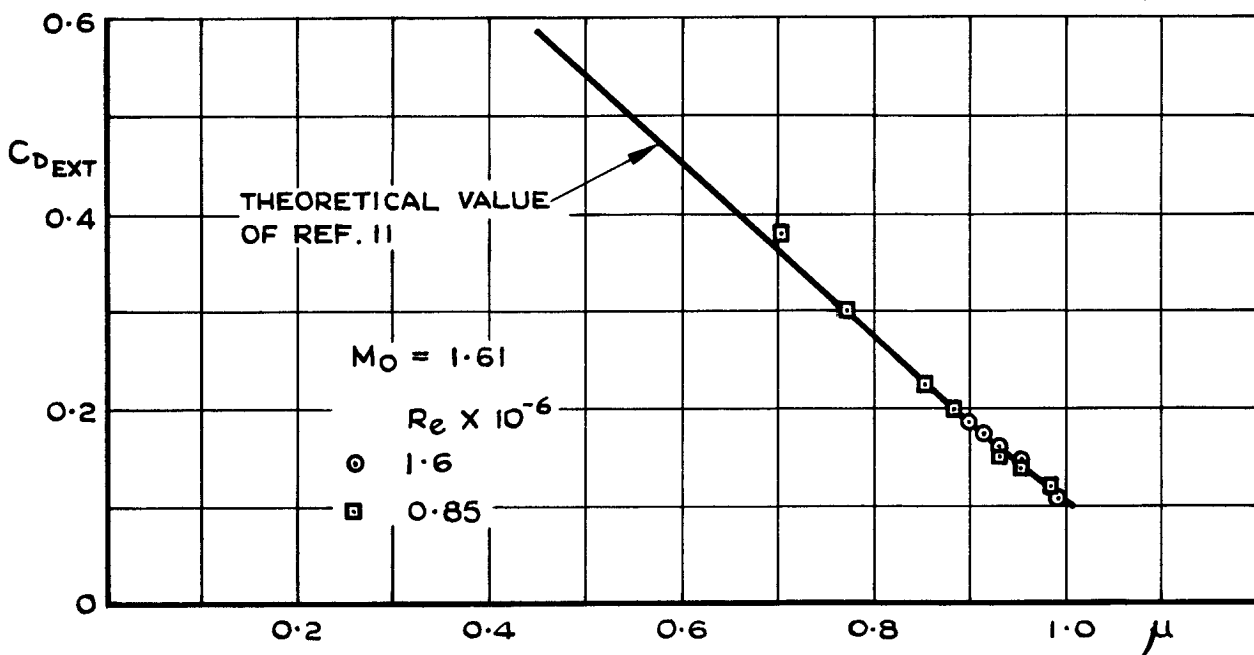
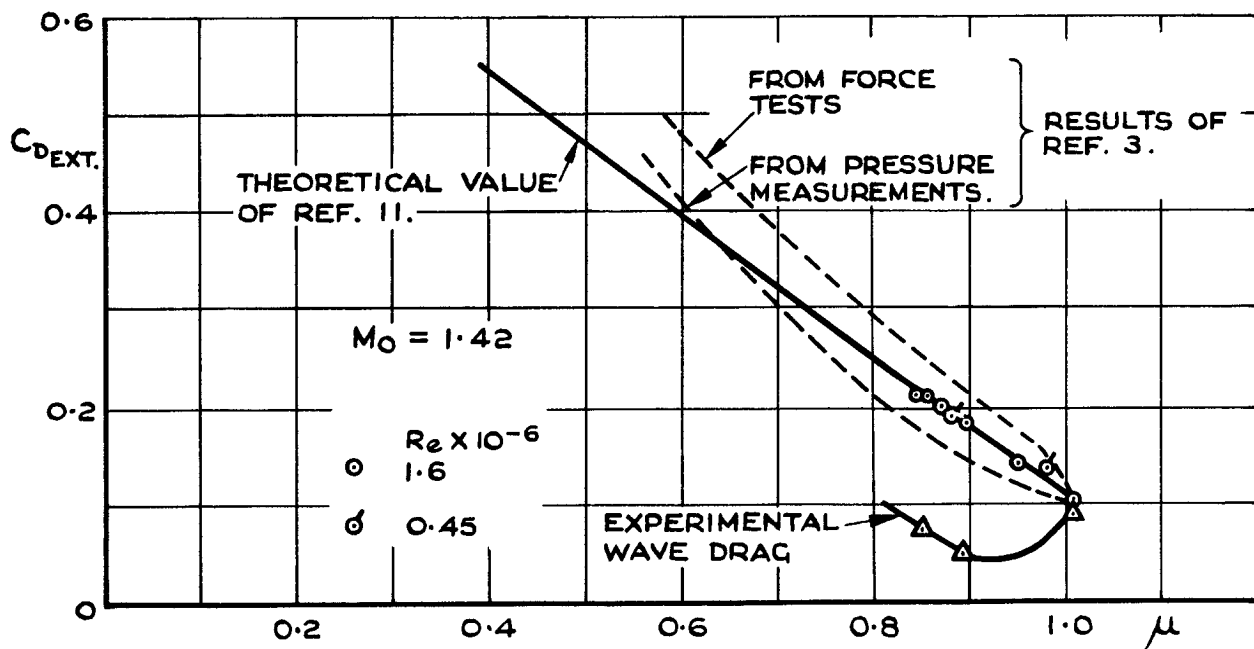


FIG. 17 - VARIATION OF EXTERNAL DRAG WITH MASS FLOW, 7.6° LIP COWL.

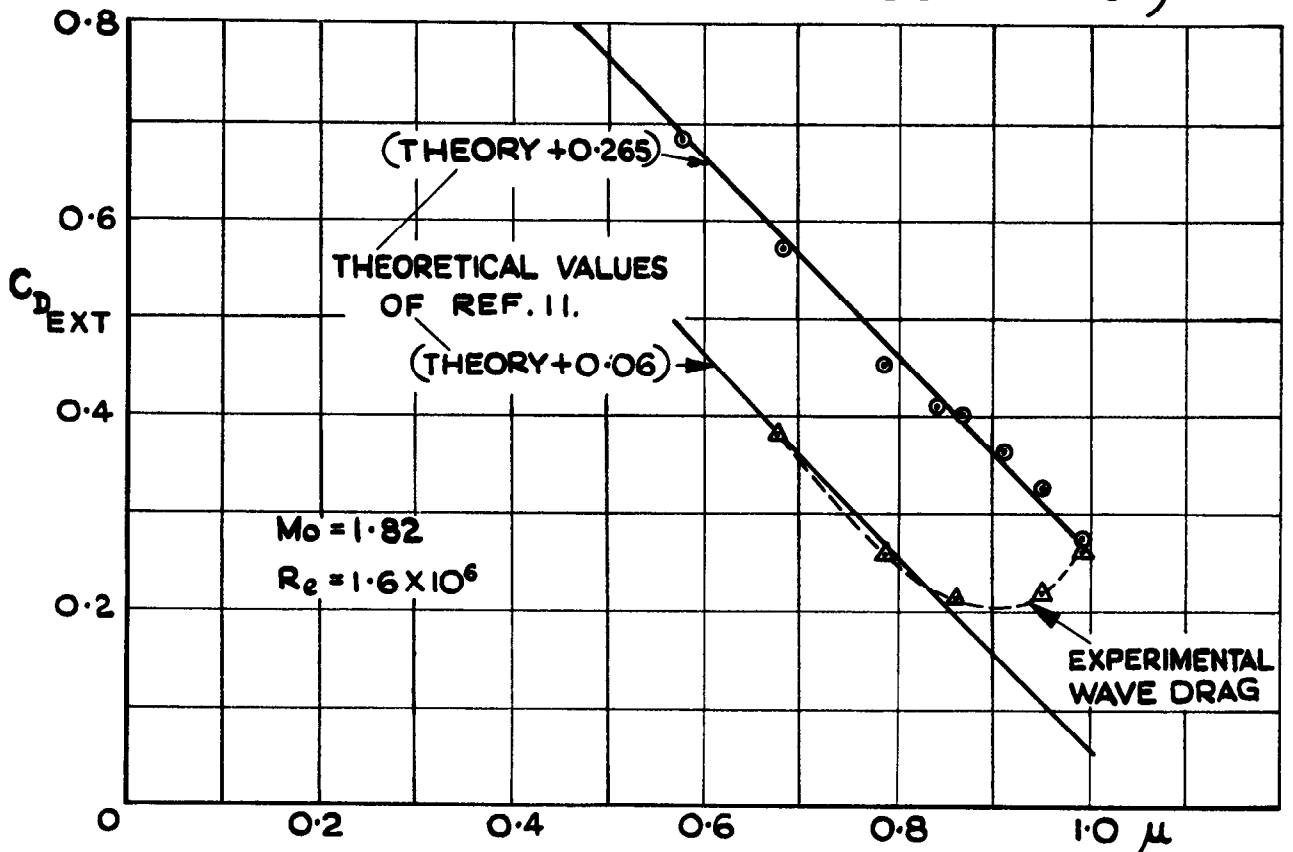
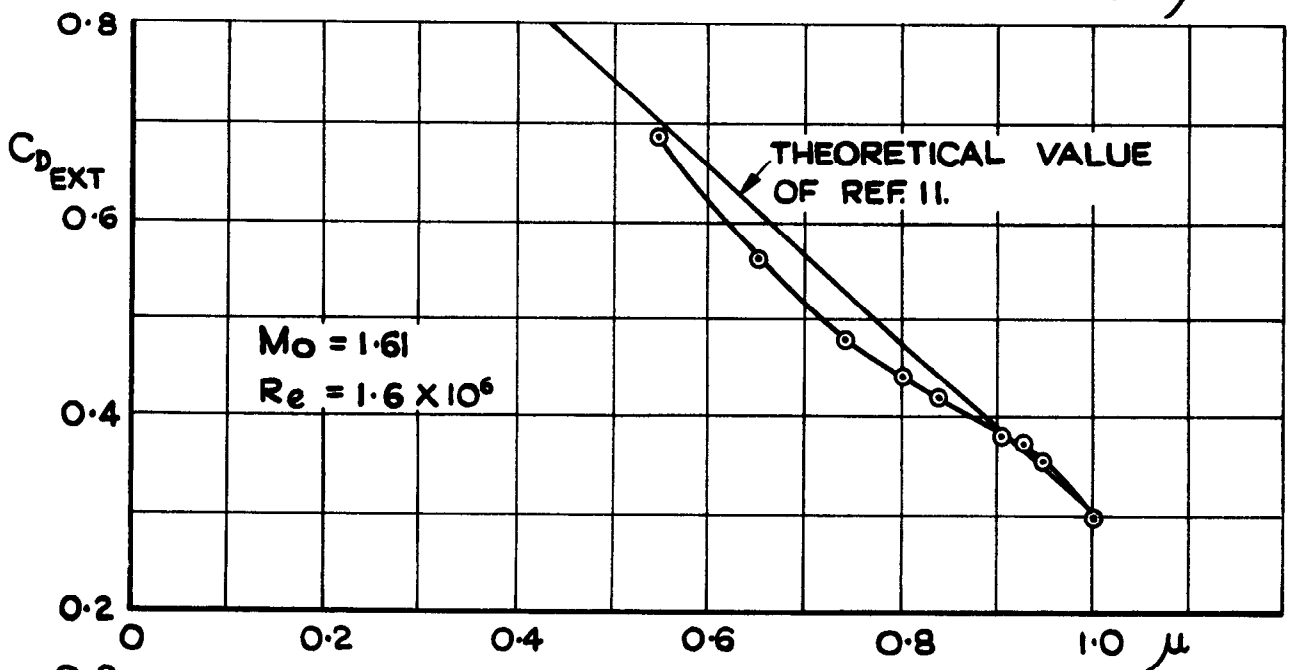
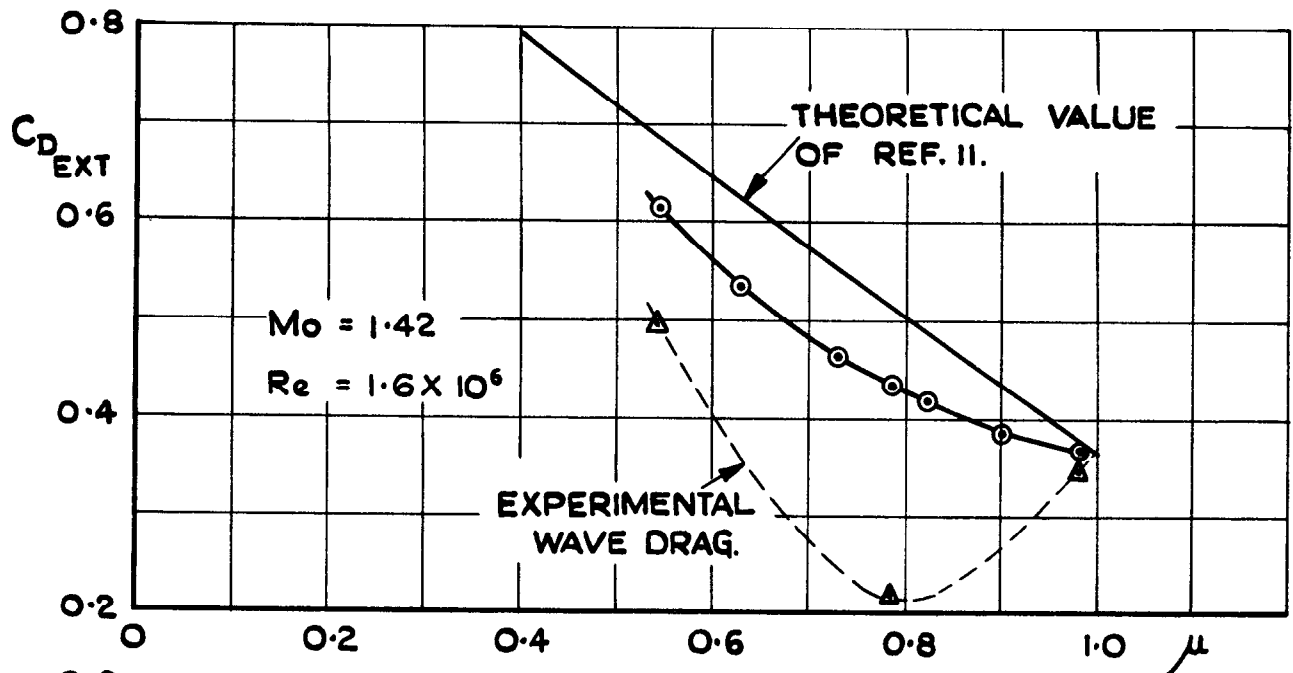


FIG.18. VARIATION OF EXTERNAL DRAG WITH MASS FLOW, 12° LIP COWL.

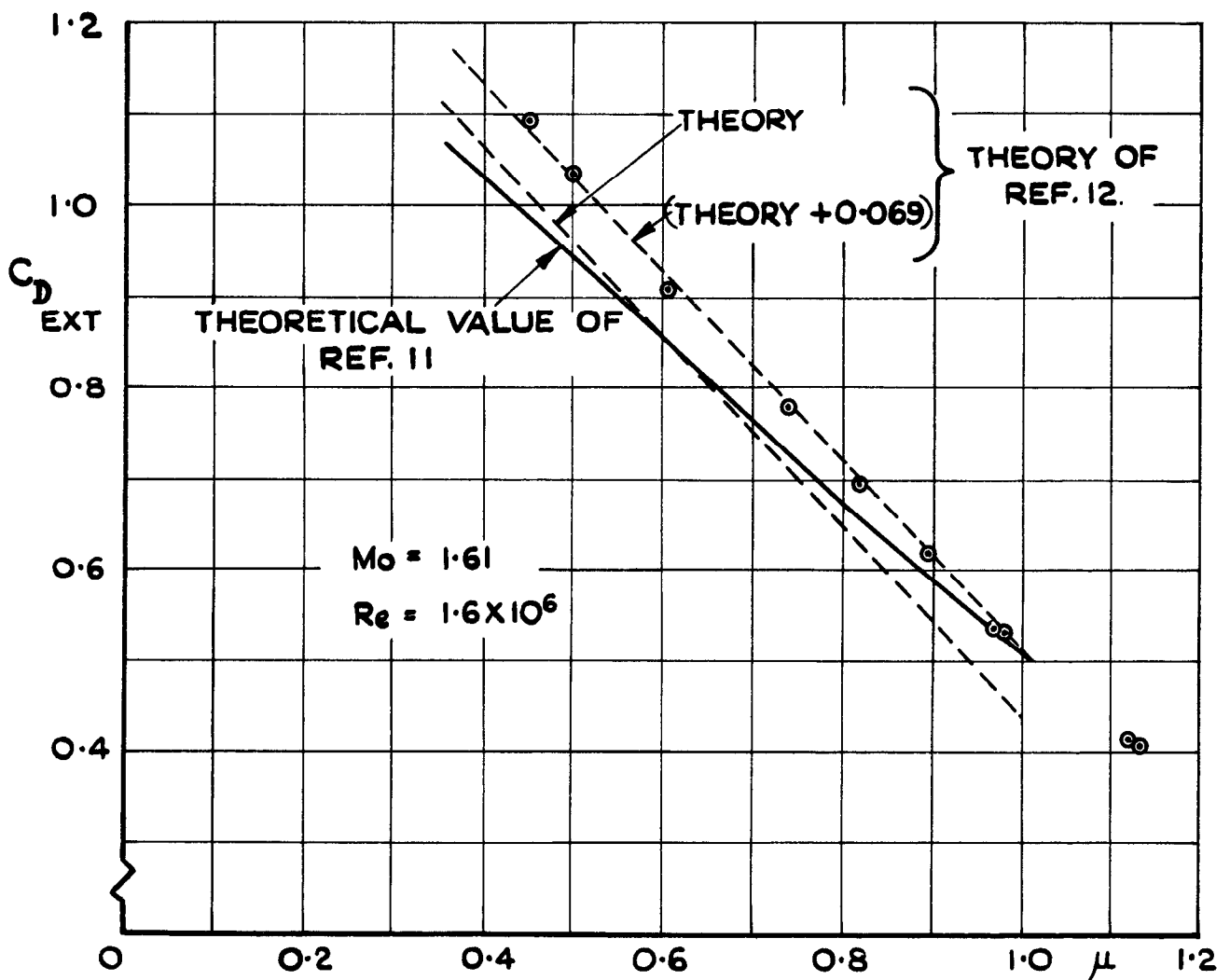
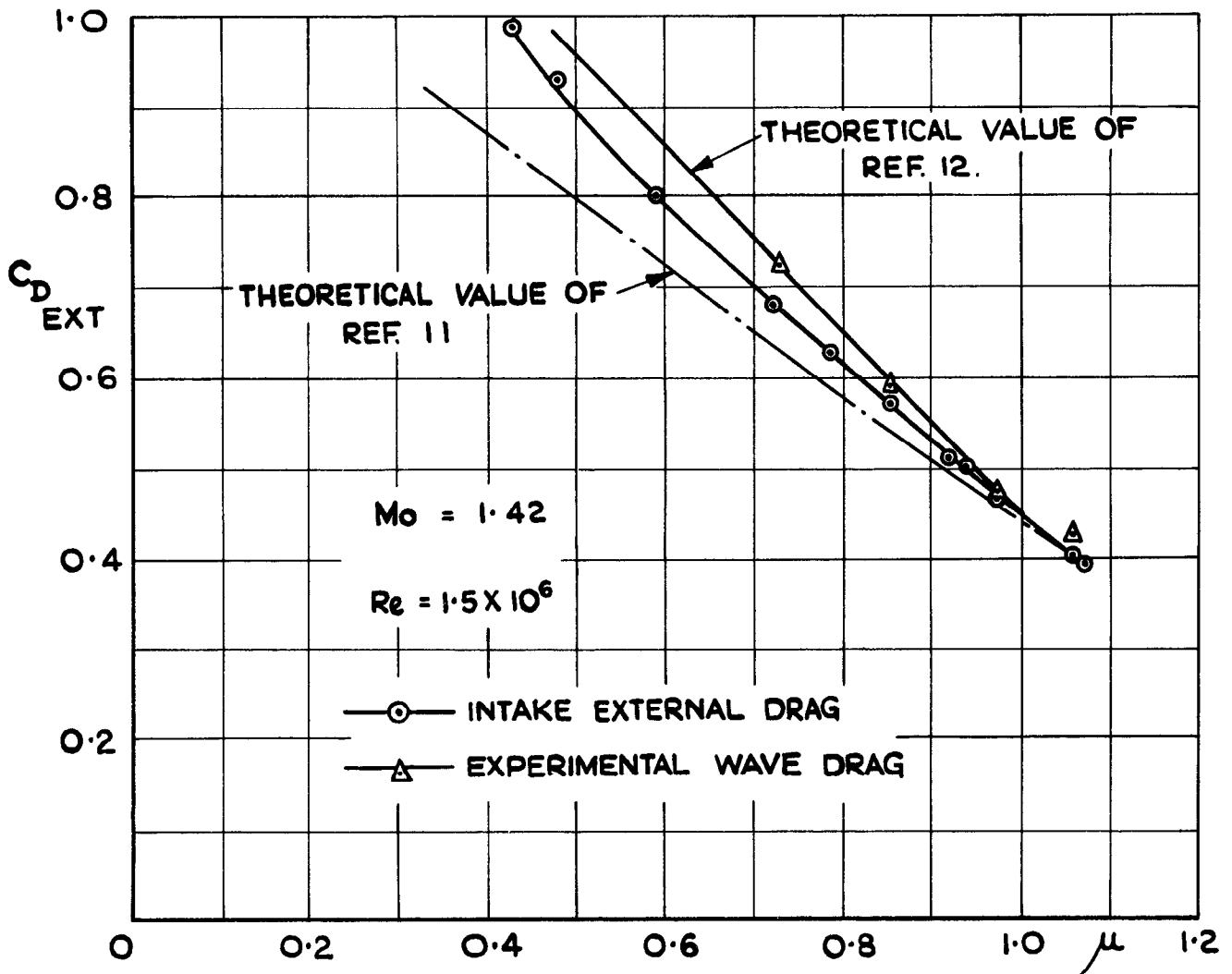


FIG.19. VARIATION OF EXTERNAL DRAG WITH MASS FLOW, BLUNT LIP COWL.

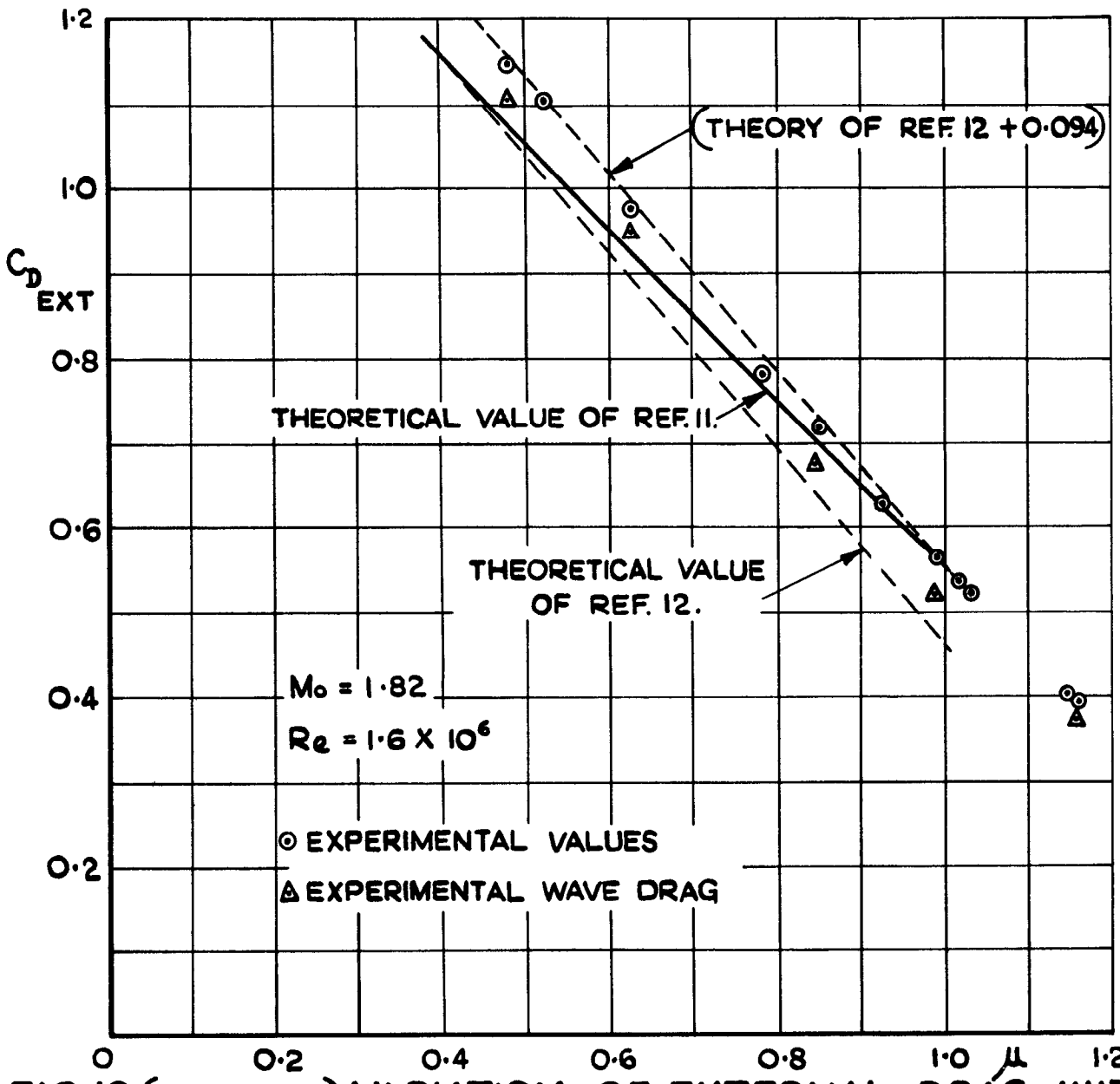


FIG. 19. (CONCLUDED) VARIATION OF EXTERNAL DRAG WITH MASS FLOW, BLUNT LIP COWL.

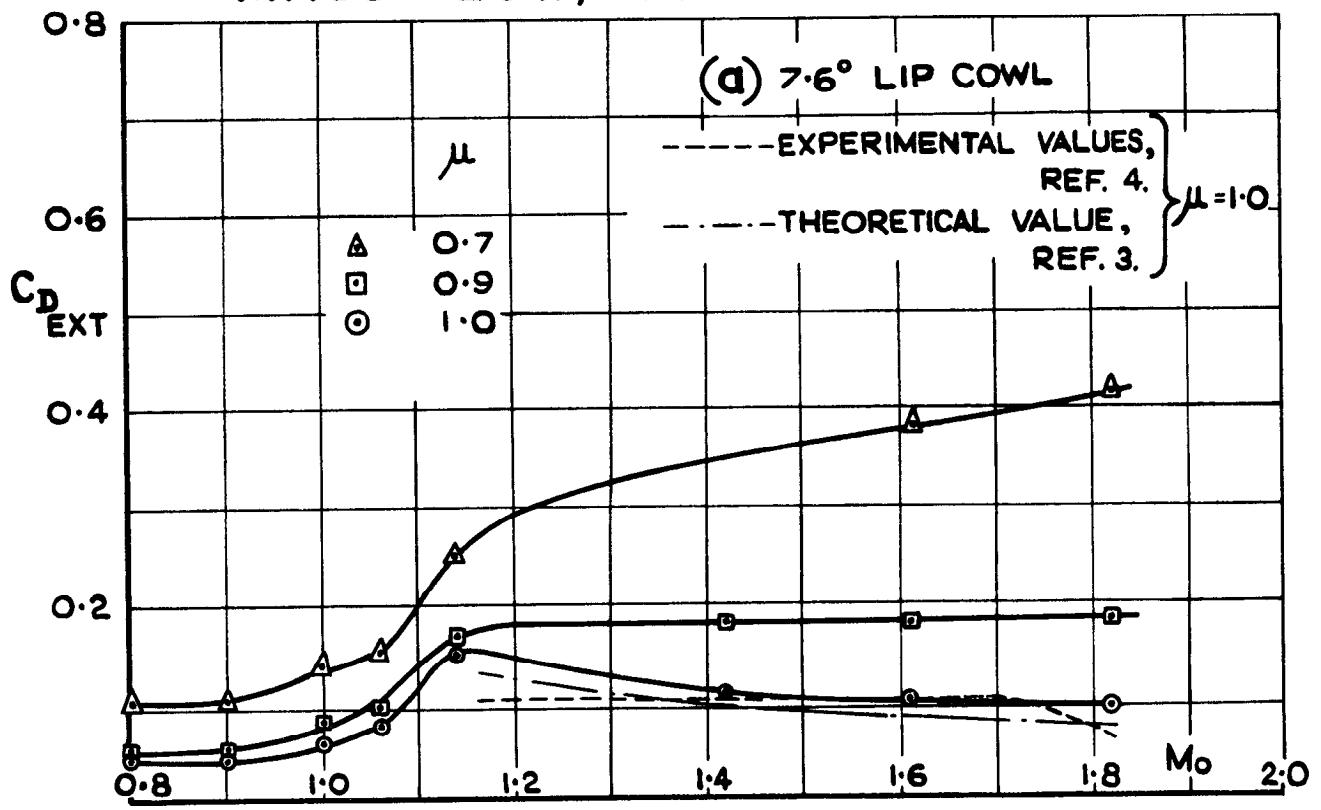
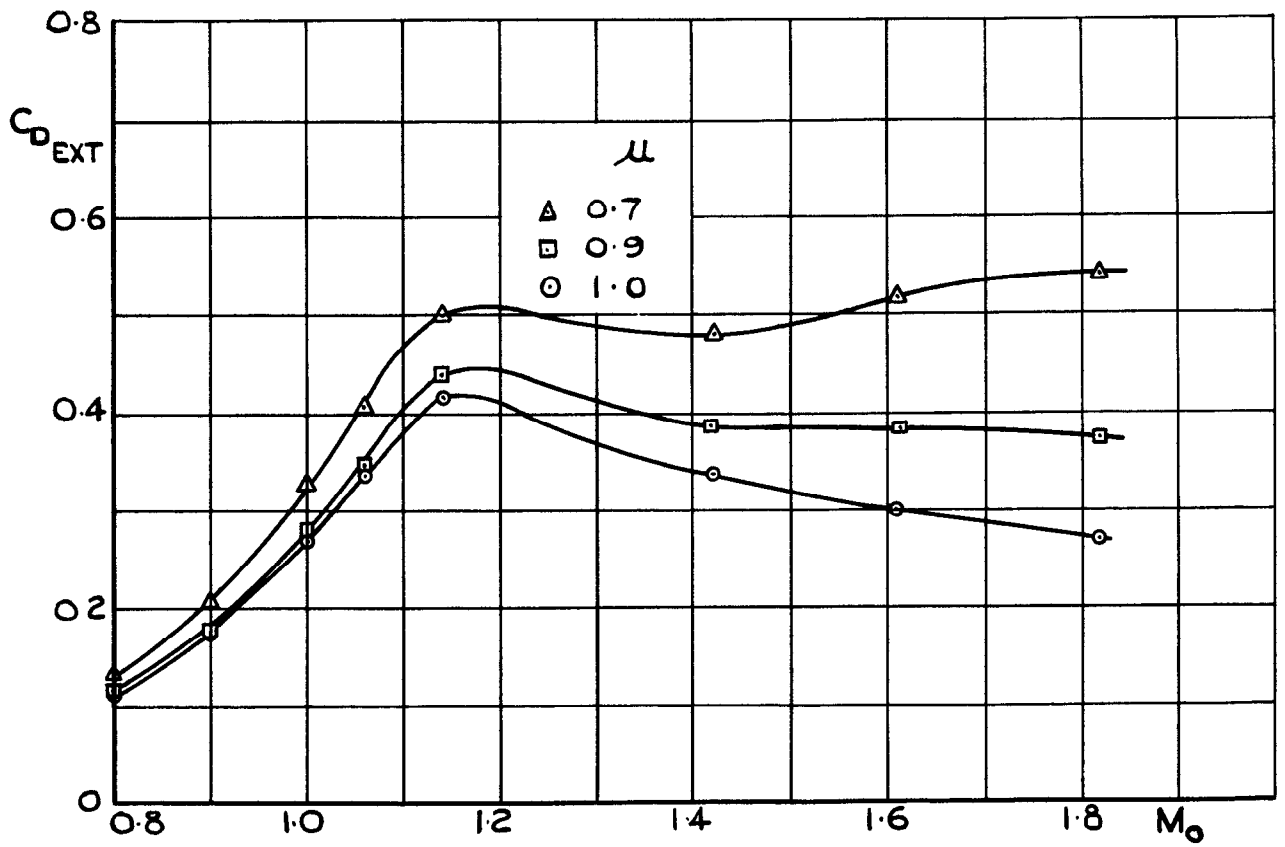
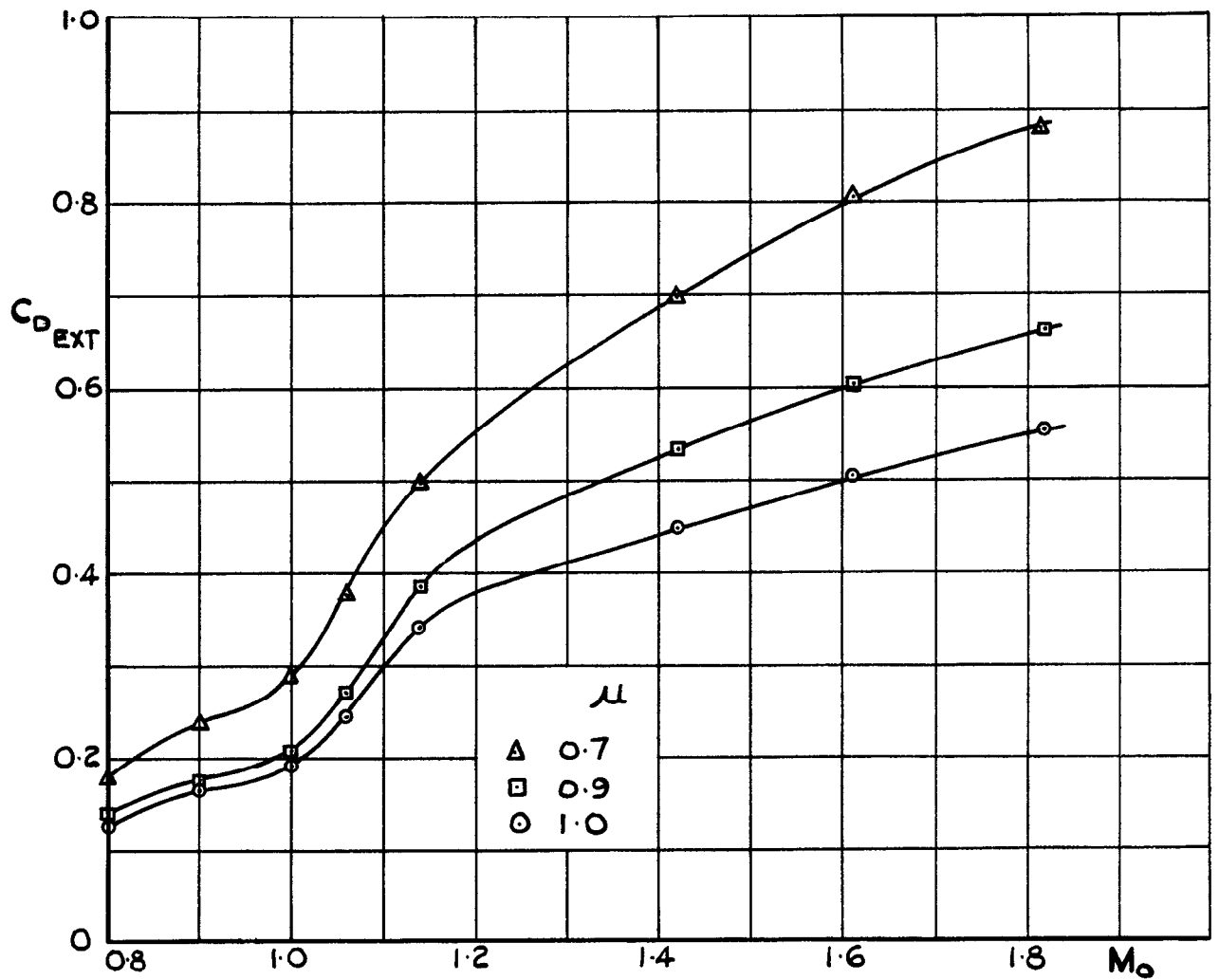


FIG. 20. - VARIATION OF $C_{D_{EXT}}$ WITH MACH NO. AT CONSTANT MASS FLOW RATIO.

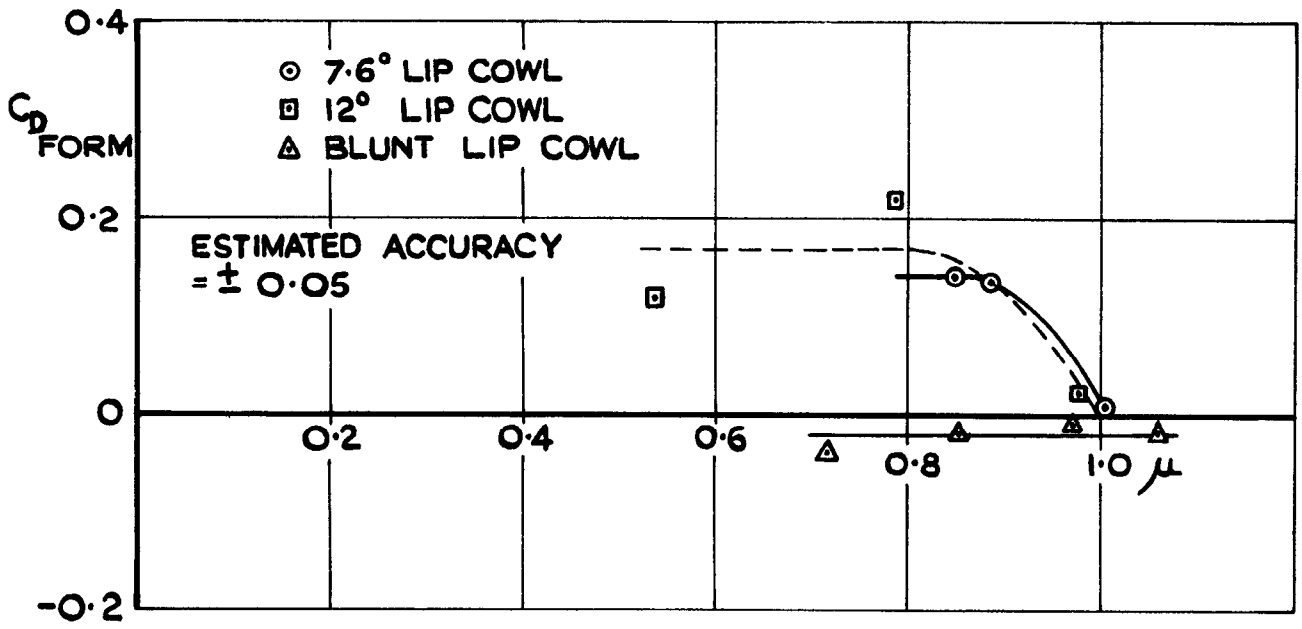


(b) 12° LIP COWL.

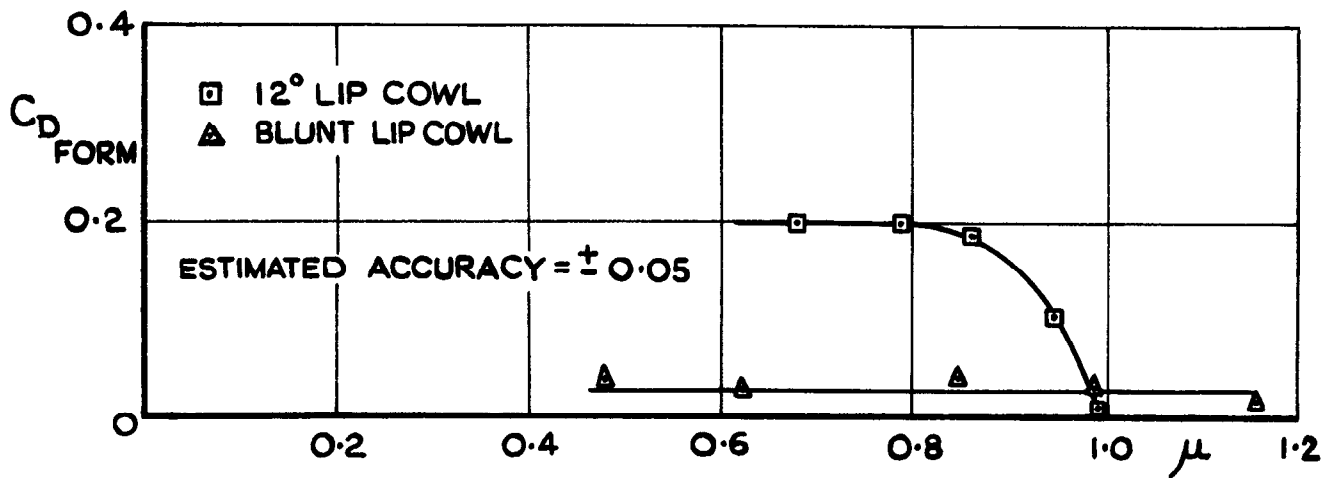


(c) BLUNT LIP COWL.

FIG. 20 (CONCLUDED) - VARIATION OF $C_{D_{EXT}}$ WITH MACH No. AT CONSTANT MASS FLOW RATIO.



(a) $M_0 = 1.42$



(b) $M_0 = 1.82$

FIG.21. VARIATION OF FORM DRAG WITH MASS FLOW RATIO.

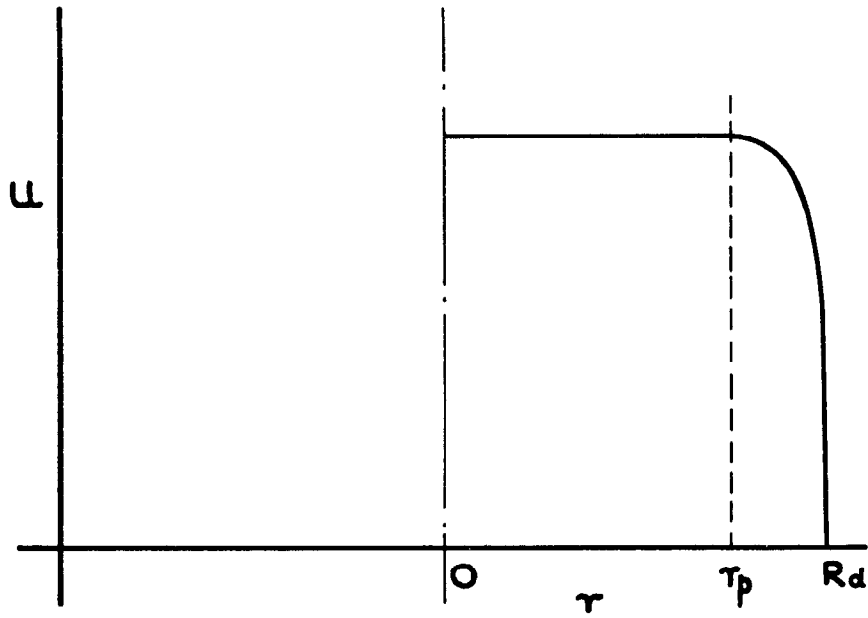


FIG. 22. ASSUMED VELOCITY PROFILE IN THE DIFFUSER.

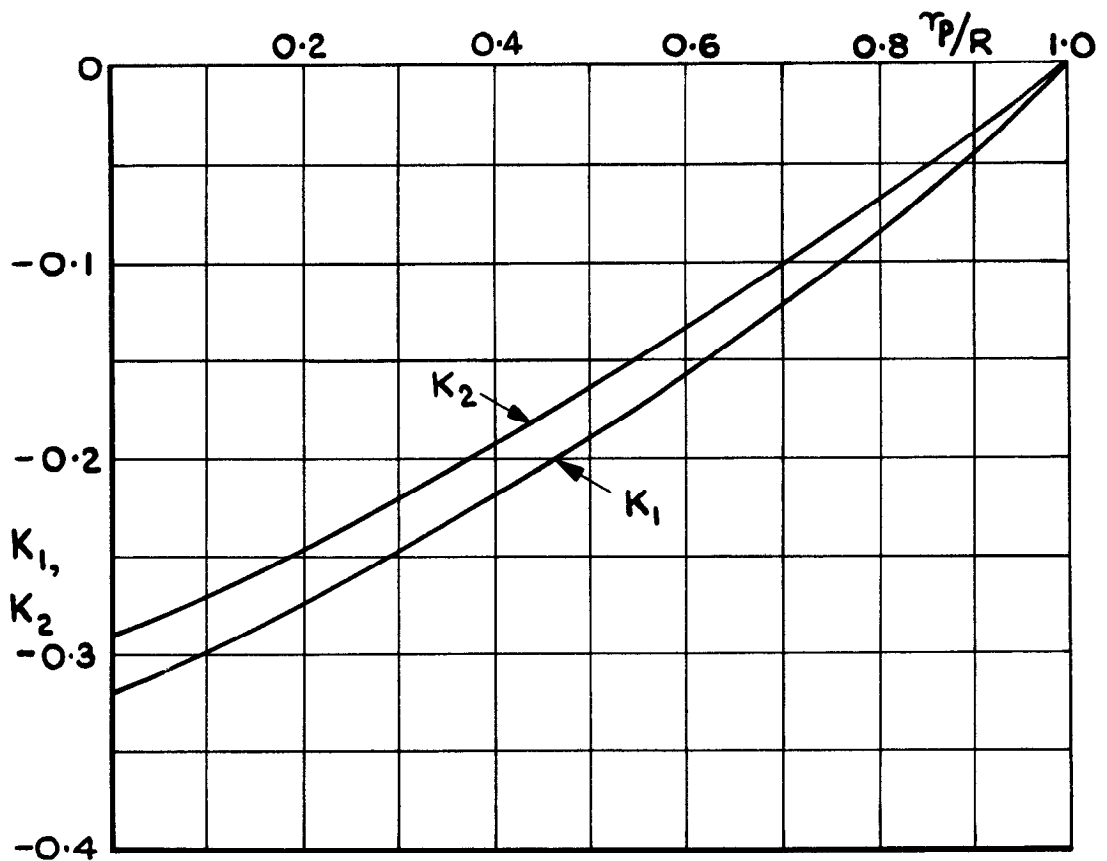


FIG. 23. PRESSURE RECOVERY FACTORS USED IN APPENDIX I.

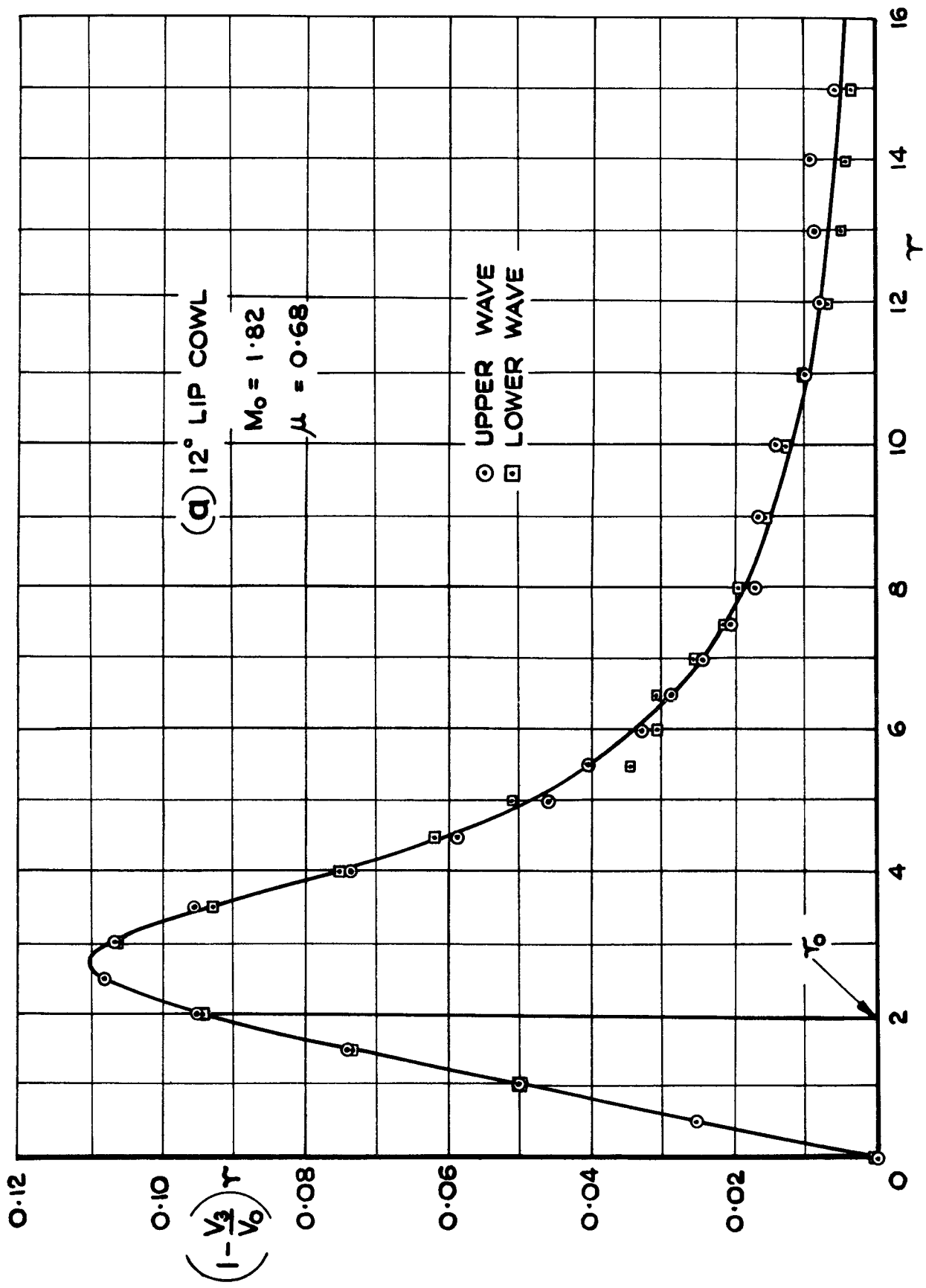


FIG. 24. - TYPICAL WAVE DRAG INTEGRATIONS (EQUATION I, APPENDIX II)

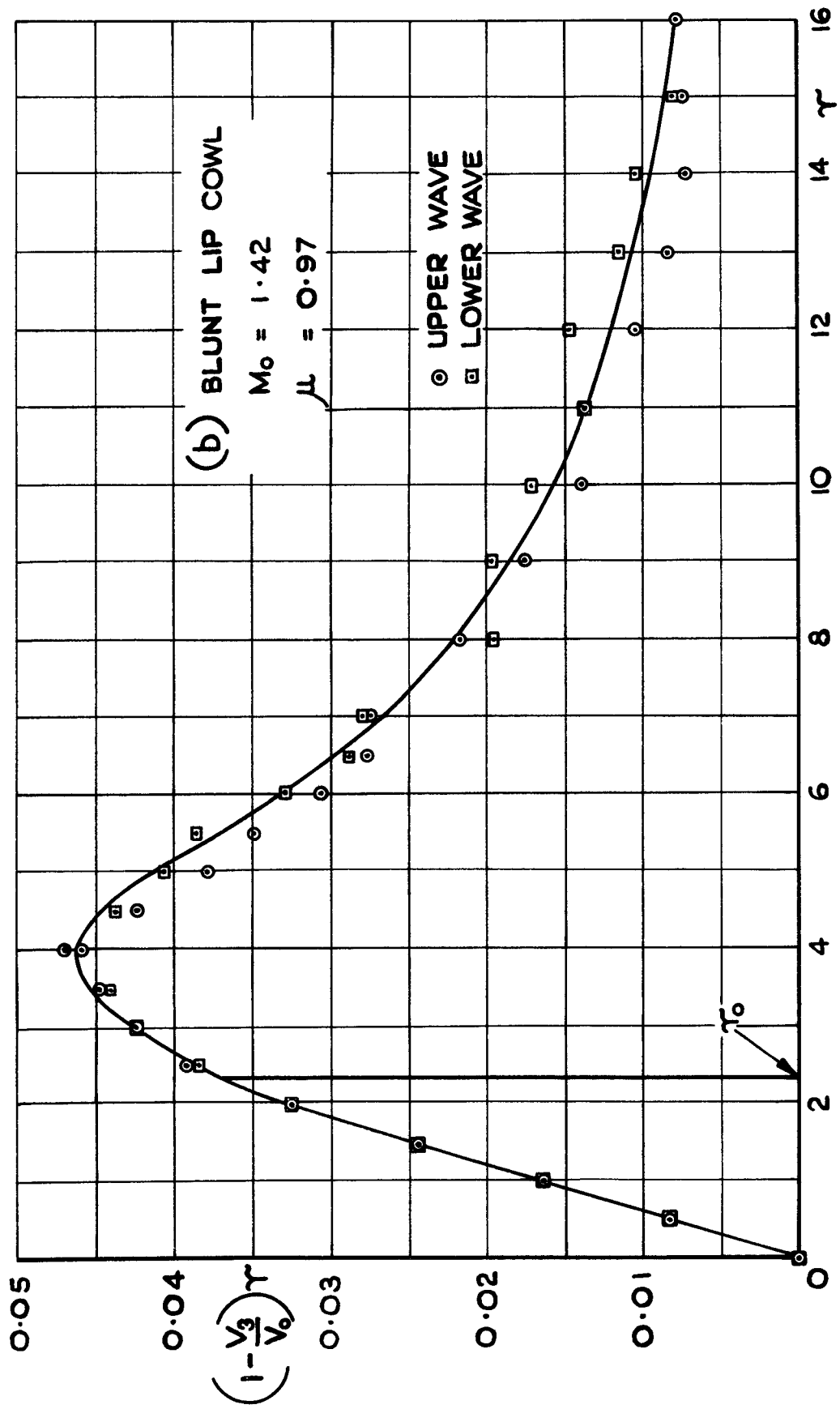


FIG. 24 (CONCLUDED) - TYPICAL WAVE DRAG INTEGRATIONS (EQUATION I, APPENDIX II)

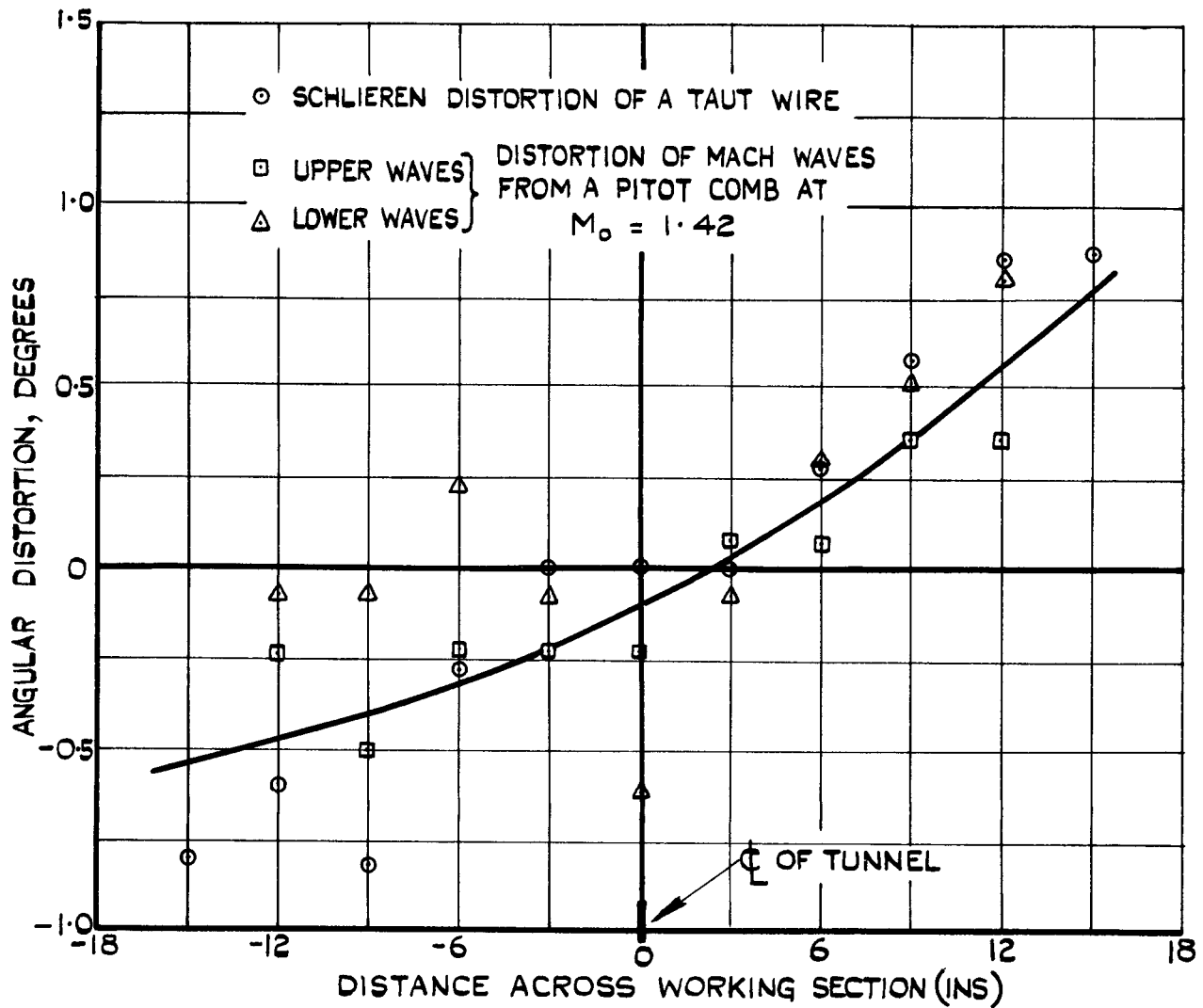


FIG. 25. ERRORS IN WAVE ANGLE DUE TO SCHLIEREN DISTORTION AND UNEVEN MACH No. DISTRIBUTION ACROSS THE TUNNEL.

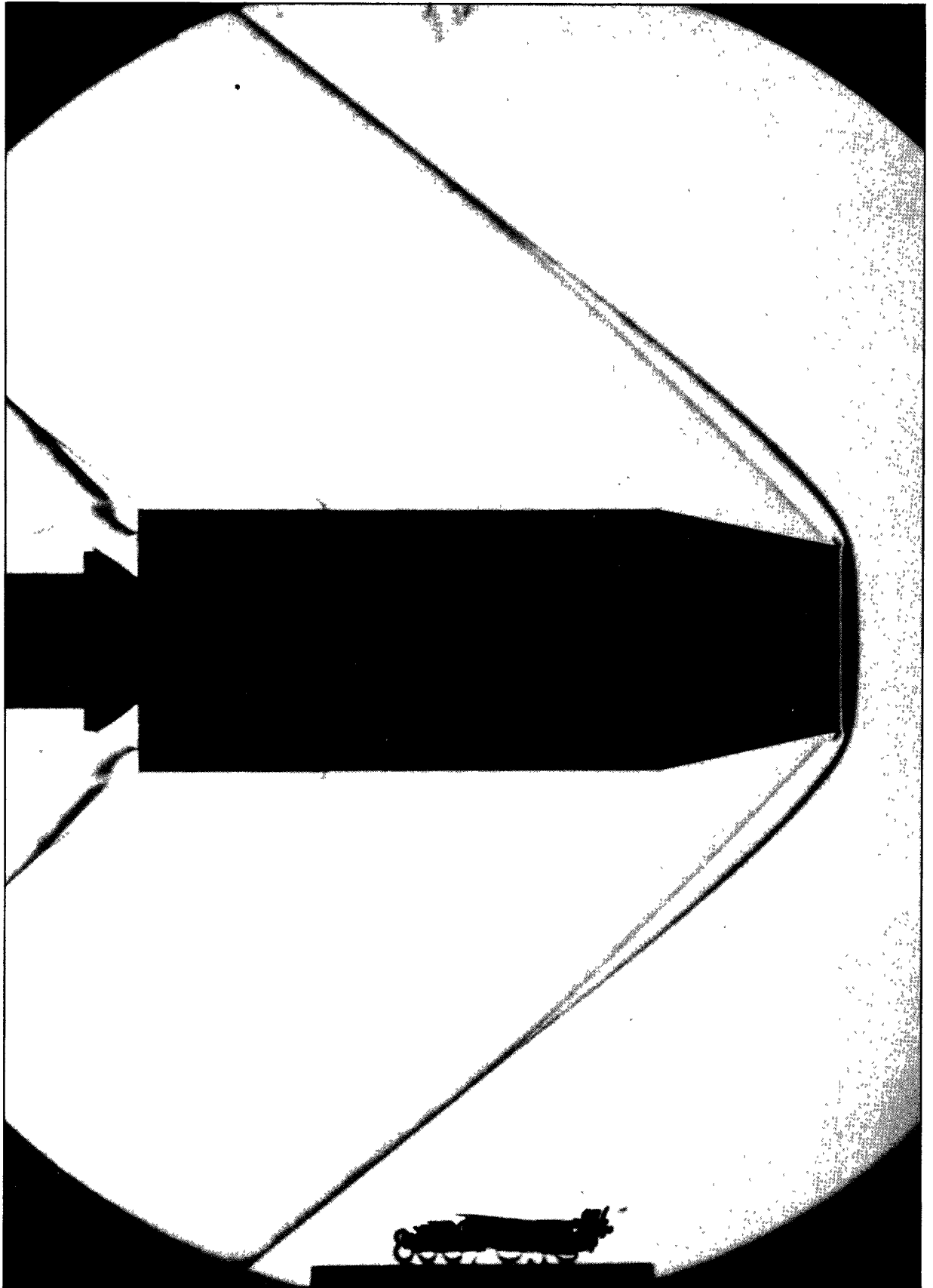


FIG.26. SCHLIEREN PHOTOGRAPH OF THE FLOW PAST
THE 12° COWL. $M_0 = 1.82$, $\mu = 0.84$

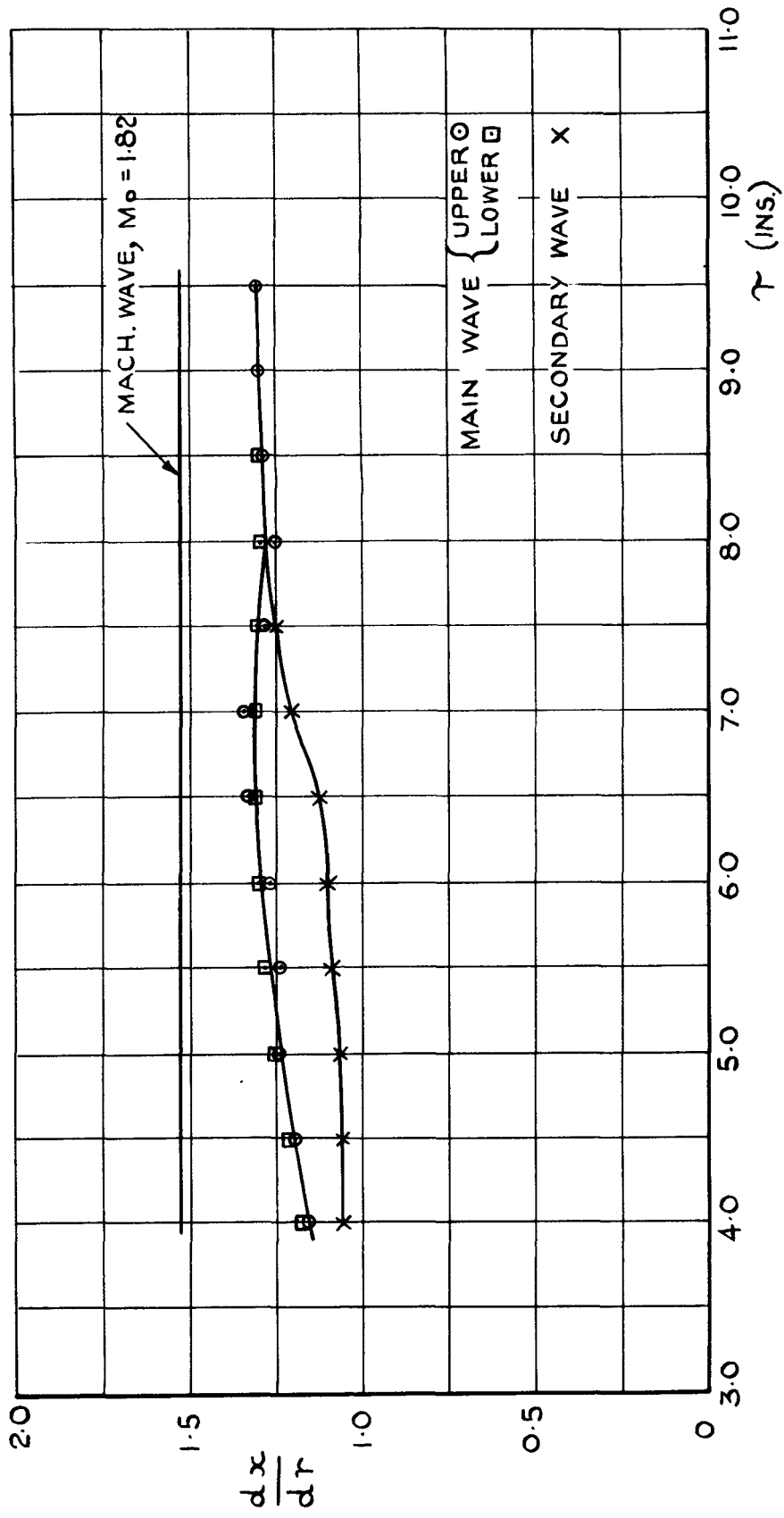
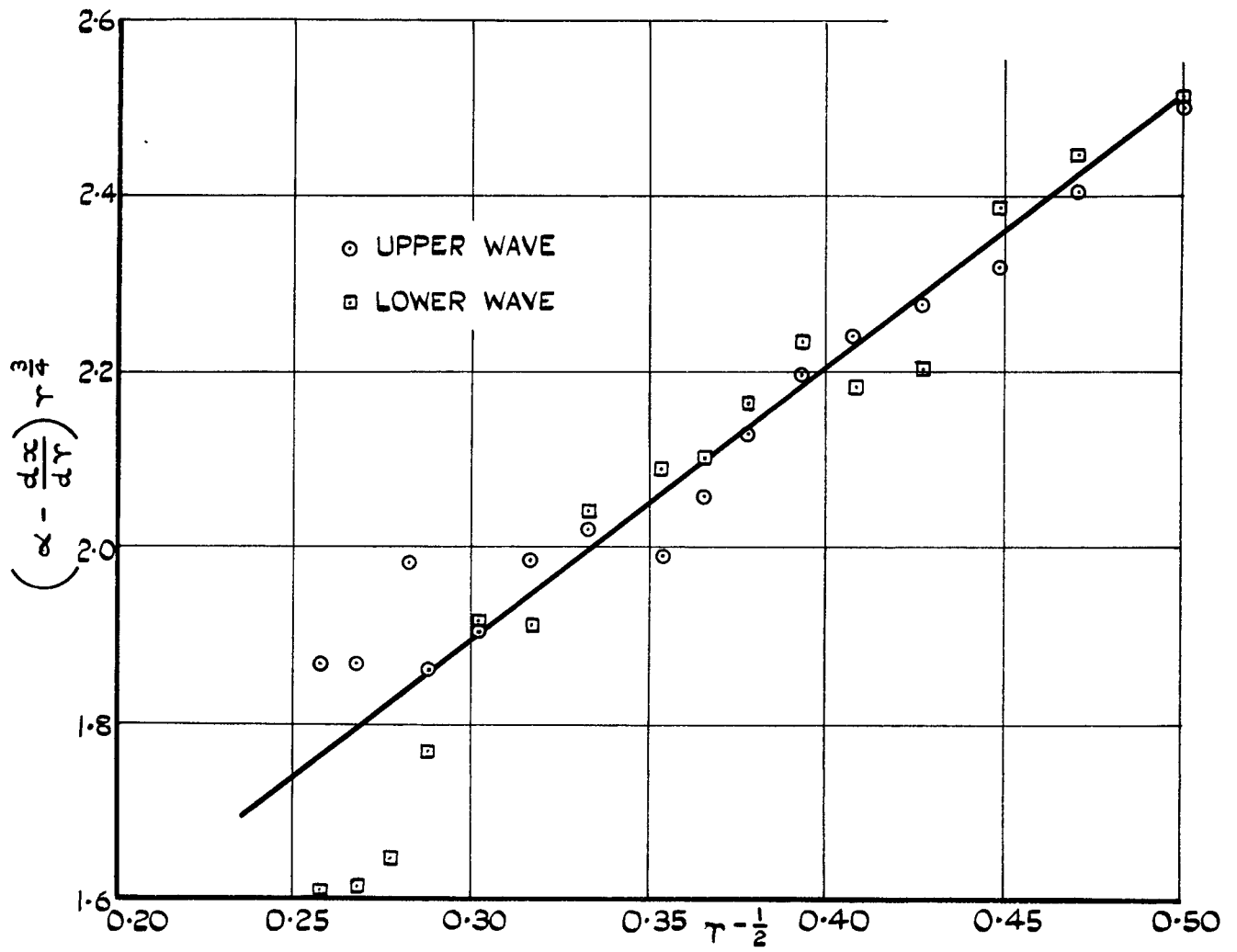
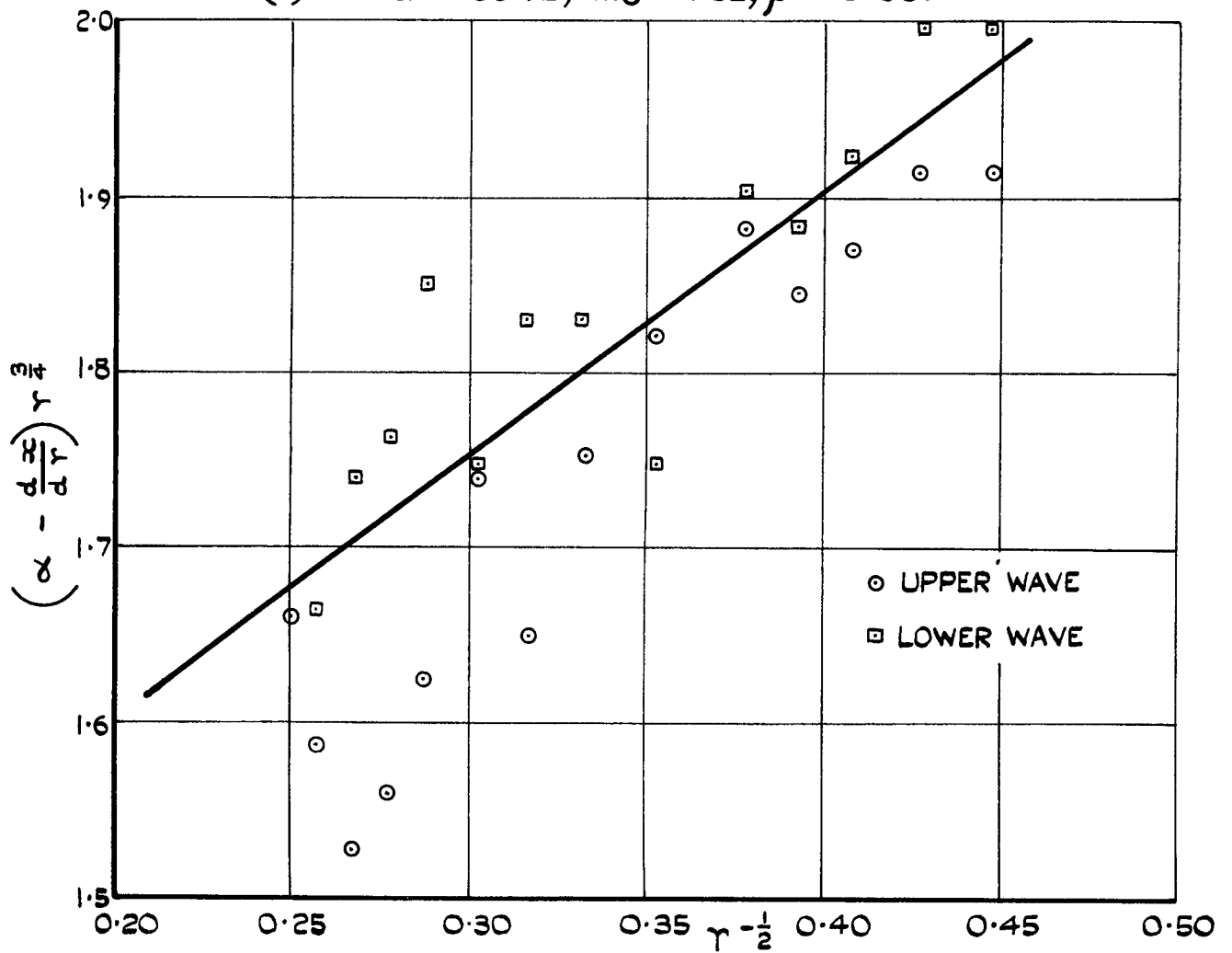


FIG. 27. INTERSECTION OF MAIN AND SECONDARY SHOCK WAVES.
 12° COWL, $M_0 = 1.82$, $\mu = 0.84$



(a) 12° LIP COWL, $M_0 = 1.82, \mu = 0.68$.



(b) BLUNT LIP COWL, $M_0 = 1.42, \mu = 0.97$.

FIG. 28. EXTRAPOLATION OF NOSE SHOCK WAVE SHAPE TO INFINITY.

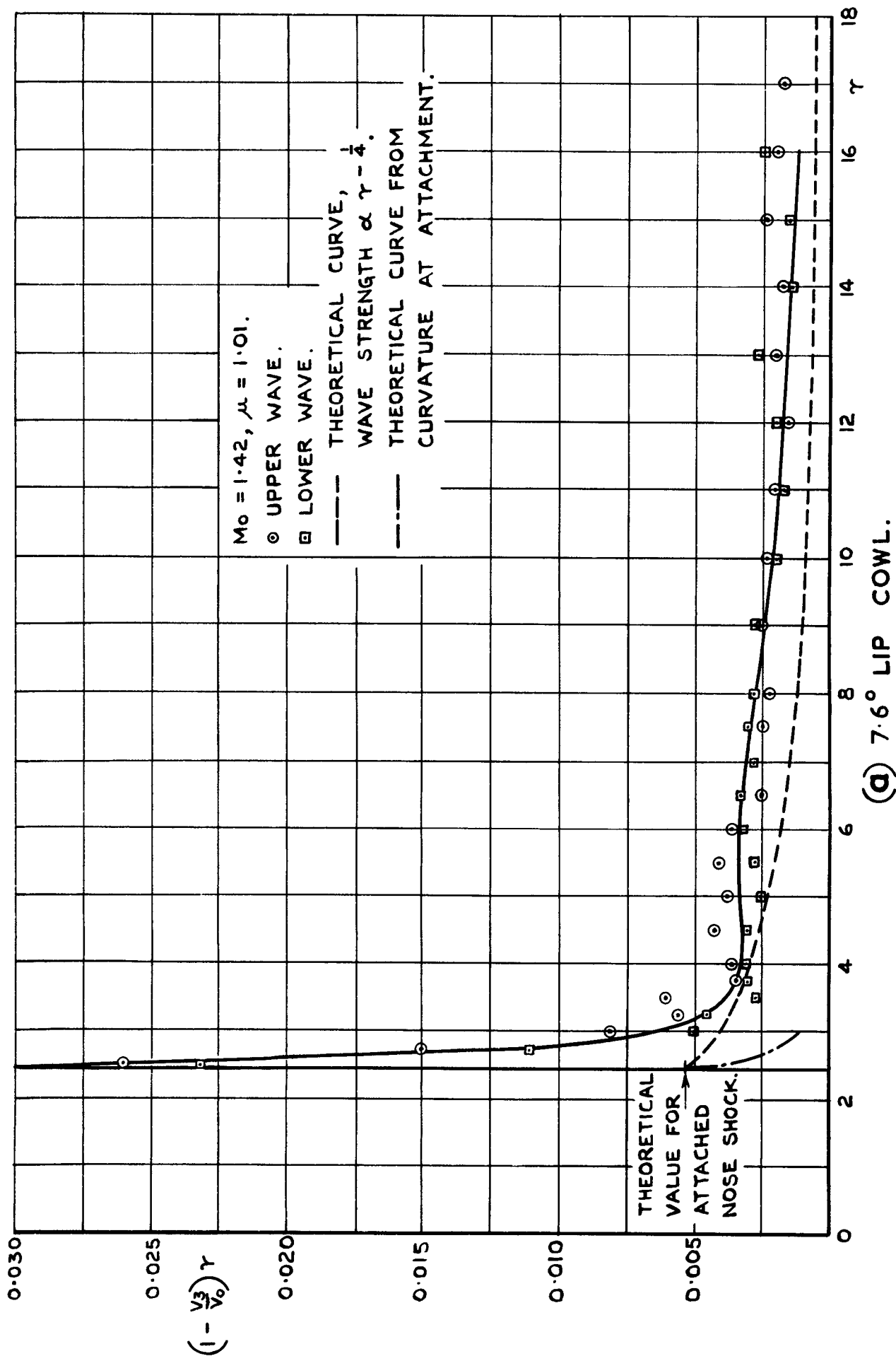
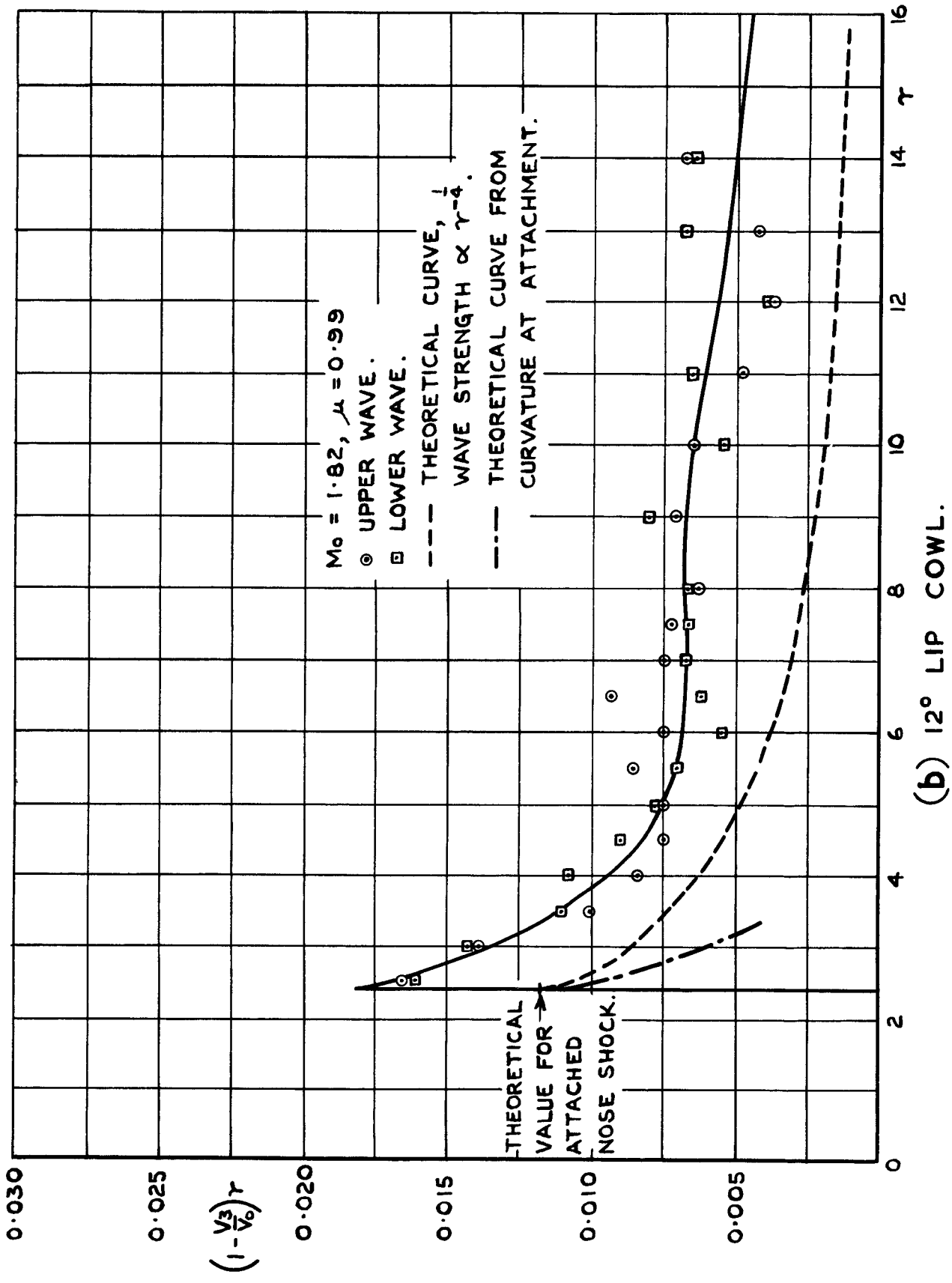


FIG. 29. WAVE DRAG INTEGRATIONS (EQUATION I, APPENDIX II)



(b) 12° LIP COWL.

FIG. 29 (CONCLUDED) - WAVE DRAG INTEGRATIONS (EQUATION I, APPENDIX II).



A.R.C. C.P. No. 544

533.697.23 :
533.6.011.5 :
533.69.048.2

PRESSURE MEASUREMENTS ON THREE OPEN NOSE AIR INTAKES AT TRANSONIC AND SUPERSONIC SPEEDS, WITH AN ANALYSIS OF THEIR DRAG CHARACTERISTICS. Gibbings, J. C. March, 1960.

Tests on three open nose air intakes at zero incidence over a Mach number range of 0.80 to 1.82 are described. Two of the cowls had sharp lips and the third a rounded lip. External pressure distributions, diffuser pressure recoveries and drags were obtained for a range of mass flow ratios. At supersonic speeds measurement of the nose shock wave shape made possible the division of the external drag into wave and separation drags. Comparisons with theoretical values are made for the pressure distributions, pressure recovery, nose shock wave shape, wave drag and external drag.

A.R.C. C.P. No. 544

533.697.23 :
533.6.011.5 :
533.69.048.2

PRESSURE MEASUREMENTS ON THREE OPEN NOSE AIR INTAKES AT TRANSONIC AND SUPERSONIC SPEEDS, WITH AN ANALYSIS OF THEIR DRAG CHARACTERISTICS. Gibbings, J. C. March, 1960.

Tests on three open nose air intakes at zero incidence over a Mach number range of 0.80 to 1.82 are described. Two of the cowls had sharp lips and the third a rounded lip. External pressure distributions, diffuser pressure recoveries and drags were obtained for a range of mass flow ratios. At supersonic speeds measurement of the nose shock wave shape made possible the division of the external drag into wave and separation drags. Comparisons with theoretical values are made for the pressure distributions, pressure recovery, nose shock wave shape, wave drag and external drag.

A.R.C. C.P. No. 544

533.697.23 :
533.6.011.5 :
533.69.048.2

PRESSURE MEASUREMENTS ON THREE OPEN NOSE AIR INTAKES AT TRANSONIC AND SUPERSONIC SPEEDS, WITH AN ANALYSIS OF THEIR DRAG CHARACTERISTICS. Gibbings, J. C. March, 1960.

Tests on three open nose air intakes at zero incidence over a Mach number range of 0.80 to 1.82 are described. Two of the cowls had sharp lips and the third a rounded lip. External pressure distributions, diffuser pressure recoveries and drags were obtained for a range of mass flow ratios. At supersonic speeds measurement of the nose shock wave shape made possible the division of the external drag into wave and separation drags. Comparisons with theoretical values are made for the pressure distributions, pressure recovery, nose shock wave shape, wave drag and external drag.

A.R.C. C.P. No. 544

533.697.23 :
533.6.011.5 :
533.69.048.2

PRESSURE MEASUREMENTS ON THREE OPEN NOSE AIR INTAKES AT TRANSONIC AND SUPERSONIC SPEEDS, WITH AN ANALYSIS OF THEIR DRAG CHARACTERISTICS. Gibbings, J. C. March, 1960.

Tests on three open nose air intakes at zero incidence over a Mach number range of 0.80 to 1.82 are described. Two of the cowls had sharp lips and the third a rounded lip. External pressure distributions, diffuser pressure recoveries and drags were obtained for a range of mass flow ratios. At supersonic speeds measurement of the nose shock wave shape made possible the division of the external drag into wave and separation drags. Comparisons with theoretical values are made for the pressure distributions, pressure recovery, nose shock wave shape, wave drag and external drag.

•

•

•

•

•

•

•

© *Crown Copyright 1961*

Published by
HER MAJESTY'S STATIONERY OFFICE

To be purchased from
York House, Kingsway, London w.c.2
423 Oxford Street, London w.1
13A Castle Street, Edinburgh 2
109 St. Mary Street, Cardiff
39 King Street, Manchester 2
50 Fairfax Street, Bristol 1
2 Edmund Street, Birmingham 3
80 Chichester Street, Belfast 1
or through any bookseller

Printed in England